HZDR-090

DOSIMETRY OF HIGHLY PULSED RADIATION FIELDS

Malte Gotz

Wissenschaftlich-Technische Berichte
HZDR-090 · ISSN 2191-8708

WISSENSCHAFTLICH-
TECHNISCHE BERICHTE

HZDR
HELMHOLTZ
ZENTRUM DRESDEN
ROSSENDORF

Wissenschaftlich-Technische Berichte
HZDR-090

Malte Gotz

DOSIMETRY OF HIGHLY PULSED RADIATION FIELDS

HZDR

HELMHOLTZ
ZENTRUM DRESDEN
ROSSENDORF

Druckausgabe: ISSN 2191-8708

Elektronische Ausgabe: ISSN 2191-8716

https://www.hzdr.de/publications/Publ-27317

urn:nbn:de:bsz:d120-qucosa-235168

Die vorliegende Arbeit wurde sowohl als Dissertation an der Medizinischen Fakultät Carl Gustav Carus der Technischen Universität Dresden sowie als Wissenschaftlich-Technischer Bericht des Helmholtz-Zentrum Dresden – Rossendorf mit der Berichtsnummer **HZDR-090** veröffentlicht.

2018

Herausgegeben vom

Helmholtz-Zentrum Dresden - Rossendorf

Bautzner Landstraße 400

01328 Dresden

Germany

Aus dem Nationalen Zentrum für Strahlenforschung in der Onkologie – OncoRay
Direktor: Frau Prof. Dr. Mechthild Krause

Dosimetry of Highly Pulsed Radiation Fields

Dissertationsschrift

zur Erlangung des akademischen Grades
Doktor der Medizintechnologie
Doctor rerum medicinalium (Dr. rer. medic.)
vorgelegt
der Medizinischen Fakultät Carl Gustav Carus
der Technischen Universität Dresden
von

Malte Gotz
aus Berlin

Dresden 2018

1. Gutachter: Prof. Dr. Wolfgang Enghardt

2. Gutachter: Prof. Dr. Klemens Zink

Tag der mündlichen Prüfung: 21. März 2018

gez.: Prof. Dr. Ralf-Thorsten Hoffmann
Vorsitzender der Promotionskommission

Contents

List of Figures v

List of Tables vii

List of Abbreviations ix

1 Introduction 1

2 Scientific Background 5
- 2.1 General Aspects of Dosimetry 5
  - 2.1.1 The Radiation Dose 5
  - 2.1.2 Limitations of Absorbed Dose 6
  - 2.1.3 Radiation Therapy vs. Radiation Protection 6
- 2.2 Pulsed Radiation 8
  - 2.2.1 Terminology 8
  - 2.2.2 Sources 10
- 2.3 Ionization Chambers for Radiation Therapy Dosimetry 13
  - 2.3.1 Principle of Operation 14
  - 2.3.2 Calibration and Correction Factors 16
  - 2.3.3 Saturation Correction and Volume Recombination 18
- 2.4 Numerical Solution of Advection-Diffusion-Reaction Equations 25
- 2.5 Dose Rate Meters for Radiation Protection Dosimetry 29
  - 2.5.1 Counting Tubes 30
  - 2.5.2 Scintillation Detectors 32
  - 2.5.3 Current Regulatory Developments 33

3 Material and Methods 35
- 3.1 Common Experimental Setup 35
  - 3.1.1 Radiation Source ELBE 37
  - 3.1.2 Beam Monitoring Equipment 38
- 3.2 Dose Rate Meter Measurements 39
  - 3.2.1 Measurement Series and Procedure 39
  - 3.2.2 Reference Measurements 40
- 3.3 Ionization Chamber Measurements 41
  - 3.3.1 Measurement Series and Procedure 43
  - 3.3.2 Experimental Determination of Volume Recombination 44

3.4 Numerical Calculation of Volume Recombination 46
    3.4.1 Plane-parallel Chamber Geometry 46
    3.4.2 Adaption to Thimble Chamber Geometry 49
    3.4.3 Input Parameters 50

4 Dose Rate Meter Investigation **55**
4.1 Results 55
4.2 Discussion and Conclusion 59

5 Ionization Chamber Investigation **65**
5.1 Field Homogeneity and Stability 65
5.2 Uncertainty Considerations 65
5.3 Advanced Markus Chamber in Air 69
    5.3.1 Experimental and Calculation Results 69
    5.3.2 Comparison to Literature 72
    5.3.3 Validity of the Numerical Model 74
    5.3.4 Discussion of the Recombination Rate 76
    5.3.5 Relevance of the Free Electron Fraction 78
5.4 Advanced Markus Chamber in N_2 81
    5.4.1 Experimental and Calculation Results 81
    5.4.2 Discussion of the Electron-Ion Recombination 83
5.5 PinPoint Chamber 85
    5.5.1 Results and Discussion 85
5.6 Liquid Ionization Chamber 88
    5.6.1 Experimental and Calculation Results 88
    5.6.2 Discussion 91
5.7 Conclusion and Outlook 92

6 Summary **95**

7 Zusammenfassung **99**

Bibliography **103**

Appendix **113**
A Evaluation of the Faraday Cup Data 113
B Description of the Implemented Numerical Solver 116

Danksagung **119**

List of Figures

1.1 The dose-effect relationship in radiation therapy 1

2.1 Pulse parameter definitions 9
2.2 Macro and micro-pulse time structure 10
2.3 General ionization chamber structure 14
2.4 1-D spatial discretization with a uniform grid 25
2.5 Comparison of 1-D calculations using different spatial discretizations 28
2.6 Regions of operation of gas-filled ionization detectors 30

3.1 Experimental setup 36
3.2 Size and orientation of the ICs in the experiment 42
3.3 Spatial discretization of a plane-parallel chamber 47
3.4 Electron velocity in air 51
3.5 Electron attachment rate in air 51

4.1 Field homogeneity measurements for dose rate meters 56
4.2 LB 1236-H10 results 57
4.3 RamION results 58
4.4 6150AD-b results 58

5.1 EBT-Films showing lateral field homogeneity for the IC measurements . . . 66
5.2 Beamspot position analysis 67
5.3 Adv. Markus chamber in air: dose-per-pulse dependence 70
5.4 Adv. Markus chamber in air: $U_\mathrm{c} = 100\,\mathrm{V}$ and low dose-per-pulse 71
5.5 Adv. Markus chamber in air: pulse duration dependence 73
5.6 Adv. Markus chamber in air: comparison to literature 74
5.7 Adv. Markus chamber in air: variations of the numerical calculation 75
5.8 Numerical calculation for additional plane-parallel chambers 80
5.9 Adv. Markus chamber: dose-per-pulse dependence in N_2 and air 82
5.10 Adv. Markus chamber: pulse duration dependence in in N_2 and air 82
5.11 E-Field strength in the Adv. Markus chamber 84
5.12 PinPoint chamber: dose-per-pulse dependence 86
5.13 PinPoint chamber: pulse duration dependence 86
5.14 LICs: dose-per-pulse dependence 89
5.15 LICs: pulse duration dependence 90
5.16 Isooctane LIC: extended pulse duration dependence 90

A.1 Evaluation of a short pulse 114
A.2 Evaluation of an intermediate length pulse 114
A.3 Evaluation of a long pulse 115
B.1 Flow-chart of the numerical solver 117

List of Tables

2.1 Pulse parameters of 5 pulsed radiation sources 12

3.1 Properties of the investigated dose rate meters 39
3.2 Properties of the investigated ionization chambers 41
3.3 Recombination rates, mobilites and permittivity in the LICs 54

5.1 Adv. Markus chamber: fit results of $(k_{\mathrm{s}})'_{\mathrm{th}}$ 69
5.2 $(k_{\mathrm{s}})_{\mathrm{num}}$ for different grid sizes 76
5.3 Adv. Markus chamber: fit results of $(k_{\mathrm{s}})_{\mathrm{num}}$ 77
5.4 Free electron fraction at different Q_0 79
5.5 Effect of electron-ion recombination on $(k_{\mathrm{s}})_{\mathrm{num}}$ 83
5.6 Electron collection time in air and N_2 83
5.7 PinPoint chamber: fit results of $(k_{\mathrm{s}})'_{\mathrm{th}}$ and $(k_{\mathrm{s}})_{\mathrm{num}}$ 87
5.8 LICs: fit results of $(k_{\mathrm{s}})_{\mathrm{th}}$ 89

List of Abbreviations

EBRT external beam radiation therapy

ELBE Electron LINAC for beams with high Brilliance and low Emittance

FWHM full width at half maximum

IC ionization chamber

ICT integrated current transformer

IMRT intensity modulated radiation therapy

IORT intraoperative radiation therapy

IP image plate

LET linear energy transfer

LIC liquid ionization chamber

LINAC linear accelerator

ODE ordinary differential equation

OSL optically stimulated luminescence

PDE partial differential equation

PMMA poly(methyl methacrylate)

PMT photomultiplier tube

PTB Physikalisch-Technische Bundesanstalt

RBE relative biological effectiveness

TLD thermoluminescent dosimeter

TMS tetramethylsilane

TVA two voltage approximation

YAG yttrium aluminium garnet

1 Introduction

About half of the roughly 500,000 annual new cancer patients in Germany receive radiation therapy at some point during their treatment. This already impressive number of annual patients is expected to grow by at least 20 % by 2030 due to the continued aging of our society (RKI, 2015). Considering the number of people impacted by radiation therapy, it is safe to say that it is a key component in our health care system and it will continue to be a key tool in surmounting the challenges of an aging society.

As with any therapy, the key to a successful radiation treatment is to find the right dosage. In particular, radiation therapy inevitably results in the irradiation of both the tumor and healthy tissue. Consequently, increasing the applied amount of ionizing radiation, that is the dose, causes greater damage to the tumor thus increasing the probability to control it, but also causes more damage to healthy tissue thus increasing the probability of complications. This relation is illustrated in Fig. 1.1. Depending on the separation and difference in slope of these two effects, there may only be a narrow dose range where the probability of treatment success (i.e., complication free tumor control) is deemed acceptable and it is this therapeutic window that must be targeted. Therefore, dosimetry, the measurement of radiation dose, is a vital cornerstone of radiation therapy.

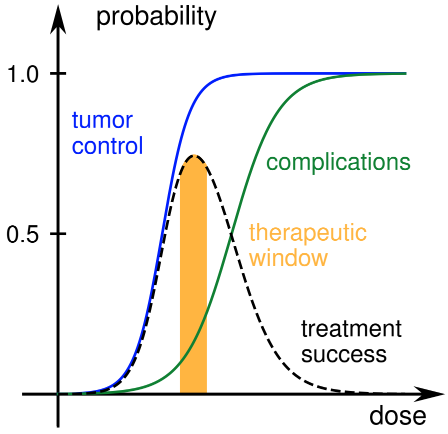

Figure 1.1: The dose dependence of radiation effects according to Holthusen (1936)

In addition to this clinical dosimetry, which determines the intentionally applied dose to a patient, there is a need for radiation protection dosimetry because, in contrast to other therapeutics, radiation is not easily confined to the patient at hand. This includes the monitoring of the environment to ensure the adequacy of radiation shielding and to assess and minimize the risks posed by any inadvertent irradiation.

Two general techniques to deliver radiation to a tumor exist: inserting a radioactive source in brachytherapy or applying a beam of ionizing radiation from outside the patient in external beam radiation therapy (EBRT). The virtual standard radiation source for EBRT in the developed world since the beginning of the 21st century is the compact electron linear accelerator (LINAC) (Grau et al., 2014), providing electrons of energy up to 20 MeV and, by virtue of Bremsstrahlung, also corresponding photon fields. In addition, the still emerging field of particle therapy mainly utilizes cyclotrons and synchrotrons to produce beams of highly energetic protons or heavier ions (PTCOG, 2016). Common to all these state-of-the-art sources for EBRT is that they produce pulsed radiation fields with a dose-per-pulse of a few milligray and a pulse duration in the micro- to millisecond range. In contrast, the fields produced by the radioactive sources used in brachytherapy are not pulsed and, while some pulsed applications exist, they are not considered here.

Currently, several developments push EBRT towards even more strongly pulsed fields. On the one hand the technological quest for compact particle therapy facilities will most likely result in highly pulsed fields. While particle therapy provides clear dosimetric advantages (Baumann et al., 2016), size and cost constraints have limited its adoption to currently world wide 65 operational facilities (PTCOG, 2016). Recently commercialized synchrocyclotrons (Mevion, 2012; IBA, 2014) and laser particle accelerators in the research phase (Masood et al., 2014) are two examples of highly pulsed sources aiming to overcome this limitation. The radiation field of, for example, a laser particle accelerator could have a dose-per-pulse of around 1 Gy at a pulse duration of a few picoseconds, dwarfing the values of the state-of-the-art sources.

On the other hand, a highly pulsed radiation field might provide a clinical benefit in its own right. There are efforts to reduce the uncertainty introduced by motion and anatomical changes through the usage of highly pulsed electron sources with their ability to apply treatment doses in fractions of a second (Maxim and Loo, 2014; Maier et al., 2017). Furthermore, recent animal studies have suggested that highly pulsed irradiation could lower complications, while maintaining the level of tumor control of continuous irradiation (Favaudon et al., 2014; Loo et al., 2017).

Regardless of the reason to employ a highly pulsed radiation field, for a proper medical application, it must be accompanied by an appropriate dosimetry. Clinical dosimetry of the pulsed radiation fields produced by state-of-the-art accelerators is well established, predominantly using ionization chambers. Their key property relevant for pulsed fields, the volume recombination, was described in the seminal work of Boag (1950), and well established standards (DIN, 2008) and codes of practice (Almond et al., 1999; Andreo et al., 2000) exist for their usage. However, these procedures and descriptions may reach their limit in the face of a 1000-fold increase in dose-per-pulse (from mGy to Gy).

In addition, radiation protection instruments are typically not certified for use in pulsed fields at all (PTB, 2009) and doubt as been cast on their general suitability for pulsed fields, particularly in the case of active personnel dosimeters (IAEA, 2007; Clairand et al., 2008; Ankerhold et al., 2009).

This thesis aims to investigate these challenges faced by dosimetry of highly pulsed fields, both in the context of clinical dosimetry for radiation therapy as well as in the context of ambient radiation protection dosimetry. To this end the state-of-the-art instrument for clinical dosimetry, the ionization chamber, is investigated experimentally for its response in highly pulsed fields, accompanied by the development of a theoretical description of the volume recombination based on a numerical solution of the processes in the ionization chamber. This should allow to explore the limits of the current theory and possibly provide a better description. Radiation protection dosimetry is analyzed in the form of three dose rate meters based on different common operating principles, whose response in highly pulsed fields is investigated experimentally and compared to the expectations based on current knowledge.

As a foundation, the basics and the state-of-the-art regarding clinical and radiation protection dosimetry of pulsed fields are presented in the following, second chapter. This is accompanied by an introduction to pulsed radiation sources and to the numerical solution of partial differential equations, the latter of which forms the basis for the developed description of volume recombination in ionization chambers. The subsequent materials and methods (chapter 3) describe the experimental setup and procedure to investigate instruments for both applications. In addition, the developed calculation of volume recombination in pulsed fields is described therein. Following those descriptions the results are presented and discussed in separate chapters for the dose rate meters (chapter 4) and the ionization chambers (chapter 5). Finally, a summary of the thesis is found after these two chapters.

2 Scientific Background

2.1 General Aspects of Dosimetry

2.1.1 The Radiation Dose

Radiation, as applied in radiation therapy or of concern in radiation protection, is more aptly termed ionizing radiation, that is radiation with the ability to – directly or indirectly – ionize matter. Specifically, ionization refers to the liberation of electrons from atoms or molecules, creating a positive ion and one or more unbound electrons (ICRU, 2011).

This property is central to the induction of a biological effect by radiation, which is the eventual consequence of concern in both radiation therapy and radiation protection. A biological effect is the result of a multistage cascade, where the physical interaction of radiation with matter ionizes it, inducing chemical alterations, which in turn can lead to, early or late, biological effects in the form of, for example, cell death or carcinogenic genetic mutations (Krieger, 1998).

While the physical interactions of radiation are very diverse, depending on radiation type, energy and also the target matter – detailed in common textbooks, such as Krieger (1998) or Knoll (2000)) – the end result of the physical interaction stage are invariably ionizations due to the local deposition of energy. Hence, a dose for the purpose of establishing dose-to-biological-effect relationships, such as those shown in Fig. 1.1, should quantify this energy deposition. This role is fulfilled by the *absorbed dose*

$$D = \frac{\mathrm{d}E}{\mathrm{d}m},$$

defined as the energy imparted by ionizing radiation $\mathrm{d}E$ to matter of mass $\mathrm{d}m$, measured in the unit gray with 1 Gy $=$ 1 J/kg (ICRU, 2011). The absorbed dose serves to abstract the various physical interaction mechanisms of ionizing radiation, quantifying the eventual result of locally imparted energy to matter, which causes the ionization.

2.1.2 Limitations of Absorbed Dose

Despite the common nature of ionizing radiation, the same dose, applied with different radiation qualities may not lead to the same biological effect. In this context radiation quality usually refers to the energy spectrum and type of radiation, but should here also consider the time or pulse structure of the radiation. This difference is expressed with the relative biological effectiveness (RBE)

$$\mathrm{RBE} = \left.\frac{D_\mathrm{reference}}{D_\mathrm{test}}\right|_{\text{same biological effect}},$$

which relates two doses ($D_\mathrm{reference}$ and D_test) causing the same effect under identical conditions, but applied using different radiation qualities, to one another.

In general, a biological effect is related to the radiation's potential to induce damage, but also to the biological system's ability to repair said damage. Therefore, the RBE relates two radiation qualities, but is also dependent on the exact biological effect considered, possibly depending on cell line, biological endpoint or milieu conditions.

2.1.3 Radiation Therapy vs. Radiation Protection

Dosimetry, in both radiation therapy as well as radiation protection, aims to provide a measurement based on which an assessment of the biological effects may be made. The two application fields differ significantly, however, in the dose and dose rates of concern and the required generalizations of the measurement.

Clinical dosimetry for radiation therapy aims to determine the direct output of an irradiation device, delivering – in one session – a dose of typically a few Gy with a dose rate of several Gy/min. Based on those measurements a detailed dose calculation for each individual patient is performed. Radiation protection dosimetry, on the other hand, is concerned with the estimation of the radiation exposure of the environment or personnel, where the primary source is typically shielded, attenuating the dose rate to below a few mGy/h with yearly doses of several mGy at most. It aims to provide a general assessment of the risks associated with the exposure to a certain radiation field, independent of individual anatomy.

As a consequence of the different doses and dose rates of concern in the two applications of dosimetry, they require instruments of different sensitivity. Where clinical dosimetry mostly employs ionization chambers, directly measuring the radiation induced ionizations in air (detailed in section 2.3), dose rate meters employed for radiation protection measurements typically require some form of charge multiplication or denser detection materials than air to generate sufficient signal (see section 2.5).

Radiation therapy utilizes a well defined beam, many properties of which are known. Clinical dosimetry aims to provide an exact measurement of the physically applied dose from this primary beam, typically as absorbed dose in water D_{w}. Based on this measurement the RBE and its dependencies may be considered for each individual treatment.

This is starkly contrasted by the requirements of radiation protection. The primary beam is typically shielded, making scattered and secondary radiation the primary concern. Consequently, the radiation field is characterized in less detail and individualized risk assessment is neither possible nor truly required.

Therefore, radiation protection measurements attempt to incorporate RBE into the reported quantity, by reporting a *dose equivalent* H, which is the absorbed dose multiplied with a dimensionless quality factor accounting for differences in RBE of different radiation qualities (DIN, 1985; ICRP, 2007). Due to the dependence of RBE on the effect under consideration and the low doses of interest in radiation protection, this consideration is limited to carcinogenic and germline mutations, which have no known lower dose limit for their occurrence (ICRP, 2007). To emphasize the consideration of the quality factor, dose equivalent is expressed in Sv, although it has the same dimension as absorbed dose (J/kg).

The established measurement quantity for the purpose of ambient dose measurements of penetrating radiation – in radiation protection this primarily entails high energy photons and neutrons – is the ambient dose equivalent $H^*(10)$. It is a dose equivalent measured under certain conditions. Specifically, $H^*(10)$ at a measurement point is the equivalent dose that would be absorbed in a specific, tissue equivalent sphere of 30 cm diameter – the ICRU sphere (ICRU, 1985) – in 10 mm depth, if the entire sphere were to be exposed to a homogeneous radiation field of the same characteristics as the field at the measurement point. This somewhat convoluted definition aims to provide an acceptable estimate for the dose a human would receive, while also providing a well defined setup for instrument calibration that is simple enough to implement in calculations (Krieger, 1998).

While these consideration of the measured quantity are highly relevant for dosimetry in general, they are largely irrelevant for the problems faced by highly pulsed fields. As discussed in the following sections, in particular 2.3 and 2.5, the key concern there is the response of the instruments and their ability to cope with a highly variable dose rate.

2.2 Pulsed Radiation

2.2.1 Terminology

As stated in the introduction pulsed radiation fields are ubiquitous in medical application. Before detailing their sources and the challenges posed by them, though, a clear definition of a pulsed field and its defining parameters is in order.

At first glance a pulsed radiation field is easily defined as a field whose dose rate or intensity is intermittent and characterized by sudden changes, while a continuous radiation field is characterized by a constant dose rate. However, this immediately brings about the question at what point a change is sudden or so gradual that the dose rate is essentially constant? The answer critically depends on the timescale under consideration. For example, a measurement instrument usually has the capability to detect gradual intensity changes as measurements at different positions in a radiation field are taken, but may fail to accurately measure a rapidly changing dose rate. However, where this limit lies, depends on the specific instrument, the physical principle it is based on and the form of signal processing used.

One important limit on what constitutes a rapid change is set by the German certification authority for radiation measurement equipment, the Physikalisch-Technische Bundesanstalt (PTB). The PTB considers a field whose dose rate stays constant for less than 10 s as pulsed (DIN, 2013). Considering physical processes, 10 s is a very long time and this limit is not necessarily the limit of any actual instrument, but, since it is the limit for which all radiation protection instruments in Germany were certified, it is relevant to keep in mind. Generally speaking, though, the question of what timescale constitutes a pulsed field has to be viewed in relation to the instrument or detection process under consideration.

In order to discuss those individual limits, it is useful to define a few parameters to describe the time dependence of the dose rate of a pulsed field. In principle this time dependence can take any shape imaginable and determining well defined parameters is only possible by generalizing it in some form. For example, the recently formulated definition of pulsed reference fields in ISO/TS 18090-1 (ISO, 2015) uses a trapezoid to approximate the pulse shape, defines a procedure how to fit a trapezoid to the real pulse shape and then defines characteristic parameters based on that fitted trapezoid. For the purpose of this work it will be sufficient to consider the field as a regular succession of pulses with a rectangular

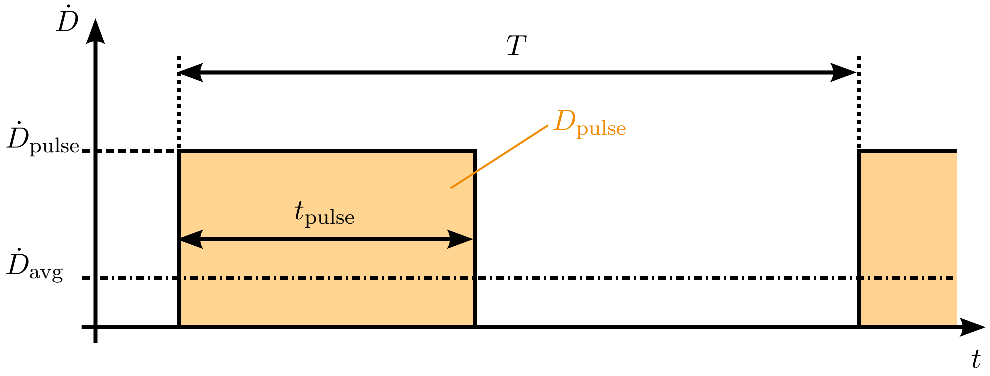

Figure 2.1: Dose rate over time of an idealized pulsed radiation field, illustrating the parameters used to describe the time structure of the field.

dose rate profile (see Fig. 2.1), using the following parameters for their description:

- The pulse-duration t_pulse is the width of the rectangle.
- The dose-per-pulse D_pulse is the cumulated dose of the entire pulse (i.e., the area under the curve of one pulse).
- The pulse dose rate $\dot{D}_\text{pulse}$ is the dose rate during the pulse: $\dot{D}_\text{pulse} = \frac{D_\text{pulse}}{t_\text{pulse}}$.
- The pulse period T is the time between two consecutive pulses and the repetition rate $f_\text{rep} = T^{-1}$ is its inverse.
- The mean dose rate $\dot{D}_\text{avg}$ is the dose rate averaged over one pulse period: $\dot{D}_\text{avg} = \frac{D_\text{pulse}}{T}$.

The definition of a pulse shape is only necessary for the definitions of the pulse duration and the pulse dose rate. When discussing more irregular pulse shapes, such as a Gaussian, t_pulse will be used to denote the full width at half maximum (FWHM) duration of the pulse and the pulse dose rate will only be used in the context of rectangular pulses. Additionally, analog terms for dose equivalents H_pulse, $\dot{H}_\text{pulse}$ and $\dot{H}_\text{avg}$ will be used.

Using these parameters, two limiting cases are helpful in order to consider the transition from a continuous to a pulsed field: First, a continuous field that is turned on and off is the same as a pulsed field with a long pulse-duration. Thus, the effects of a pulsed field, when increasing the pulse duration, should gradually transition to the effects of a continuous field, for example, pulses with a duration longer than 10 s should be correctly measured by certified radiation protection equipment.

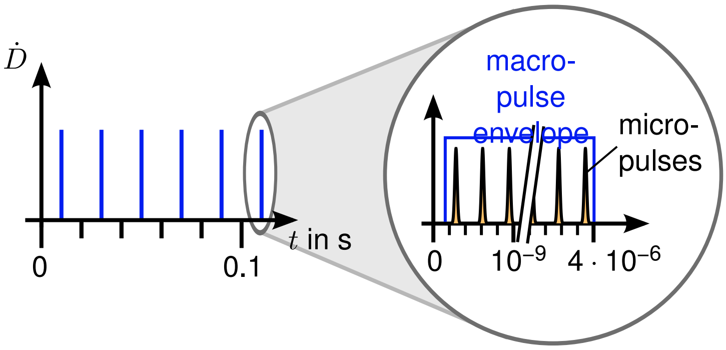

Figure 2.2: Illustration of the typical combined macro and micro-pulse structure of a clinical LINAC. Due to the range of times involved from 10^{-10} s to 0.1 s, drawing micro and macro-pulses on a single time axis is not possible.

Second, for an instrument or a detection process under consideration, a rapid succession of pulses will be indistinguishable from a continuous field if the time between the pulses is too short to be resolved. Thus, a field with a very rapid succession of pulses is termed quasi continuous, if the pulse structure is not observable from the perspective of the process under consideration.

2.2.2 Sources

Pulsed radiation sources exist beyond the medical application, for example, in the form of research installations such as the Electron LINAC for beams with high Brilliance and low Emittance (ELBE) at the Helmholtz-Zentrum Dresden-Rossendorf. This thesis is focused, however, on sources intended for medical application, specifically those for EBRT.

Present day EBRT in the western world predominantly uses electron LINACs to generate high energy photon fields and to a lesser extent to deliver electron fields (Grau et al., 2014). In addition, protons are slowly adopted, accelerated in cyclotrons or synchrotrons and recently also synchrocyclotrons (PTCOG, 2016).

The principle acceleration process in all these accelerators generates a quasi continuous radiation field because charged particles are accelerated in a cavity using a resonant, high frequency, alternating electric field in the MHz to GHz range, resulting in beams where the particles are compressed into bunches or pulses of the same frequency. Onto this high frequency pulse structure of micro-pulses, inherent to the acceleration process, an additional lower frequency macro-pulse structure is often superimposed, illustrated in Fig. 2.2.

The Siemens Artiste LINAC used for radiation therapy, for instance, produces an electron beam with a micro-pulse repetition rate of 3 GHz. However, in order to limit the heat produced in the accelerator it is only operated for roughly 4 µs at a time every 20 ms, equaling a macro-pulse repetition rate of 50 Hz.

In the contexts considered here, macro-pulses are the relevant time structure and are referred to as pulses. Unless otherwise specified, the micro-pulse time structure is considered to be equivalent to a continuous field.

In addition to the accelerator, the medical application of a beam may also impose a pulse structure, for example, in the application of protons or heavier ions. A focused, mono-energetic ion beam deposes most of its dose in a small volume in a specific depth. It needs to be modulated in energy and spread laterally to cover an entire tumor. Lateral spread may be achieved by actively steering the focused beam to irradiate successive small volumes for short durations each, called pencil beam scanning, or by broadening the beam via scattering, irradiating the entire lateral extent at once, called passive field formation or double scattering. Energy modulation in pencil beam scanning is typically also active, irradiating successive, discrete layers, whereas double scattering often uses an energy modulation fixed in range and frequency (from rotating a wheel of varied thickness), such that the beam must be pulsed to use only the energy and thus depth range relevant for the patient at hand.

Consequently, both dose delivery techniques – pencil beam scanning and double scattering – result in a pulsed beam. Furthermore, the dose delivery technique influences the dose-per-pulse. Spreading the intensity over a large volume in double scattering results in smaller doses to a large volume, while a focused pencil beam results in large doses applied to small volumes.

Table 2.1 lists the parameters defining the time structure of a few sources in medical application. Next to the ubiquitous LINAC are two sources for proton beams currently deployed or on the outset of commercial availability, serving to illustrate two extremes in regard to dose-per-pulse. On the one hand, a cyclotron is a principally continuous source, pulsed only due to the passive field formation with a low dose-per-pulse. On the other hand, a synchrocyclotron operates inherently pulsed and in pencil beam scanning would deliver a relatively large dose-per-pulse. Furthermore, the possible parameters of a laser based accelerator are shown and an angiography X-ray machine, used for live imaging, to provide an example of a non radiation therapy pulsed source.

Table 2.1: Comparison of the pulse parameters of 5 exemplary pulsed radiation sources used in medical application and research. The values are intended to be representative of the class of sources and may be different for any specific system.

	Laser accelerator[1]	Synchro-cyclotron[2]	Cyclotron[3]	Electron LINAC[4]	Angiography X-ray[5]
dose-per-pulse	∼ Gy	∼ 0.5 Gy	4 mGy	1 mGy	0.1 mGy
pulse-duration	∼ ps	2–10 µs	2–10 ms	4 µs	2 ms
repetition rate	∼ 10 Hz	1 kHz	10 Hz	50–300 Hz	20–30 Hz
micro-pulse rate	-	60 MHz	100 MHz	3 GHz	-

[1] Order of magnitude estimates for a possible clinical system based on the considerations given in Linz and Alonso (2007) and Zeil et al. (2010).

[2] Values for the IBA S2C2 proton synchrocyclotron according to Krimmer et al. (2017). The dose-per-pulse was estimated assuming pencil beam scanning dose delivery mode.

[3] Based on measurements of the IBA C230 proton cylcotron at OncoRay, Dresden in double scattering dose delivery mode.

[4] Based on values given in Podgorsak (2005) and measurements on a Siemens Artiste system.

[5] According to appendix A in DIN IEC/TS 62743 (DIN, 2013).

A laser based accelerator delivers very intense and very short charged particle pulses (i.e., the dose-per-pulse is very large and the pulse-duration short compared to the LINAC) making the laser based accelerator an extreme example of a pulsed radiation source. X-ray tubes on the other hand are in principle prime examples of continuous sources, but they are often pulsed when used for live imaging. X-ray images in those systems are acquired with a rate of 20–30 Hz because that rate is sufficient for the illusion of fluidity. Consequently, the X-ray source is pulsed with the same rate to minimize the applied dose. While such sources have much lower average dose rates than those used for therapy, personnel are exposed much more directly to them, increasing the risk of accidental exposure.

An additional source not listed in table 2.1, but of interest due to its intermediary position regarding dose-per-pulse, are LINACs used for intraoperative radiation therapy (IORT). From a construction standpoint, these sources are identical to LINACs used for external beam therapy, resulting in a field with the same micro and macro-pulse time structure, pulse duration and repetition rate. Yet, their application during surgery allows bringing the IORT-LINAC in direct proximity of the target volume. This enables an increase in the dose-per-pulse up to 100 mGy (di Martino et al., 2005) because the available radiation is focused onto a smaller area and because it allows the use of the direct electron beam of the LINAC instead of converting it to photons, which have better penetrating ability required in EBRT.

The examples given in table 2.1, with keeping in mind that LINACs with increased dose-per-pulse for IORT exist, should give a good overview of the spectrum of pulsed radiation sources encountered in clinical use. Those range from X-ray imaging sources, using relatively long pulses with a low average dose rate, over the current radiation therapy sources, using an intermediate pulse-duration, to the next generation sources such as a synchrocyclotron and laser based accelerator, with a very short pulse-duration and very high dose-per-pulse. In particular, this last source highlights the challenges dosimetry might face, as it provides dose-per-pulse values up to three orders of magnitude higher than current sources, with pulse dose rates even higher, due to the considerably reduced pulse duration. The following sections will discuss the specific challenges this poses to radiation protection and clinical dosimetry respectively.

2.3 Ionization Chambers for Radiation Therapy Dosimetry

Clinical dosimetry for radiation therapy requires a high level of accuracy with a total uncertainty of at most 3–4 % (Krieger, 2001), because of the need to target the relatively small therapeutic dose window, where the trade off between controlling the tumor and inducing side effects is optimally balanced (Fig. 1.1). Errors in the dosimetry will have direct consequences for patients by either delivering too little dose to a tumor, thereby reducing the chances for treatment success or by applying too much dose to healthy tissue and inducing more side effects than acceptable.

The most widely used radiation detector to achieve this level of accuracy is the ionization chamber (IC). As the name implies it detects the ionizations central to the effects of ionizing radiation (see section 2.1.1). While ionization chambers were not immediately used in clinical application, nowadays, a century of construction refinements has produced detectors of unparalleled long term stability and robustness. Such a highly reliable detector may be calibrated to provide very accurate absolute dose measurements. Additionally, it is relatively simple to construct and operate and its behavior is generally well understood, simplifying modeling and computations.

Ionization chambers can be machined in various shapes to fulfill different dosimetric tasks, further contributing to their widespread use. Small chambers can be produced to measure inhomogeneous fields, as encountered in intensity modulated radiation therapy

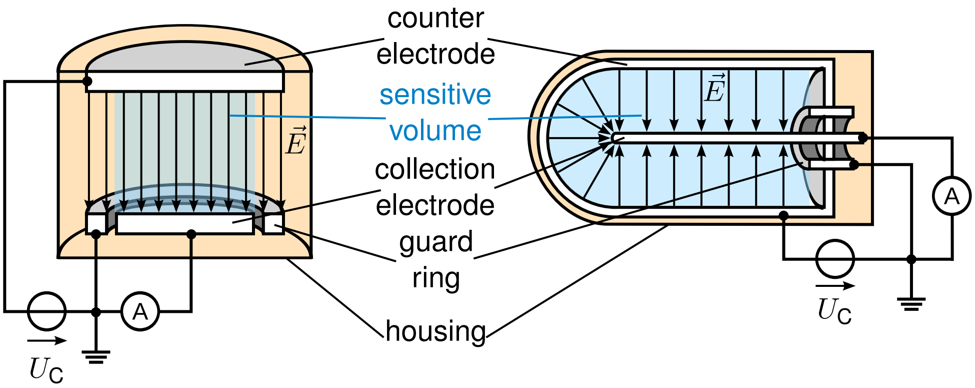

Figure 2.3: Schematic drawing of the two most common ionization chamber geometries: the plane parallel geometry on the left and the thimble geometry on the right.

(IMRT), either as thimble-shaped or as plane-parallel chambers. On the other hand, large diameter plane-parallel chambers are used to capture the entirety of a proton pencil beam, which is broadened significantly towards its end, due to lateral scattering.

Considering these advantages and the vast legacy the ionization chamber has in radiation therapy it is only sensible to try to adapt the usage of ionization chambers to novel, pulsed radiation sources, rather than developing entirely new detector systems.

2.3.1 Principle of Operation

In an ionization chamber an electric field is formed in a sensitive volume by applying a potential across at least two electrodes. Charges liberated by ionizing radiation within this sensitive volume drift in the electric field, inducing a measurable current in the ionization chamber's electrodes.

Figure 2.3 sketches the two most common ionization chamber construction types, the plane-parallel chamber and the thimble type chamber. In both cases a collection electrode, from which the signal is taken, and a counter electrode, to which a potential is applied, define a sensitive volume, wherein the ionization is measured. In principle, both collection and counter electrode maybe either cathode or anode, in dependence of the applied voltage. The accuracy of delimiting this sensitive volume is improved by adding a third electrode, the guard ring, which is held on the same potential as the collection electrode. It eliminates most of the fringe field effects at the edge of the collection electrode, thereby ensuring that charges outside the sensitive volume do not reach the collection electrode, but instead flow through the guard ring.

Additionally, without a guard ring a significant current, in comparison to the current due to ionizations, would flow across the insulation between collection and counter electrode. This is due to the very small ionization currents on the order 10^{-12} A and due to the finite resistance of any insulator, in particular in the face of surface contamination. With a guard ring this leak current flows mostly through the guard ring. The potential difference between the guard ring and collection electrode is practically zero and the current measurement taken between them reflects the pure ionization current (Knoll, 2000).

The inner volume, including the sensitive volume, is most often filled with a gas, sometimes also a liquid is used. While different gases can be used for different applications, in radiation therapy, air vented chambers are used almost exclusively. These chambers are typically open to the surrounding atmosphere because such a construction is much simpler and more easily maintained than the alternative of a sealed inner volume. In some cases non-polar liquids, such as isooctane (2,2,4-trimethylpentane) or tetramethylsilane (TMS), have also found use as active media in radiation therapy. They provide a measurable ionization current from a much smaller volume, due to the much higher mass density of these media compared to air, resulting in a higher ionization density. The small sensitive volume makes liquid ionization chamber (LIC) ideal to measure small or inhomogeneous fields.

As radiation interacts with the medium in the sensitive volume the ionization results in the liberation of ion-electron pairs. These charge carriers, initially positively charged ions and negatively charged electrons, are accelerated in opposite directions and separated by the electric field spanned by the electrodes of the ionization chamber. During the collection process the molecules of the medium and also the charge carriers undergo repeated collisions, due to their thermal motion. As a result, the charge carriers are not accelerated to an ever increasing velocity, but instead transfer momentum and kinetic energy to other molecules in each collision. The repeated process of collision and acceleration leads to an effectively constant drift velocity of the charges, when considering an entire swarm of ions or electrons.

These drifting charges induce the current in the collection electrode, which is measured with an ammeter or electrometer attached to the ionization chamber. This instantaneous current, induced by a charge moving in the vicinity of the conductor, can be calculated using the Shockley-Ramo theorem (Shockley, 1938; Ramo, 1939). However, it can also be shown that for a two electrode setup as used in an ionization chamber, the time integral of the instantaneous current over the duration of the charge collection is equal to the amount of charge collected at that electrode (Hochhäuser, 1993). Thus, when considering the total measured charge and not the actual current, it is viable to equate the measured charge with that arriving at the collection electrode, that is the collected charge of one sign.

In addition to momentum transfer, more transformative reactions take place during the repeated collisions of the charge carriers with neutral molecules and with each other. In a charge transfer collision, the charge is moved from one carrier to another, for example in air $N_2^+ + O_2 \rightarrow N_2 + O_2^+$.

For media containing molecules which form stable negative ions electron attachment occurs. In air this is foremost the attachment to O_2 with the assistance of a third collision partner for energy and momentum conservation: $e^- + O_2 + M \rightarrow O_2^- + M$. The resulting negative ions still carries the charge but drifts much more slowly in the electric field, due to the much higher mass of the ion compared to the free electron.

Finally, collisions between charge carriers of opposite sign may lead to a recombination and mutual neutralization of the charge, for example, of the form $N_2^+ + O_2^- \rightarrow N_2 + O_2$. Such recombination causes the measured charge (Q_c) to be less than the amount originally liberated by radiation (Q_0) and needs to be taken into account when performing ionization chamber measurements. The likelihood of such recombination increases with an increased ionization density, as collisions between opposing charge carriers become more likely. Thus, it is particularly important for highly pulsed fields, where a high ionization density is created in a short time and this volume recombination is at the focus of this investigation.

2.3.2 Calibration and Correction Factors

An ionization chamber measures liberated charge in, usually, air, but the goal of a dosimetric measurement is to determine absorbed energy per unit mass (dose) in, preferentially, water. Commonly, a probe method is employed in order to relate the two quantities.

The ionization chamber is inserted into the medium of interest – usually water – forming a small cavity in the medium. Ideally, the insertion of the cavity (the ionization chamber) has only minimal impact on the radiation field. At the same time the secondary radiation field and energy deposition inside the chamber's sensitive volume should be determined by the gas or liquid used to fill the chamber. This leads to the requirement of a balance of in- and outflow of certain (secondary) radiation types with respect to the sensitive volume of the ionization chamber. For the high energy photons, electrons and charged particles typical of EBRT, this balance is formulated as the Bragg-Gray condition, originally developed for photons (Gray, 1936). Irrespective of the details of this balance, it should be clear that it places certain requirements on the construction of the ionization chamber, in particular the wall materials and thickness. Furthermore, the balance and minimal perturbation is only ever approximated and cannot be achieved for all kinds of radiation simultaneously limiting the applicability of an ionization chamber to the radiation type and energy is was designed for.

While it is possible to calculate the dose to water from a chamber under the Bragg-Gray condition, which was calibrated for measurements of liberated charge in air (radiation exposure), such an approach involves several conversions and tabulated values, introducing a large amount of uncertainty. The preferred and currently recommended approach (Almond et al., 1999; Andreo et al., 2000; DIN, 2008) is to directly calibrate the ionization chamber for absorbed dose in water, by comparing it to a reference dose measurement, traceable to the primary national standard in a reference field. Typically, this calibration factor N_w is determined by the manufacturer. It is, however, exact only under the precise conditions of the reference measurement, requiring correction factors to account for the differences between the condition of the measurement and the calibration.

For high energy photon beams DIN 6800-2 (DIN, 2008) lists the full measurement equation as

$$D_\mathrm{w} = (M - M_0) \cdot N_\mathrm{w} \cdot \prod_i k_i, \tag{2.1}$$

with the ionization chamber measurement M and the zero reading M_0. Dimensionless correction factors k_i are employed for example for air density (k_ρ), chamber polarity (k_p) and beam quality (k_q). DIN 6800-2 (DIN, 2008) views these correction factors as independent from one another. Therefore, it is possible to consider the effects of pulsed radiation independently from the other factors and analyze its effects independent of radiation quality or other factors influencing the dosimetry.

In the context of pulsed radiation the saturation correction factor k_s is the most important of these factors. The term saturation correction arises from the typical behavior of the current measured with an ionization chamber. Increasing the applied voltage from zero causes an increasingly diminished rise of the current that approaches a saturation level. Typically, ionization chambers are operated with a voltage resulting in a saturation current.

The onset of charge multiplication, though, sets an upper limit on the applicable voltage (see section 2.5.1 and Fig. 2.6).

Ideally, reaching the saturation current implies a collection of all the charges liberated. However, due to the recombination effects described in section 2.3.1 this may not be the case and such a situation is termed incomplete saturation. This incomplete saturation is corrected for by the saturation correction factor k_s, which is consequently defined as the ratio of liberated to collected charge,

$$k_\mathrm{s} = \frac{Q_0}{Q_\mathrm{c}}. \tag{2.2}$$

Since the ionizations from pulsed radiation occur in a short amount of time, such radiation has the potential to cause a very high density of liberated charge, which would cause a high amount of recombination and a large, and therefore highly relevant, k_s.

2.3.3 Saturation Correction and Volume Recombination

Describing the recombination effects giving rise to incomplete saturation requires a closer look at the processes taking place. These processes can broadly be categorized into two classes: initial and volume recombination. Initial recombination considers the effects that depend on the microscopic charge distribution directly following the ionization. Those are the recapture of an electron by its parent ion, described by Onsager (1938), or the recombination within the track of a single ionizing particle, described by Jaffé (1913). Volume or, as it is at times referred to, general recombination considers effects after those charges have diffused to form a macroscopic charge distribution corresponding to the beam profile. For ionization chamber dosimetry this is usually a homogeneous charge distribution in the chamber volume.

Since initial recombination considers only the effect of a single primary particle, it is unaffected by the primary particle flux and thus also dose rate or dose-per-pulse. Additionally, initial recombination is typically negligible in air at atmospheric pressure, except in the case of high linear energy transfer (LET) radiation (Boag, 1987). Conversely, volume recombination is very much affected by the dose rate and the primary particle flux. Therefore, in the following, only the contribution from volume recombination to k_s is considered, neglecting the other contributions.

For a given Q_0, which may be considered as the liberated charge of one sign after any initial recombination effects, k_s is calculated by determining the collected charge of one sign Q_c (eq. (2.2)). Determining Q_c essentially requires determining the evolution of the density of charges of one sign $\rho_+(\vec{r},t)$ or $\rho_-(\vec{r},t)$ in space and time. Integrating ρ_+ or ρ_- over the area of the collection electrode and the duration of the charge collection would give Q_c, with the sign of the applied collection voltage determining whether ρ_+ or ρ_- must be used.

The symmetry of a plane-parallel chamber under homogeneous irradiation allows the reduction of this principally 3-dimensional problem to a single dimension. The density of liberated charges is constant in each plane perpendicular to the electrodes, and, without an electric field component to induce any change, it will remain as such over the duration of the collection process. Consequently, the only relevant dimension is perpendicular to the plane of the electrodes and will be referred to as x.

A similar consideration is possible for cylindrical and spherical geometries. Charge drift in those chambers is purely radial. Yet, the circumferential compression of the charges as they move inward must be considered. Typically, those geometries are discussed as generalizations of the plane-parallel geometry, an approach that will be employed here as well.

In order to properly account for the interaction between charges of opposite sign, both ρ_+ and ρ_- must be considered simultaneously, even if the result for one would be sufficient. In addition, the charge density of one sign liberated by irradiation in any medium is made up of different charge carriers with varied concentrations $c_i(x,t)$ and properties, for example,

$$\rho_-(x,t) = \sum_{q_i<0} q_i c_i(x,t),$$

where q_i is the charge carried by carrier i.

Taking into account all the different charge carriers created when air is ionized by radiation is almost impossible. For instance, Kossyi et al. (1992) consider in their model of discharges in nitrogen-oxygen mixtures 9 positive ions and 6 negative ones, in addition to several excited states of the neutral molecules. In air additional considerations would have to be made for at least water vapor, probably also CO_2 and some of the other trace gases, as well as the compounds formed by their ions and nitrogen and oxygen. To eventually describe their influence, a parametrization of each constituent's properties would be needed, which seems hardly feasible. Therefore, the consideration is limited to positive ions (c_+), negative ions (c_-) and free electrons (c_e), leaving one carrier for each charge sign and additionally the electrons, because their behavior is fundamentally different from any ion.

In order to describe the time evolution of the charge density, two main process need to be considered. The drift of the charge carriers in the electric field and the interactions between the different charge carriers described in section 2.3.1.

The drift of the charges in the electric field is best described by an advection equation, derived from mass conservation (Hundsdorfer and Verwer, 2003). Consider a concentration $c(x,t)$ of a charge carrier species, with a space variable $x \in \mathbb{R}$ and time t. A small spatial cell of size h, centered around position x is given by the interval $[x - \frac{1}{2}h, x + \frac{1}{2}h]$. The average concentration $\overline{c}(x,t)$ in that cell can be written as

$$\overline{c}(x,t) = \frac{1}{h}\int_{x-\frac{1}{2}h}^{x+\frac{1}{2}h,} c(s,t)ds = c(x,t) + \frac{1}{24}h^2\frac{\partial^2}{\partial x^2}c(x,t)\ldots \tag{2.3}$$

resolving the integral by expanding $c(s,t)$ around x.

Due to the drift of the charge carriers there is a flow with the speed $v(x,t)$ across the cell boundaries. Mass conservation requires the difference in in- and outflow to be equal to the change in concentration in the cell, resulting in

$$\frac{\partial}{\partial t}\overline{c}(x,t) = \frac{1}{h}\left[v(x-\frac{1}{2}h,t)c(x-\frac{1}{2}h,t) - v(x+\frac{1}{2}h)c(x+\frac{1}{2}h,t)\right]. \tag{2.4}$$

Inserting eq. (2.3) into eq. (2.4) and letting $h \to 0$, one arrives at the advection equation

$$\frac{\partial}{\partial t}c(x,t) = -\frac{\partial}{\partial x}\left(v(x,t)c(x,t)\right). \tag{2.5}$$

This equation is easily generalized to three dimensions using a gradient operator, however, for a plane-parallel chamber one dimension is sufficient.

The concentration changes of the charge carrier species due to reactions is proportional to the concentrations of the involved carriers, according to the law of mass action. In the case of recombination of positive and negative ions this means

$$\frac{\mathrm{d}c_+}{\mathrm{d}t} = \frac{\mathrm{d}c_-}{\mathrm{d}t} = -\alpha c_+ c_-$$

using a recombination rate constant α (Knoll, 2000).

The attachment of electrons to O_2 forming negative ions follows a similar equation

$$\frac{\mathrm{d}c_-}{\mathrm{d}t} = -\frac{\mathrm{d}c_e}{\mathrm{d}t} = \gamma c_e.$$

However, the concentration of O_2 is practically unaffected by the electron attachment, because it is several orders of magnitude larger than the electron concentration. It is therefore omitted from the equation, folding its contribution into the attachment rate constant γ.

The desired description of the charge concentration's time evolution in the sensitive volume of the ionization chamber is achieved by combining these reaction terms with the advection equation above and adding a source term for the liberation of ion-electron pairs by radiation $R(t)$. Furthermore, the drift velocity is expressed in terms of a mobility μ with

$$v_i = \mu_i \cdot E, \tag{2.6}$$

which expresses the dependence of the drift velocity on the electric field strength E, resulting in the equation system (Karsch and Pawelke, 2014)

$$\begin{aligned}
\frac{\partial c_+}{\partial t} &= +R(t) \qquad -\alpha c_+ c_- - \frac{\partial(E\mu_+ c_+)}{\partial x} \\
\frac{\partial c_-}{\partial t} &= \qquad + \gamma c_e - \alpha c_+ c_- - \frac{\partial(E\mu_- c_-)}{\partial x} \\
\frac{\partial c_e}{\partial t} &= +R(t) - \gamma c_e \qquad - \frac{\partial(E\mu_e c_e)}{\partial x}.
\end{aligned} \tag{2.7}$$

Historically, similar systems have been derived, usually considering only positive and negative ions, and have been solved for the limiting cases of continuous irradiation ($R(t) = const.$) (Mie, 1904) and idealized short pulses ($R(t) = \delta(t) \cdot const.$, with δ denoting the Dirac delta function) (Langevin, 1902). In the latter case, $R(t)$ can be removed from the equation and instead a constant initial charge concentration is assumed ($c_+(x,0) = c_-(x,0) = const.$). Using these approximations, the solution for pulsed irradiation takes the form (Boag, 1950)

$$(k_\mathrm{s})_\mathrm{th} = \frac{aQ_0}{\ln(1 + aQ_0)}, \tag{2.8}$$

where a is a parameter characterizing the chamber and its filling gas, defined as

$$a = \frac{\alpha d^2}{e(\mu_+ + \mu_-)U_c V}, \tag{2.9}$$

with the distance between the electrodes d, elementary charge e, volume of the chamber V and collection voltage U_c.

Boag (1950) also calculated solutions for cylindrical and spherical geometries. He argued that the circumferential compression of the charges is exactly balanced by a radial stretching due to the increased electric field and velocity closer to the center. Hence, the solutions take an identical form to eq. (2.8) if the electrode distance d is replaced with an effective value. For a cylindrical chamber with an inner (i.e., collection electrode) radius r_1 and an outer (i.e., inner counter electrode) radius r_2 this effective value is

$$d_{\mathrm{cyl}} = (r_2 - r_1)\sqrt{\frac{r_2 + r_1}{r_2 - r_1}\frac{\ln r_2/r_1}{2}}.$$

An important simplification involved in Boag's (1950) solution is ignoring the dependence of E on the total charge density $\rho = \rho_+ + \rho_-$ and thus on the concentrations c_i. Boag (1950) showed that for a pulsed irradiation and typical charge densities used in clinical practice at that time, the effect of this simplification is negligible. He also expanded Langevin's (1902) work by deriving solutions for spherical and cylindrical chambers, showing that they can be described by an identical expression to the plane-parallel chambers if the electrode distance is replaced by an effective value (Boag, 1950).

In much later work the original expression of eq. (2.8) was amended to also consider the process of electron attachment, giving the currently best published description of k_{s} (Boag et al., 1996). When considering only positive and negative ions it was usually assumed that all electrons attach immediately to form ions. Enabled by the work of Hochhäuser (1993) on the electron attachment in air, Boag et al. (1996) modified this assumption by introducing a fraction of free electrons p which do not attach and are collected without loss. Three expressions for different assumptions regarding the resultant negative ion concentration were derived, with all symbols retaining their meaning from eq. (2.8).

$$(k_{\mathrm{s}})'_{\mathrm{th}} = \frac{aQ_0}{\ln\left(1 + \frac{e^{paQ_0} - 1}{p}\right)} \tag{2.10}$$

$$(k_{\mathrm{s}})''_{\mathrm{th}} = \frac{aQ_0}{paQ_0 + \ln\left(1 + (1-p)aQ_0\right)} \tag{2.11}$$

$$(k_{\mathrm{s}})'''_{\mathrm{th}} = \frac{aQ_0}{\lambda aQ_0 + \ln\left(1 + \frac{e^{\lambda(1-\lambda)aQ_0} - 1}{\lambda}\right)}, \lambda = 1 - \sqrt{1-p} \tag{2.12}$$

The model for the negative ion concentration leading to eq. (2.10) is a homogeneous, but compared to the positive ions reduced, concentration of $c_-(x) = (1-p)\,c_+(x)$. For eq. (2.11) a negative ion concentration is assumed which consist of a region in front of the cathode devoid of negative ions of a width $p\,d$ and $c_-(x) = c_+(x)$ in the remaining volume. The last solution, eq. (2.12), assumes a combination of the two previous distributions: A region devoid of negative ions and a reduced concentration in the remaining volume (Boag et al., 1996).

In current clinical practice, where dose-per-pulse is low (typically $<4\,\mathrm{mGy}$), neither of these expressions is commonly used, because the parameters determining a were shown to be dependent on the chamber and experimental conditions (ICRU, 1982). Instead the voltage dependence of an approximation of k_s is utilized. Assuming p is independent of Q_0, a first order approximation of, for example, eq. (2.10) reads:

$$(k_\mathrm{s})'_\mathrm{th} \approx 1 + \frac{aQ_0(1-p)}{2} \tag{2.13}$$

Since $a \propto 1/U_\mathrm{c}$, instead of $\frac{a(1-p)}{2}$ one can write $\frac{b}{U_\mathrm{c}}$. This relationship, with different definitions for b, may be derived from any of the eqs. (2.8), (2.10), (2.11) or (2.12). By also inserting the definition of k_s from eq. (2.2) and dividing by Q_0, eq. (2.13) is transformed to

$$\frac{1}{Q_\mathrm{c}} = \frac{1}{Q_0} + \frac{b}{U_\mathrm{c}}.$$

This approximate voltage dependence does not require the consideration of a free electron fraction and is valid for all the expressions given for k_s, including $(k_\mathrm{s})_\mathrm{th}$. A method known as the Jaffé-plot uses this relation by plotting inverse ionization chamber measurements ($1/Q_\mathrm{c}$) over inverse collection voltage ($1/U_\mathrm{c}$), which gives the liberated charge without recombination losses as the axis intercept of a linear fit. The Jaffé-plot is the recommended method to determine k_s for a chamber where tabulated values for k_s are not available (Almond et al., 1999; Andreo et al., 2000; DIN, 2008). Directly using any of eqs. (2.10), (2.11) or (2.12) is usually not possible, because determining the parameters a and p is not universally possible. A generally accepted and often performed approximation for low k_s (i.e., k_s close to 1) is to only measure two voltages and directly calculate the fit from those points, which is known as the two voltage approximation (TVA) (Almond et al., 1999; Andreo et al., 2000; DIN, 2008).

These established procedures work well for the dose-per-pulse values produced by typical LINACs of a few mGy. Different methods have been proposed to deal with higher dose-per-pulse values encountered in IORT up to 100 mGy. Di Martino et al. (2005) suggested to fit $(k_\mathrm{s})'_\mathrm{th}$ to reference measurements to obtain effective values of a and p and use those as a basis to calculate k_s for a measurement. However, determining the dose with an independent method in a reference measurement is rather time consuming. Therefore, Laitano et al. (2006) suggested to instead calculate p and modify the two voltage method to calculate a. Assuming a constant electric field throughout the volume of a plane-parallel chamber, the free electron fraction p is easily derived as (Boag, 1987):

$$p = \frac{\mu_e E}{\gamma d} \left(1 - e^{-\frac{\gamma d}{\mu_e E}}\right) \tag{2.14}$$

For two measurements of the same radiation field at two collection voltages ($M(U_1)$, $M(U_2)$) the relation

$$k_\mathrm{s}(U_1)M(U_1) = k_\mathrm{s}(U_2)M(U_2)$$

is true. Using any of the expressions $(k_\mathrm{s})'_\mathrm{th}$, $(k_\mathrm{s})''_\mathrm{th}$ or $(k_\mathrm{s})'''_\mathrm{th}$ and the calculated value of p it is possible to numerically solve for a and thus derive k_s. Laitano et al. (2006) found best agreement with experimental data using $(k_\mathrm{s})'''_\mathrm{th}$ and a k_s calculated in this way will be denoted as $(k_\mathrm{s})'''_\mathrm{L}$ here. Subsequent publications, which compared those approaches (Cella et al., 2010; Ghorbanpour Besheli et al., 2016), found reasonable agreement between those calculations and measurement, but tended to attest di Martino et al.'s approach a better agreement with the experimental data.

At even higher dose-per-pulse values beyond a 100 mGy the validity of the eqs. (2.10) to (2.12) themselves, which underly all these approaches, must be questioned. All of the negative ion distributions assumed are rather rough approximations, nevertheless at low dose-per-pulse little difference between them could be found (Boag et al., 1996). However, this might change for much higher dose-per-pulse values. Additionally, the effect of the collected charges on the electric field may come into play. While the ions are generally too slow to exhibit significant space charge effects, for the free electrons space charge effects were postulated to occur above a few cGy (Boag et al., 1996). To address this issue a solution of the equation system (2.7) could be sought that does not require those approximations.

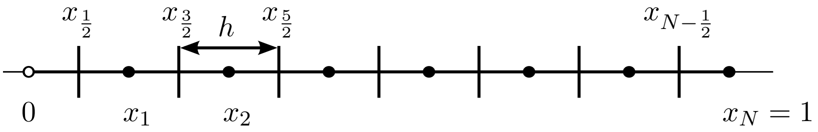

Figure 2.4: Discretization of the interval $[0, 1]$ using a uniform grid of N points, plus auxiliary boundary points.

2.4 Numerical Solution of Advection-Diffusion-Reaction Equations

Consisting of advection and reaction terms eq. (2.7) can be considered a special case of an advection-diffusion-reaction equation. Advection-diffusion-reaction equations are encountered in fields ranging from atmospheric modeling to cancer angiogenesis; they are, however, often not analytically solvable. Hence, a wide range of numerical approximation techniques have been developed to solve these systems.

Instead of solving the system for the entire space and time domain these methods approximate the solution at discrete points in time and space. Considering, as an example, the one dimensional advection equation in flux form

$$\frac{\partial u}{\partial t} = -\frac{\partial\left(v(x)u\right)}{\partial x} \tag{2.15}$$

with a velocity $v(x)$, a discretization is required for the spatial dimension x and the time.

The x-direction is discretized, for example, on the interval $[0, 1]$ by introducing a grid of N points $x_1, x_2, \ldots, x_N$, with $x_j = j/N$, which results in a cell size of $h = 1/N$ and cell boundaries lying at the auxiliary points $x_{j\pm\frac{1}{2}}$. The resulting grid is illustrated in Fig. 2.4. It is natural to mirror the mass conservation relation used in the original derivation of the advection equation (2.4) to write

$$u_j'(t) = \frac{1}{h}\left(v(x_{j-\frac{1}{2}})u_{j-\frac{1}{2}}(t) - v(x_{j+\frac{1}{2}})u_{j+\frac{1}{2}}(t)\right),$$

with the notation $u_j(t) = u(x_j, t)$ and the prime denoting a time derivative. This notation is used to emphasize the transition from a partial differential equation (PDE) to a system of N ordinary differential equations (ODEs).

The inversion of the mass conservation still leaves the values of $u_{j\pm\frac{1}{2}}$ at the auxiliary points to be approximated in terms of the neighboring points u_j. The exact form of this approximation defines the spatial discretization (Hundsdorfer and Verwer, 2003).

Two specific spatial discretizations will be discussed in the following. The assumption

$$u_{j+\frac{1}{2}}(t) = u_j(t),$$

for $v(x) > 0$ leads to the first order upwind scheme

$$u_j'(t) = \frac{1}{h}\left(v(x_{j-\frac{1}{2}})u_{j-1}(t) - v(x_{j+\frac{1}{2}})u_j(t)\right); \tag{2.16}$$

and the assumption

$$u_{j+\frac{1}{2}}(t) = \frac{1}{2}\left(u_j(t) + u_{j+1}(t)\right)$$

gives the second order central difference scheme

$$u_j'(t) = \frac{1}{2h}\left(v(x_{j-\frac{1}{2}})\left[u_j(t) + u_{j-1}(t)\right] - v(x_{j+\frac{1}{2}})\left[u_j(t) + u_{j+1}(t)\right]\right).$$

Subsequently, the system of N ODEs resulting from either of these discretizations, needs to be solved. Very generally such an ODE has the form

$$\frac{\mathrm{d}u}{\mathrm{d}t} = F(t, u(t)),$$

where u is written as a scalar function, but could equally be a vector resulting from spatial discretization.

Integrating both sides from $t = t_i$ to $t = t_i + \Delta t$ and approximating the right side by a single rectangle (like a Riemann sum with only one element) gives

$$u(t_i + \Delta t) - u(t_i) = \int_{t_i}^{t_i+\Delta t} F(t, u(t))\,\mathrm{d}t \approx \Delta t\, F(t_i, u(t_i)).$$

Given an initial solution $u(0)$ this allows the successive calculation of the solution at discrete time points $t_{i+1} = t_i + \Delta t$ by

$$u(t_{i+1}) = u(t_i) + \Delta t\, F(t_i, u(t_i)). \tag{2.17}$$

This specific approximation is known as the forward Euler method. Another possible approximation of the integral would be to calculate the rectangle using the upper limit of the integral, giving the backwards or implicit Euler method of

$$u(t_{i+1}) = u(t_i) + \Delta t\, F(t_{i+1}, u(t_{i+1})).$$

While these approximations (both space and time integration methods) are equal to the exact solutions in the limit of $h \to 0$ and $\Delta t \to 0$ a stricter convergence to the real solution is required for these methods to be useful numerical approximations. It needs to be shown that the errors introduced by these approximations can be bounded by bounding h and Δt, which can be broken down into two parts: Firstly, the local errors introduced by going from t_i to t_{i+1} need to be bounded (consistency) and, secondly, the result of bounded local errors must be a bounded global error (stability) (Hundsdorfer and Verwer, 2003). Establishing consistency is usually straightforward, for example, inserting the exact solution $u'(t_i)$ instead of $F(t_i, u(t_i))$ into eq. (2.17) and expanding around t_i one can calculate the local truncation error (Hundsdorfer and Verwer, 2003). Stability is more difficult to establish and usually requires that certain conditions are met, especially when considering the combination of a space and time discretization. For instance, using the forward Euler time integration method requires a step size limitation known as a Courant-Friedrichs-Levy condition (Courant et al., 1928). For the first order upwind spatial discretization (eq. (2.16)) with a constant velocity $v(x) = v$ this condition reads

$$\Delta t \leq \frac{h}{|v|}. \tag{2.18}$$

However, solving the pure advection problem with the central difference spatial discretization and the forward Euler time integration is unstable at any step size. The backwards Euler method on the other hand is computationally more costly, because it requires the inversion of F, but it has no step size limitation for either of the mentioned spatial discretizations.

In addition to the computational trade-offs of the time integration methods, the spatial discretization also present certain trade-offs. Figure 2.5 shows the result of applying both schemes introduced here to the solution of eq. (2.15) with a rectangular initial distribution and $v(x) = 1.0$. Discretization width was $h = 0.01$ for both schemes and a periodic boundary condition $u_0 = u_N$ was used. The resulting systems were integrated with an implicit Euler method and $\Delta t = 0.0005$ at $t = 4$. Since this is seen as a purely mathematical problem of solving the equation, no units are associated with the values. Compared to the exact

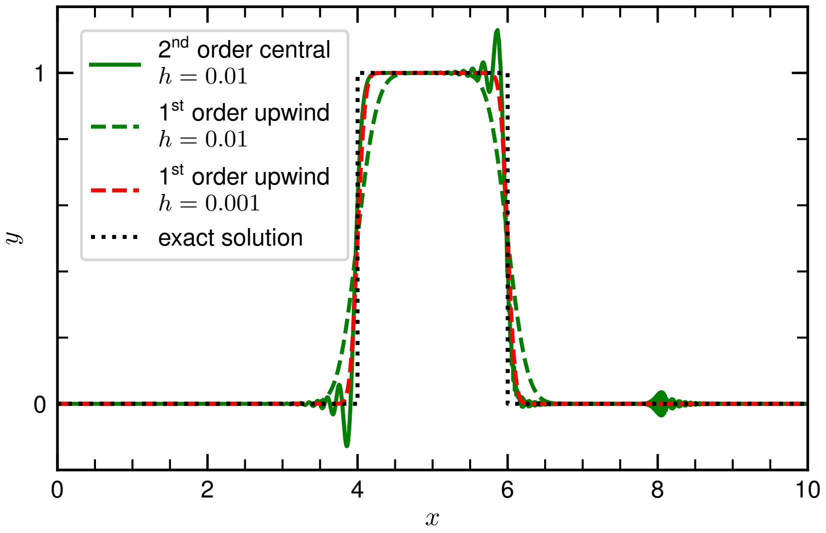

Figure 2.5: Compared are the exact solution to the results of the first order upwind and second order central discretization for the same cell size $h = 0.01$, both integrated with the backwards Euler method and $\Delta t = 0.0005$. The initial distribution was 1 for $0 < x < 2$, the velocity was $v(x) = 1.0$ and the solution calculated for the time $t = 4$. Additionally, a first order upwind calculation with a finer grid of $h = 0.001$ is shown.

solution, the first order upwind scheme smears the sharp gradients, while the second order difference scheme replicates those gradients more closely, but introduces oscillations, which in part lead to negative values, despite the original distribution being entirely non-negative. The first order upwind calculation with a finer grid replicates the gradients as well as the second order scheme, but at 10 times the computational cost.

The smearing introduced by the first order upwind discretization can be understood when considering the Taylor expansion of the scheme for a constant v

$$\frac{1}{h} v \left(u(x-h,t) - u(x,t) \right) = v \frac{\partial u(x,t)}{\partial x} + \frac{1}{2} v h \frac{\partial^2 u(x,t)}{\partial x^2} + \mathcal{O}(h^2).$$

The first order upwind scheme is a first order approximation to the pure advection equation, but also a second order approximation to an advection-diffusion equation. Therefore, it can be interpreted as the introducing of a numerical diffusion with a diffusion constant (Hundsdorfer and Verwer, 2003)

$$\delta_{numerical} = \frac{1}{2} v h. \tag{2.19}$$

Reducing h also reduces $\delta_{numerical}$, but often reducing h to levels where $\delta_{numerical}$ is negligible is not feasible due to computational limitations and the size of the investigated system. This is the primary reason other discretizations than the first order upwind scheme are often sought, however, it should be noted that the first order upwind scheme is the only discretization that ensures positivity for an advection problem on a uniform grid (Hundsdorfer and Verwer, 2003). Positivity, which ensures that a non-negative initial distribution leads to non-negative values at any time point, is particularly important if reaction terms are involved, that can quickly magnify spurious oscillations, making the entire solution unstable. In conclusion, the decision for a numerical approximation needs to weigh these different considerations, for example, how relevant steep gradients are versus the required smoothness of the solution and also the size of the investigated system versus the computational power available.

2.5 Dose Rate Meters for Radiation Protection Dosimetry

Dose rate meters are employed in radiation protection as fixed installations or as hand held devices to check or survey the safety of an area from a radiation protection standpoint. Compared to dosimetry for radiation therapy, this application requires a much higher sensitivity, as the dose rates of interest are much lower, typically in the µSv/h to mSv/h range compared to Sv/min in the direct field of a radiation therapy beam. In addition, the specifics of the investigated field are less well known in a radiation protection application, where typically an unknown mix of radiation qualities and energies is present. This uncertainty reduces the accuracy achievable with a typical radiation protection dose rate meter, which is reflected in the requirements made for these instruments. For instance, in order to be certified by the PTB a combined deviation of the response for a variation of the incident energy and direction of up to −29 % to +67 % is allowed (PTB, 2013). The low accuracy is justified, because the purpose of these instruments is a very general risk assessment that already condenses various factors into the single quantity of ambient dose equivalent.

Most generally speaking the problem of dose rate meters in a pulsed field can be seen as one of dynamic range. Commercial dose rate meters are designed to measure continuous fields somewhere in the range relevant for radiation protection from a few nSv/h to at most 1 Sv/h. The natural background is several tens of nSv/h setting the lower limit and a dose

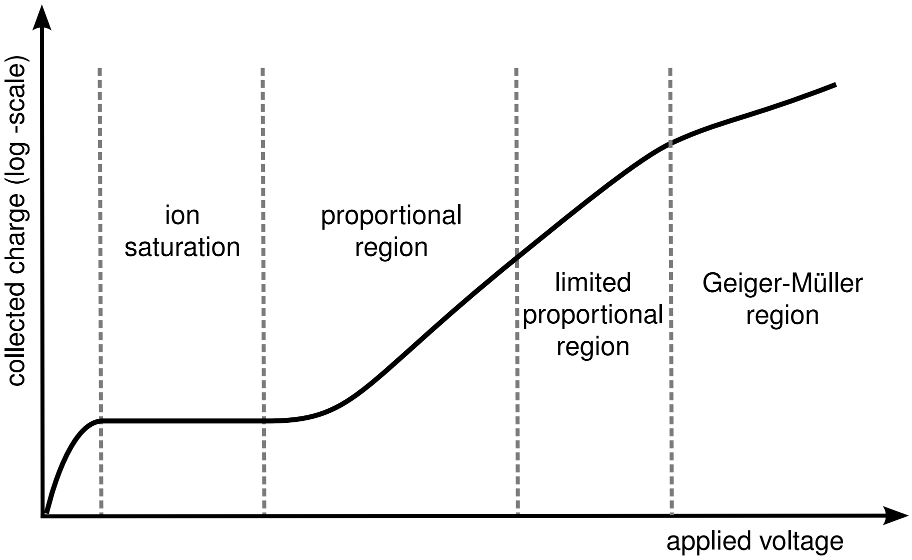

Figure 2.6: The regions of operation of a gas-filled ionization detector, based on (Knoll, 2000).

rate of 3 mSv/h would classify an area as an exclusion area. Still some instruments allow measurements above this dose rate, which may be of interest under some circumstances, for example, to monitor activation in an exclusion area or to asses the extent of the radiation exposure in a catastrophe. However, the momentary dose rate in a pulsed field is much higher than the average dose rate, for example, in the direct beam of a clinical LINAC the factor between peak and mean dose rate is 5000. Therefore, for an instrument, which is limited by the maximum dose rate it can measure, the measurable average dose rate will be orders of magnitude lower in a pulsed field, than in a continuous field, because the instrument's limits are quickly exceeded by the high peak dose rates during the radiation pulses.

2.5.1 Counting Tubes

Counting tubes are among the oldest radiation detectors. They are closely related to gas-filled ionization chambers, measuring the charge resulting from ionization of the gas. The typical shape is cylindrical with a central anode wire, similar to the thimble type ionization chamber in Fig. 2.3. As the voltage applied to such a chamber under irradiation is increased from 0 the collected charge increases (see Fig. 2.6) until it reaches the saturation plateau, where all the liberated charges, minus those lost in recombination, are collected. This is the operational region of the ionization chambers described in section 2.3.

If the voltage is increased further, the electrons acquire enough energy in between collisions to further ionize the gas, in particular in the region of high electric field close to the central anode, creating a charge avalanche due to gas amplification. The measured charge is proportional to the applied voltage and the amount of initially liberated charges. This is the region of operation of a proportional counter.

Some of the energy imparted on the molecules in collisions with the electrons, is released again in the form of energetic photons. Those photons in turn can cause ionizations in a distant region of the tube, sparking additional avalanches. If the applied voltage is sufficiently high each avalanche spawns at least one additional, distant avalanche, resulting in a discharge across the entire tube. In this Geiger-Müller region the amount of charge measured is independent of the initially liberated charge and every ionization event triggers a discharge across the entire tube, which stops when the build up of space charges due to the discharge leads to a drop in the electric field below the threshold needed for amplification (Knoll, 2000).

Proportional and Geiger-Müller counters operate in these respective voltage regions and detect ionization events by the discharges they trigger – they count those events. Counting of single ionization events allows the detection of much lower ionization rates than in the ionization chamber.

In the Geiger-Müller counter all information about the amount of charge liberated in the original event is lost, while the proportional counter retains this information. Nevertheless, the Geiger-Müller counter is a popular instrument, due to the simplicity of its construction and readout. The large amount of gas amplification allows a direct readout without further amplification, greatly simplifying the readout electronics.

In any system based on event counting one is faced with the problem of a dead time τ_{dead}, a time period after the detection of an event in which no further events can be registered. In a Geiger-Müller counter the detector itself is responsible for part of this dead time because, after the breakdown of the electric field due to the space charge buildup, a certain time is required to collect all the slow moving positive charges and restore an electric field capable of inducing another Geiger discharge (typically at least 50–100 µs (Knoll, 2000)). In a proportional counter the discharge is confined to a small region of the tube and recovery is much faster (few µs). However, in particular for the proportional counter, the dead time of the electronics used to measure the output pulses can also be the main dead time determinant (Knoll, 2000).

The dead time of the detection system leads to a difference in the measured count rate (m) and the true rate of ionization events in the detector (n). Assuming additional events during the dead time do not extend it (non paralyzable system) n can be calculated as

$$n = \frac{m}{1 - m\tau_{\mathrm{dead}}} \tag{2.20}$$

for a constant event rate and thus dose rate (Knoll, 2000).

In a pulsed field such a correction is more complicated, because it depends on the relative size of dead time, pulse duration and pulse period. As discussed for pulsed fields in general in section 2.2.1, long pulses (i.e., $t_{\mathrm{pulse}} >> \tau_{\mathrm{dead}}$) and rapid repetition rates (i.e, $1/f_{\mathrm{rep}} < \tau_{\mathrm{dead}}$) may be treated very similarly to the continuous case above. For short pulses and low repetition rates (i.e., $t_{\mathrm{pulse}} < \tau_{\mathrm{dead}} < T = 1/f_{\mathrm{rep}}$) at most one event is registered per radiation pulse and one can write (Knoll, 2000)

$$n = f_{\mathrm{rep}} \ln \left(\frac{f_{\mathrm{rep}}}{f_{\mathrm{rep}} - m} \right).$$

The problem becomes more complicated where intermediate cases are concerned and for commercial instruments. The exact dead time is often not available for a commercial instrument and often a dead time correction of the form of eq. (2.20) is already applied to the reported dose or count rate. The combined effect is that calculating a correct count rate from the one reported by the instrument requires intricate knowledge of the inner workings of the instrument.

2.5.2 Scintillation Detectors

Scintillators are one of the most popular radiation detectors, but not very common as dose rate meters. Ionizing radiation is converted to visible light in a scintillator, which is then detected by, for instance, a photomultiplier tube (PMT) or a semiconductor detector. Scintillators are well suited for spectroscopic applications, because the number of photons produced is proportional to the energy deposited in the scintillator; and they can be produced in various shapes and sizes to allow position sensitive detectors for different applications.

In a scintillator, part of the absorbed energy, which is in the form of ionized and excited molecules, is transfered to luminescence centers, where deexcitation occurs via the emission of visible photons. Two classes of scintillators exist, organic and inorganic ones. In organic scintillators the visible light is emitted by transitions in aromatic ring molecules. In an inorganic scintillator light emitting transitions occur in the band structure of a crystal. Typically a doping agent is introduced into the pure crystal to locally perturb the band structure and introduce suitable energy levels for deexitation under light emission.

Inorganic scintillators tend to have a higher light output, are denser and of materials of higher atomic number, making them more suitable for photon detection and spectroscopy (Knoll, 2000). Many of the materials are, however, expensive, brittle and hygroscopic. Organic scintillators can be dissolved in a suitable solvent to be used in liquid or a plastic form. As such they become highly malleable and the high amount of hydrogen makes them very suitable for neutron detection (Knoll, 2000). On the other hand, their low light output makes them unsuitable for the detection of low energy photons as well as most spectroscopic applications concerning photons.

While the fluorescence from a scintillator has a certain decay time, which limits the ability to distinguish two successive events, the deposited energy is still converted into visible light. Thus they could be ideal dose rate meters in a pulsed field. Nevertheless, this ability is limited by the light detector, the readout electronics and the specific implementation in a commercial system. For instance, a PMT has a limited dynamic range and will saturate in its output if the number of incident photons is too large. Furthermore, a scintillator may be used as a simple counting device with increased detection efficiency over a gas filled tube, in which case it would be limited in a similar way as the counting tube.

2.5.3 Current Regulatory Developments

Most currently, commercially available instruments are designed and tested solely for continuous fields, in part due to the lack of a normative framework and reference fields available (see section 2.2.1). In addition to the recent formulation of a standard for pulsed reference fields (ISO, 2015), the DIN IEC/TS 62743 (DIN, 2013) was developed, proposing requirements for counting dose meters operating in pulsed fields. With the aim to allow the measurement of single pulses by the dose rate meter, a set of requirements is defined as well as a maximum pulse dose rate ($\dot{H}_{\mathrm{pulse,max}}$) up to which an instrument can measure with an error of $\pm 20\,\%$. This dose rate can be estimated based on the calibration factor of the instrument G_count, which defines the dose associated with a single count event, as

$$\dot{H}_\mathrm{pulse,\,max} = \frac{0.25 \cdot G_\mathrm{count}}{\tau_\mathrm{dead}}. \tag{2.21}$$

Furthermore, amongst other requirements, the cycle time, that is the time used for averaging before displaying, should be < 30 s, known and fixable by the user and the count rate should be displayable. An instrument is suitable for a given field if $\dot{H}_\mathrm{pulse,max} > \dot{H}_\mathrm{pulse}$ and $\tau_\mathrm{dead} < t_\mathrm{pulse}$

The quoted requirements serve to outline some of the problems one might face when trying to use commercial instruments in a pulsed field. It is not always clear what corrections were applied to the displayed measurement value and raw values are rarely accessible. Furthermore, automatic changes in measurement range may leave the instrument in an unclear state and, while the primary detection method is often advertised by the manufacturer, the subsequent signal processing is often undisclosed.

While the DIN IEC/TS 62743 (DIN, 2013) is an excellent guideline to determine under which conditions a counting dose meter is suitable to measure single radiation pulses, it may be of little help when trying to find a suitable instrument to measure a given field. For instance, for a laser accelerated proton field with ps pulse duration, it is not possible to find a counting detector for which $\tau_\mathrm{dead} < t_\mathrm{pulse}$ and the standard is not applicable to detectors which do not derive their measurement from a primary counting signal, such as scintillators or ionization chambers. Additionally, for a survey dose rate meter it may be sufficient to accurately measure the repeated application of pulses instead of each individual pulse. Individual pulses would be much more critical in a personnel dosimeter determining individual exposure. This may relax some of the constraints set forth in DIN IEC/TS 62743 (DIN, 2013) and allow the usage of counting detectors for a wider parameter range.

3 Material and Methods

The two aspects of radiation protection dosimetry and clinical dosimetry for radiation therapy were investigated in separate but similar experiments using the Electron LINAC for beams with high Brilliance and low Emittance (ELBE) located at the Helmholtz-Zentrum Dresden-Rossendorf. In addition, a numerical calculation of the volume recombination in ionization chambers was performed.

In the experiments, measurements of different radiation protection dose rate meters were performed in pulsed fields of various settings to asses their feasibility as ambient dose monitors and analyze the effects of pulsed radiation on different operating principles.

In addition, the volume recombination was determined in clinical ionization chambers of both plane-parallel and a thimble geometry to test the calculation of both geometries. Furthermore, the typically used air vented setup was augmented by a measurement using pure N_2 as a filling-gas, which should allow to better explore the influence of the free electrons. Finally, two LICs were investigated, which could provide further insights into recombination effects at very high dose-per-pulse due to the much higher ionization densities encountered in these media.

3.1 Common Experimental Setup

A common experimental setup at ELBE shown in Fig. 3.1 was used for all the measurements. Minor modifications were required in some cases to accommodate the specifics of the investigated instrument and it had to be re-setup several times, because the experiments were performed in several beamtimes over a 3 year period. Nevertheless, the key characteristics of the experimental design remained unchanged. The electron beam of 20 MeV from ELBE exits the beamline vacuum through a 100 µm beryllium window and is used to irradiate an ionization chamber (IC), after which it is fully stopped in an aluminium Faraday cup, serving as the reference for the ionization chamber measurements. The collimator in front of the ionization chamber consists of 15 mm aluminium followed by 15 mm

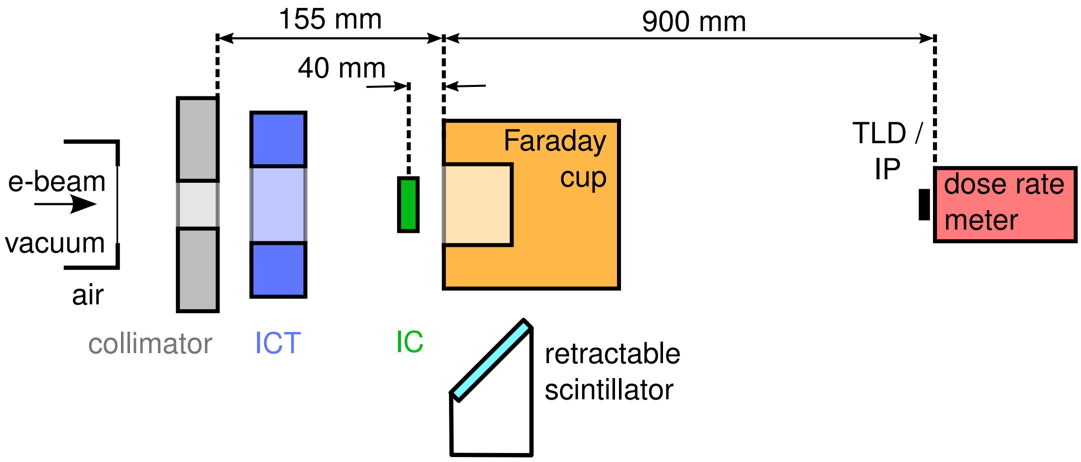

Figure 3.1: Experimental setup at ELBE showing the relative position of the key elements: ionization chamber (IC), Faraday cup and dose rate meters

lead with an opening of 17 mm in diameter. It limits the electron beam transversally, such that it is entirely captured by the Faraday cup and the integrated current transformer (ICT), an additional beam diagnostic directly behind the collimator.

The Bremsstrahlung created in the aluminium Faraday cup upon stopping the electron beam was used to irradiate the dose rate meters located behind the Faraday cup. This constellation allows using the same setup for investigating ionization chambers and dose rate meters, despite the large gap in the dose rates of interest.

In addition, the ionization chamber served as the reference for the measurement of the dose rate meters. In those experiments it functioned as a beam monitor, providing a more convenient reference measurement than the Faraday cup and, if necessary, a saturation correction could be performed using the Faraday cup measurements. The required cross calibration, linking ionization chamber measurement of the primary beam and dose rate of the Bremstrahlungs-field behind the Faraday cup, was performed using thermoluminescent dosimeters (TLDs) placed directly in front of the dose rate meters. To ensure sufficient homogeneity of the radiation field, another, 2-D measurement of the beam intensity at this position was performed using an image plate (IP), a detector based on optically stimulated luminescence (OSL). Both TLD and OSL are retrospective detectors, whose response has been shown to be independent of the applied dose rate (Karsch et al., 2012).

3.1.1 Radiation Source ELBE

The superconducting linear accelerator ELBE was used in these experiments to deliver an electron beam of 20 MeV energy. As a LINAC it exhibits the typical micro-pulse structure, but, due to its superconducting construction, does not require macro-pulsing. The micro-pulses or bunches have a temporal width of 5 ps and a repetition rate of 13 MHz, allowing the consideration of this time structure as quasi continuous in the context of the instruments investigated here. Despite not needing it, a (macro-)pulse structure may still be superimposed on this quasi continuous field and it can be controlled over a wide range. It is this macro-pulse structure that will be considered as the time structure of the radiation field.

The number of bunches included in a pulse and thus the pulse duration can be controlled from a single bunch of 5 ps to several seconds pulse duration, while the pulse period can be varied from 100 µs to applying only a single pulse. In addition, the intensity of each bunch can be controlled by setting the gate voltage of the electron gun. While this allows the control of the bunch charge and thus the dose-per-pulse, the relationship is non-linear and depends on the specific settings of the beamline, which varied between beamtimes. Therefore, the setting of a specific desired bunch charge is usually an experimental and iterative process.

In general, two parameters of the radiation field were varied: the dose-per-pulse and the pulse duration. Varying the dose-per-pulse for a fixed pulse duration and period is straightforward by varying the gate voltage. While the exact dose-per-pulse obtained may not be known in advance, it is still the only quantity altered and it can be determined exactly retrospectively.

Varying the pulse duration is more complicated. The starting point for such a variation was a short pulse duration with a few or a single bunch in each pulse. Adding more bunches elongates the pulse, but also increases the dose-per-pulse as the constant bunch charge is equivalent to a constant pulse dose rate. In terms of a constant pulse dose rate this can also be understood as applying the same dose rate for a longer time, which increases the integral dose. In order to maintain a constant dose-per-pulse the gate voltage was lowered until the dose-per-pulse of the elongated pulse matched that of the original, using the Faraday cup measurements to determine dose-per-pulse. However, due to-pulse-to pulse fluctuations small variations in the dose-per-pulse remain, requiring a correction of the final data.

The X-ray spectrum used to irradiate the dose rate meters was rather hard, due to the length of the Faraday cup of 130 mm serving as the bremsstrahlungs-target. A Monte Carlo simulation of the spectrum yielded an average photon energy of 4.8 MeV and a median of 3.4 MeV (Rohling, 2015). The time structure of this X-ray field emitted in forward direction of the relativistic electron beam should correspond to that of the primary electron beam, as contributions which smear the time structure such as path length differences from multiple scattering paths or activation should be marginal.

3.1.2 Beam Monitoring Equipment

The ICT, the Faraday cup and the retractable scintillator served as control instruments to verify proper characteristics of the electron beam.

The ICT is a capacitively coupled toroidal coil that outputs a current pulse proportional to the charge passing through it. The commercial unit employed here, was ICT-CF4.5"/34.9-070-05:1-UHV from Bergoz Instrumentation, Saint-Genis-Pouilly, France. Its bandwidth is sufficiently high to resolve the intensity of each individual bunch of the electron beam, allowing verification of a constant intensity of the bunches throughout each pulse.

The Faraday cup stops and collects the entire charge of the electron beam, facilitating a dose rate independent, yet destructive, measurement of the beam intensity. The Faraday cup used here was a custom construction, connected to a custom charge sensitive amplifier. The voltage signal from this amplifier was read with a Digital Phosphor Oscilloscope (DPO 7254 from Tektronix, Beaverton, USA). The linearity of the amplifier was determined in a pre-experiment by connecting a capacitor in place of the Faraday cup and charging that capacitor with a well defined voltage. In addition, this pre-experiment determined the relative amplification of the two gain settings of the amplifier. A detailed description of the evaluation of the Faraday cup signals is given in the Appendix A.

The retractable scintillator was placed in the beam instead of the Faraday cup to verify the position of the electron beam. Both Faraday cup and scintillator were mounted on separate linear actuators, such that choosing which one to place in the beam could be controlled remotely. The scintillator was positioned with a 45° angle to the beam and imaged by a CCD camera 90° to the beam. The verification was performed periodically throughout the beamtimes, but only with one beam setting of fixed pulse-duration, dose-per-pulse and repetition rate to achieve sufficiently bright, but not saturated, images.

Table 3.1: Properties of the investigated dose rate meters according to their data sheets (Berthold Technologies GmbH & Co. KG, 2007; Automation und Messtechnik GmbH, 2011; Rotem Industries LTD., 2014).

probe + readout	dose rate range	type	diameter	counting
RamION (integrated unit)	min: 1 µSv/h max: 500 mSv/h	ionization chamber	90 mm	no
LB 1236-H10 +LB 1230 UMo	min: 0.1 µSv/h max: 10 mSv/h	proportional counter	50 mm	yes
6150AD-b +6150AD	min: 0.1 µSv/h max: 0.1 mSv/h	organic scintillator	76 mm	no

3.2 Dose Rate Meter Measurements

For the investigation three commercial dose rate meters based on different operating principles were chosen. The RamION is an air filled ionization chamber from Rotem Industries, Rotem Industries Park, Israel, the LB 1236-H10 is a proportional counter which is connected to the LB 1230 UMo readout unit, both from Berthold Technologies, Bad Wildbad, Germany and the 6150AD-b is a scintillation counter combined with the 6150AD readout unit, both from Automess - Automation and Messtechnik GmbH, Ladenburg, Germany. A summary of the instrument properties is shown in table 3.1. All three were factory calibrated to ambient dose equivalent $H^{*}(10)$ using ^{137}Cs irradiation.

All the dose rate meters under consideration had a cylindrical shape and were positioned with that cylinder axis centered on the beam axis. The front face of the cylinder was positioned at a distance of 900 mm behind the Faraday cup, to achieve a comparable positioning for all the instruments, despite their otherwise variable shape.

The readout units of the LB 1236-H10 and the 6150AD-b could be conveniently positioned in the control room, while the sensor was irradiated in the bunker. However, the RamION is a single, integrated unit and could only be readout via camera.

3.2.1 Measurement Series and Procedure

Before the measurement a reading of the radiation background in the experimental bunker was taken with each instrument to be subtracted from the subsequent measurements. In each beam setting the instrument was irradiated for 60 s prior to a reading to allow for an adjustment of the internal averaging. Then, the reading was taken by observing the display for a few seconds and recording a representative value for this duration. The 6150AD-b allowed to formalize this process by internally averaging the dose rate over a 60 s period.

All instruments were investigated for the dependence of their response on the dose-per-pulse and the pulse duration. The dose-per-pulse was varied with a pulse duration of 5 ps employing a single electron bunch, applied at a repetition rate of 5 Hz for the RamION and the 6150AD-b. In the case of the LB 1236-H10 a higher repetition rate of 25 Hz was necessary to obtain a signal sufficiently above the background. At the high end of the dose-per-pulse variation the dose is limited by the maximum bunch charge. Therefore, the dose-per-pulse series using a single bunch per pulse was expanded in the case of the RamION by also applying pulses with a maximum bunch charge containing 10 and 50 bunches, corresponding to a pulse duration of 0.693 µs and 3.773 µs respectively.

The pulse duration was varied using that same repetition rate and a constant dose-per-pulse that was different for each instrument. Due to the mentioned, unavoidable dose-per-pulse variations in this series these results were normalized to the maximum dose-per-pulse ($D_\mathrm{pulse}^\mathrm{max}$) as measured by the ionization chamber. To this end each measurement point was multiplied with $D_\mathrm{pulse}^\mathrm{max}/D_\mathrm{pulse}$, where D_pulse is the dose-per-pulse obtained for that pulse duration.

3.2.2 Reference Measurements

The dose rate at the position of the dose rate meters was determined with a reference measurement using TLD-100H chips from Thermo Fisher Scientific, Waltham, USA. Prior to irradiation the TLDs were annealed for 30 min and read after irradiation with a commercial reader (Harshaw 3500, Thermo Fisher Scientific, Waltham, USA). For the readout a heat curve with a 10 s pre-heat at 135 °C followed by a readout lasting 23 s at 240 °C was employed as recommended by the manufacturer.

A calibration of the TLD reading in terms of dose to water was created for each TLD by irradiation in a 200 kV X-ray tube. Using a calibrated Farmer type ionization chamber (Type 30010, PTW, Freiburg Germany) the dose to water in this irradiation was determined and subsequently a linear relationship between TLD readout and dose was established. 5 dose points for each chip at 0.9 mGy, 3 mGy, 5 mGy, 50 mGy and 500 mGy were used in this calibration.

Table 3.2: Dimensions of the sensitive volume and the sensitive media of the ionization chambers used. Listed are the electrode distance (d) and the electrode's radius (r) for the plane-parallel geometries and the inner and outer electrode radius (r_1 and r_2 respectively) for the thimble type chamber as well as the sensitive volume (V_sens) for all chambers.

chamber	d (mm)	r (mm)	V_sens (mm^3)	sensitive media
adv. Markus	1.0	2.5	20	air, N_2
LIC	0.35	1.25	1.7	isooctane, TMS
	r_1 (mm)	r_2 (mm)		
PinPoint	0.575	2.75	125	air

Due to the time consuming nature of irradiating and reading the TLDs it was unfeasible to use a TLD for every measurement point of the dose rate meter investigation. Instead a calibration of an Advanced Markus ionization chamber, located in front of the Faraday cup, to the dose at the dose rate meter position was established. To this end TLDs were irradiated with a pulsed beam consisting of pulses of 1.463 µs pulse duration with a repetition rate of 5 Hz. Different dose points were achieved by varying the duration of this irradiation. Furthermore, an irradiation with a quasi continuous beam ($f_\mathrm{rep} = 13\,\mathrm{MHz}$) was performed to exclude any effects of the irradiation time structure.

3.3 Ionization Chamber Measurements

In order to maximize the available dose-per-pulse small ionization chambers were chosen for the investigation: A plane-parallel Advanced Markus chamber and a thimble-type PinPoint chamber. In addition to performing measurements with these air-filled chambers, experiments were performed filling the Advanced Markus chamber with N_2 and using two plane-parallel liquid ionization chambers (LICs).

All chambers were manufactured by PTW, Freiburg, Germany and the collected charge was measured for all chambers using a Unidos webline electrometer also from PTW. The Advanced Markus chamber was PTW type 34035, the PinPoint chamber type 31010 and the two LICs were both of type 31018, one filled with the standard 2,2,4-Trimethylpentane (isooctane) while the other was a custom product filled with tetramethylsilane (TMS). Both LICs were provided as a generous loan by Heikki Tölli from Umeå University.

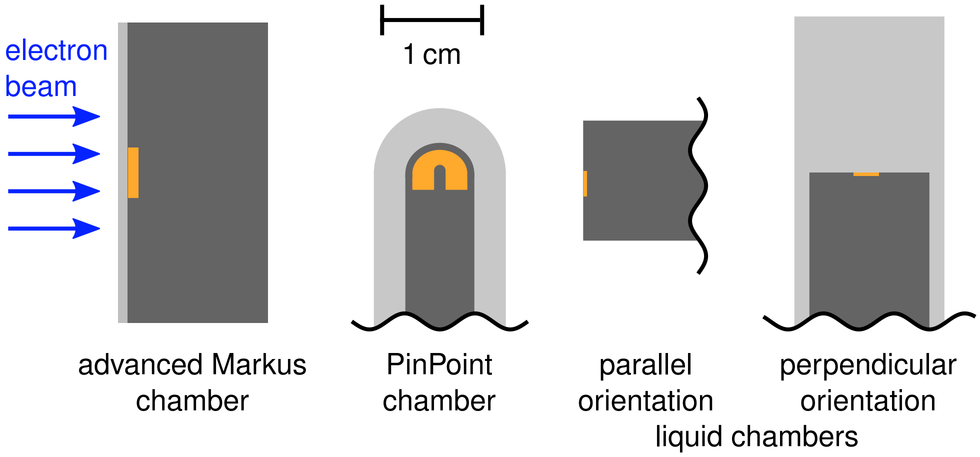

Figure 3.2: Relative size and orientation of the ionization chambers used in the experiment. Orange is the sensitive volume, dark gray the chamber body and light gray are buildup caps.

The geometric properties of the different ionization chambers used are summarized in table 3.2. The orientation of the different chambers in the irradiation setup is shown in Fig. 3.2. The Advanced Markus chamber was positioned with its cylinder axis centered on the beam axis, parallel to the beam, while the PinPoint chamber was positioned with its cylinder axis perpendicular to the beam and its reference point on the beam axis. To avoid effects resulting from the inhomogeneity the chamber walls present, the PinPoint chamber was fitted with a buildup cap with a wall thickness of 3 mm made of poly(methyl methacrylate) (PMMA).

Due to the larger size of the sensitive volume of the PinPoint chamber and the increased difficulty of ascertaining its center, a scatterer of 150 µm aluminium was placed in front of the collimator for the PinPoint measurements, homogenizing the lateral beam profile over a larger area.

The LICs were initially positioned analogously to the Advanced Markus chamber with their axis parallel to the beam. However, their housing and the cable extent in the direction of the electrode separation, necessitating a large distance between the sensitive volume and the Faraday cup reference and leaving the readout cable in the radiation field. In order to avoid effects due to this geometry, in a later experiment the LICs were also fitted with a build up cap and positioned analogously to the PinPoint chamber, perpendicular to the beam. Furthermore, in this final experiment the collimator was removed and a 4 mm thick cerium-doped yttrium aluminium garnet (YAG) crystal placed 20 mm in front of the center of the LIC. This scintillating material was imaged using a mirror and a CCD-camera, providing an online monitor of the beam position. In addition, it served as a scatterer broadening the beam profile.

Performing measurements using N_2 instead of air as a filling-gas with the Advanced Markus chamber also required some changes to the setup, because the chamber is not sealed but vented to the surrounding atmosphere. Therefore, the chamber was enclosed in its entirety in a vacuum chamber fitted with 1 mm aluminium entrance and exit windows. The Faraday cup was placed behind this vacuum chamber, which had a total thickness in beam direction of 55 mm, and the collimator was relocated to be directly in front of the vacuum chamber's entrance window. The vacuum chamber was twice evacuated using a pre-pump to a pressure of about 0.2 mbar and subsequently filled with pure N_2. An overpressure valve released excess N_2 establishing a total pressure of 1310 mbar inside the chamber. The gas inside the chamber was cycled through a Rapidox 2100 sensor (Cambridge Sensotec Limited, St Ives, Cambridgeshire, UK) to monitor the relative O_2 pressure in the vacuum chamber, which was below 1 mbar directly after the gas exchange.

For all the ionization chamber measurements radiochromic Gafchromic EBT 2 films (Ashland Specialty Ingredients, Wilmington, USA) were irradiated directly in front of the ionization chamber periodically throughout the experiments to verify the lateral beam profile.

3.3.1 Measurement Series and Procedure

For each measurement series with an ionization chamber a fixed collection voltage was set and either dose-per-pulse or pulse duration was varied, keeping the other quantity constant.

The dose-per-pulse was varied at a constant pulse duration of 3.773 µs. This value includes a sufficient number of bunches (50), such that the highest usable dose-per-pulse in the experiment is not dictated by maximum bunch charge deliverable by the accelerator (corresponding to $\sim$60 mGy), but rather by the measurement limit of the amplifier of the Faraday cup. In addition, it is close to a typical LINAC pulse duration and therefore allows a good comparison to existing data. The Advanced Markus chamber in air was irradiated using U_c values of 50 V, 100 V, 300 V and 400 V and the PinPoint chamber using values of 100 V and 300 V. The measurements using N_2 were performed at a single U_c value of 100 V and those of the LIC at a value of $U_\mathrm{c} = 800$ V.

The dose-per-pulse used for the variation of the pulse duration was not identical for all those measurement series due to the outlined difficulties in obtaining a predefined dose from the accelerator. The maximum bunch charge available was used to create the most intense pulse possible, while at the same time employing the shortest possible pulse duration of 5 ps. This determined the dose-per-pulse for most pulse duration series. In order to increase the dose-per-pulse in these series, some were also started at longer pulse duration, allowing multiple bunches per pulse, thusly increasing the maximum dose-per-pulse available. The exact liberated charge values obtained in each series are reported in the respective results.

The Faraday cup's amplifier had an auto reset function which limited the maximum pulse duration to 308 µs corresponding to 4000 bunches in the pulse. Only in the final measurements of the LIC an updated version of this electronics was available, enabling measurements with a pulse duration up to 9856 ms corresponding to 128 000 bunches in the pulse.

At each measurement point (i.e., combination of dose-per-pulse, pulse duration and chamber voltage) 15–20 measurements using a single radiation pulse were taken. For every such single pulse irradiation a k_s was calculated. In the dose-per-pulse variation those k_s were simply averaged to obtain a $\left.\overline{k_\mathrm{s}}\right|_{D_\mathrm{pulse},\, t_\mathrm{pulse},\, U_\mathrm{c}}$ at that measurement point.

In the pulse duration variation such an average would have resulted in a slightly different D_pulse for each point of the series due to the mentioned fluctuations in the accelerator output. Therefore, for each pulse duration a linear fit of the relation $k_\mathrm{s}(D_\mathrm{pulse})$ was performed, using the 15–20 measured k_s values. The resulting function was evaluated at the same $(D_\mathrm{pulse})_\mathrm{nominal}$ for an entire series of different pulse durations. The value of $(D_\mathrm{pulse})_\mathrm{nominal}$ was determined by taking the average of all the dose-per-pulse values obtained in the respective series. The effect of this correction was small with the largest correction to k_s resulting from this procedure when compared to simply averaging the values being 1.8 %.

3.3.2 Experimental Determination of Volume Recombination

The measurement yields data pairs of ionization chamber and Faraday cup measurements $\{M_\mathrm{IC}, M_\mathrm{FC}\}$, which were used to calculate a k_s correcting for volume recombination. The liberated charge in the ionization chamber is given in this measurement by $Q_0 = c_\mathrm{calib} \cdot M_\mathrm{FC}/c_\mathrm{amp}$, the product of the Faraday cup measurement divided by the relative gain of the charge sensitive amplifier (c_amp) and a calibration factor (c_calib). The collected charge in the chamber needs to account for a background M_IC^0 and is given by $Q_\mathrm{c} = M_\mathrm{IC} - M_\mathrm{IC}^0$.

Combining these gives

$$k_\mathrm{s} = \frac{Q_0}{Q_c} = \frac{c_\mathrm{calib} \cdot M_\mathrm{FC}/c_\mathrm{amp}}{M_\mathrm{IC} - M_\mathrm{IC}^0}. \tag{3.1}$$

Two amplifier settings were used throughout the experiments. The higher gain setting ($\mathrm{S}_2 = 1$), used to measure lower dose-per-pulse, was assigned a relative gain of exactly $c_\mathrm{amp}(\mathrm{S}_2 = 1) = 1$. The value for the lower gain setting ($\mathrm{S}_2 = 0$), used to measure higher dose-per-pulse, was determined in a pre-experiment. In this pre-experiment the amplifier of the Faraday cup was connected to a known capacitance, which was charged with a defined voltage. The resultant signal from the amplifier was recorded in the same way as the Faraday cup signal was in the main experiments. This allowed to verify the linearity between voltage output of the amplifier and the charge up to an output voltage of 1.2 V. In addition, by comparing the slope of the linear relation for both gain settings, the relative gain of the two amplifier settings was determined as $c_\mathrm{amp}(\mathrm{S}_2 = 0) = 0.072 \pm 0.009$.

Considering that eq. (2.13) is generally deemed a good approximation of k_s for low dose-per-pulse values, c_calib can be determined from a linear extrapolation of the measurement at low dose-per-pulse. To this end the quotient $\frac{M_\mathrm{FC}/c_\mathrm{amp}}{M_\mathrm{IC} - M_\mathrm{IC}^0}$ is plotted against the quantity $M_\mathrm{FC}/c_\mathrm{amp}$. Inserting eq. (3.1) as well as the measurement definition of Q_0 into eq. (2.13) and dividing by c_calib yields

$$\frac{M_\mathrm{FC}/c_\mathrm{amp}}{M_\mathrm{IC} - M_\mathrm{IC}^0} = \frac{1}{c_\mathrm{calib}} + \frac{a(1-p)}{2}\left(M_\mathrm{FC}/c_\mathrm{amp}\right)$$

showing that the axis intercept of this plot is the inverse of the desired calibration factor.

The need for a background correction of the ionization chamber measurement (using $Q_\mathrm{c} = M_\mathrm{IC} - M_\mathrm{IC}^0$) results from the long integration window of 10 s of the electrometer compared to the Faraday cup measurement, which only considers the actual radiation pulse of $t_\mathrm{pulse} <$ 400 µs. Even when no pulses are triggered in the accelerator, some radiation is still emitted, due to the electron gun's dark current and field emission in the acceleration cavities, causing a background ionization rate in the ionization chamber.

To ensure that the data included in the extrapolation was sufficiently described by the linear extrapolation the r^2 of the fit was considered. Starting with the three lowest dose-per-pulse data points, additional points were added if they did not lower the r^2. For the gas-filled chambers this resulted in $r^2 >$ 0.99 and included points with a k_s of at most 1.1. In the case of the LICs it was $r^2 >$ 0.95 and k_s at most 1.5.

Using this calibration, any dose independent contributions to k_s, such as initial recombination, are folded into this calibration factor. Therefore, the measured k_s only includes contributions from volume recombination.

3.4 Numerical Calculation of Volume Recombination

3.4.1 Plane-parallel Chamber Geometry

The k_s for volume recombination was calculated by numerically solving the equation system (2.7). The solver was implemented in C++ using a first order upwind discretization in space (eq. (2.16)) and a forward Euler method for time integration (eq. (2.17)). The mathematical aspects of this numerical solver are outlined here, while a description of the concrete implementation is given in the Appendix B. The full source code of the developed implementation is archived online at Gotz (2017) allowing for convenient download and compilation directly from the given online source.

For the numerical solution the sensitive volume in direction perpendicular to the electrodes was segmented into N bins of size h plus two bins outside the sensitive volume (see Fig. 3.3). This results in the major grid points $x_0, \ldots, x_{N+1}$ and auxiliary grid points at the cell boundaries $x_{-\frac{1}{2}}, \ldots, x_{N+\frac{3}{2}}$ with the auxiliary points $x_{\frac{1}{2}}$ and $x_{N+\frac{1}{2}}$ lying directly in front of the electrodes delimiting the sensitive volume. The concentrations are defined at the major grid points and can be viewed as averages over the cell, while the electric field strength, and consequently the drift velocities, are calculated at the cell boundaries. This results in the full recursive definition of the positive ion concentration (c_+), for example, as

$$\begin{aligned} c_+(x_i, t_m) = {} & \Delta t\, R(t_{m-1}) - \Delta t\, \alpha\, c_-(x_i, t_{m-1})\, c_+(x_i, t_{m-1}) + \\ & \frac{\Delta t}{h} \left(\mu_+ E(x_{i-\frac{1}{2}})\, c_+(x_{i-1}, t_{m-1}) - \mu_+ E(x_{i+\frac{1}{2}})\, c_+(x_i, t_{m-1}) \right). \end{aligned}$$

The calculation steps forward through time starting at a point $t = 0$ when all charge carrier concentrations are zero with a step width $\Delta t = t_m - t_{m-1}$. Irradiation creates charge carriers homogeneously throughout the sensitive volume and in each time step their movement and reactions are calculated. Charges that arrive in either of the bins located outside the sensitive volume (x_0 and x_{N+1}) are considered as collected at the electrode and removed from the calculation.

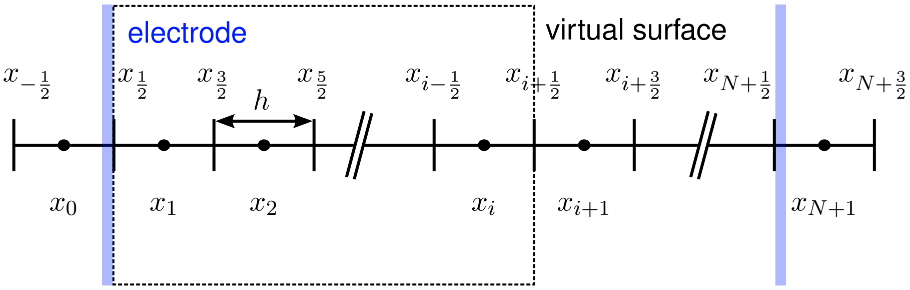

Figure 3.3: Illustration of the discretization of a plane-parallel chamber and, as an example, the virtual surface used to calculate the electric field at point $x_{i+\frac{1}{2}}$ is shown.

At the end of each time step, after considering movement, reactions and collection, this newly determined charge density is used to calculate the electric field and thus the charge carrier velocities for the next time step. The calculation is based on Gauss's law

$$\frac{Q}{\epsilon_0} = \oint_S \vec{E} \cdot \mathrm{d}\vec{A}$$

relating the total charge Q enclosed by a surface S to the surface integral of the electric field. The electric field at point $x_{i+\frac{1}{2}}$ is calculated considering a cylinder ranging from $x_{\frac{1}{2}}$ to $x_{i+\frac{1}{2}}$ in x-direction and in the other dimensions encompassing the entire sensitive volume (shown as the virtual surface in Fig. 3.3). Considering only the x-component of the electric field is non-zero, only the surfaces perpendicular to the electrodes contribute to the integral allowing Gauss's law to be written as

$$\frac{hA}{\epsilon_0} \sum_{j=1}^{i} \rho(x_j) = A \left(E(x_{i-\frac{1}{2}}) - E(x_{\frac{1}{2}}) \right) ,$$

with A being the area of the top and bottom of the virtual cylinder considered, that is the area of the collection electrode.

The value of the electric field directly in front of the electrode ($E(x_{\frac{1}{2}})$) is essentially a normalization constant, a common offset to the electric field throughout the considered volume. It can be determined from the condition that a constant voltage is applied and thus the potential difference between the electrodes must be kept constant

$$U_\mathrm{c} = h \left[\sum_{i=1}^{N-1} E(x_{i+\frac{1}{2}}) + \frac{1}{2} \left(E(x_{\frac{1}{2}}) + E(x_{N+\frac{1}{2}}) \right) \right] .$$

The next time step is dynamically calculated at the end of each step as $\Delta t = \frac{1}{2}\frac{h}{max(|v(x)|)}$ to fulfill the the Courant-Friedrichs-Levy condition (eq. (2.18)). It is based on the previously calculated values for the electric field, which determines the velocity of the different charge carriers ($v_i(x) = \mu_i(E(x))E(x)$). Once the total amount of charge left is less than 10^{-6} of the amount created during irradiation the collection is considered complete and the time stepping is aborted.

While this combination of methods is possibly the most primitive numerical approach to solve such a system, it has some distinct advantages over more elaborate schemes. First and foremost it ensures positivity of the solution. Thus, a negative concentration of any of the charge carriers is avoided and charge conservation is assured. Furthermore, the explicit time integration allows for an easy consideration of the effects of the charges on the electric field, which can be simply recalculated at the end of each time step and the new values used in the next step. In an implicit method the dependence $E(\rho(c_+, c_-, c_e))$, which is itself a differential equation, would greatly increase the complexity of the matrix inversion required in each time step.

The downside of this simple approach is the low numerical order, namely the error due to using a finite number of points to approximate the whole function decreases only linearly with the chosen grid size. Higher order methods would provide the same accuracy at larger grid sizes and thus lower computational cost. However, the systems under consideration are rather small; for instance, the electrode distance in an Advanced Markus chamber is only 1 mm, allowing for a very small grid size without the need for exorbitant computational power.

Similarly the problem of introducing numerical diffusion when using the first order upwind discretization (eq. (2.19)) can be addressed by requiring that the numerical diffusion should not exceed the physical diffusion in the real system. The diffusion constant of a charged particle with charge q and mobility μ at temperature T may be expressed using the Einstein-Smoluchowski relation (Einstein, 1905; von Smoluchowski, 1906) as

$$\delta_{physical} = \frac{\mu k_{\mathrm{B}} T}{q}$$

Using that the numerical diffusion is also related to the particle mobility (eq. (2.19) in conjunction with eq.(2.6)), a requirement for the grid size h is derived based on the inequality

$\delta_{\text{numerical}} < \delta_{\text{physical}}$, which results in

$$h < \frac{2k_{\mathrm{B}}T}{qE}.$$

Assuming singly charged particles (i.e., $q = e$, with e being the elementary charge), $T = 293$ K and an $E = 4000$ V/cm this establishes an upper limit as $h < 126$ nm. In the calculations for the Advanced Markus chamber this limit is observed by using a bin size of $h = 100$ nm, corresponding to 10 000 bins.

3.4.2 Adaption to Thimble Chamber Geometry

The derivation of the equation system 2.7 and its numerical solution outlined above were performed assuming a homogeneously irradiated plane-parallel chamber. The reaction and creation terms are readily transferred to any homogeneously irradiated chamber. However, in order to extend this approach to a thimble type chamber, like the investigated PinPoint chamber, the advection term needs some additional consideration. The geometry of a thimble type chamber is a combination of a half sphere and a cylinder (see Fig. 2.3). In order to simplify this problem a pure cylindrical geometry is assumed for this calculation, which shall have the same inner and outer electrode radii and the same sensitive volume as the PinPoint chamber (see table 3.2), resulting in a length of the model cylinder of $l = 5.5$ mm.

The obvious choice for a coordinate system is then a cylindrical coordinate system, with the three basis vectors $\hat{e}_r, \hat{e}_\phi, \hat{e}_z$ and corresponding coordinates r, ϕ, z. The advection equation from (2.5) is easily generalized to three dimensions using those coordinates as

$$\begin{aligned}\frac{\partial c(\vec{r},t)}{\partial t} &= -\nabla \cdot \left(\vec{v}(\vec{r},t)\, c(\vec{r},t)\right)\\ &= -\frac{1}{r}\frac{\partial(\vec{v}(\vec{r},t)\cdot\hat{e}_r\, c(\vec{r},t)\, r)}{\partial r} - \frac{\partial(\vec{v}(\vec{r},t)\cdot\hat{e}_\phi\, c(\vec{r},t))}{\partial \phi} - \frac{\partial(\vec{v}(\vec{r},t)\cdot\hat{e}_z\, c(\vec{r},t))}{\partial z}.\end{aligned}$$

The advection field ($\vec{v}$) is a direct result of the electric field inside the ionization chamber, which has only a radial component ($\vec{E} = E(r)\hat{e}_r$). This allows the simplification of the advection equation to one dimension in direction of $\hat{e}_r$

$$\frac{\partial c(r,t)}{\partial t} = \frac{1}{r}\frac{\partial(\mu\, E(r,t)\, c(r,t)\, r)}{\partial r},$$

which can be discretized analogously to the advection term in the plane-parallel geometry with major grid points r_i and minor grid points $r_{i+\frac{1}{2}}$, spaced at a distance h. This yields as the fully discretized equation for positive ions, for example:

$$\begin{aligned} c_+(r_i,t_n) = {} & \Delta t\, R(t_n) - \Delta t\, \alpha\, c_-(r_i,t_{n+1})\, c_+(r_i,t_{n+1}) + \\ & \frac{\Delta t}{h\, r_i}\left(r_{i-\frac{1}{2}}\mu_+ E(r_{i-\frac{1}{2}})\, c_+(r_{i-1},t_{n-1}) - r_{i+\frac{1}{2}}\mu_+ E(r_{i+\frac{1}{2}})\, c_+(r_i,t_{n-1}) \right). \end{aligned}$$

In addition to modifying the advection terms, calculating the electric field from the charge density needs some modification to be used in the cylinder geometry. The principle of using Gauss's law remains unchanged, but now cylinders with their central axis along the central electrode of the cylinder chamber are considered. The electric field is perpendicular to the mantle of these cylinders. Assuming that the central electrode of this ionization chamber holds a charge Q_{central} due to the applied voltage and considering that each bin has the volume $V_i = 2\pi r_i h l$ (difference of cylinders of radius $r_i + h/2$ and $r_i - h/2$), Gauss's law can be written as

$$\frac{2\pi h l}{\epsilon_0}\left(\sum_{j=1}^{i} r_j \rho(r_j)\right) + \frac{Q_{\mathrm{central}}}{\epsilon_0} = \pi r_{i+\frac{1}{2}}^2 l E(r_{i+\frac{1}{2}}).$$

Solving this equation for $E(r_{i-\frac{1}{2}})$ gives the electric field in dependence of the ρ_i. The charge on the central electrode is the normalization constant to be calculated from the condition that the applied voltage is constant, taking the place of the electric field directly in front of the electrode in the plane-parallel chamber.

3.4.3 Input Parameters

Beyond solving the equation system (2.7) the calculation of k_{s} from that solution also requires the knowledge of the various interaction parameters therein. Particularly for a numerical procedure a solution cannot be obtained without assigning explicit values to the parameters. Namely, the mobility of the three considered charge carriers (positive ions, negative ions and electrons), the attachment coefficient of the electrons (γ) and the recombination coefficient of positive and negative ions (α) are required.

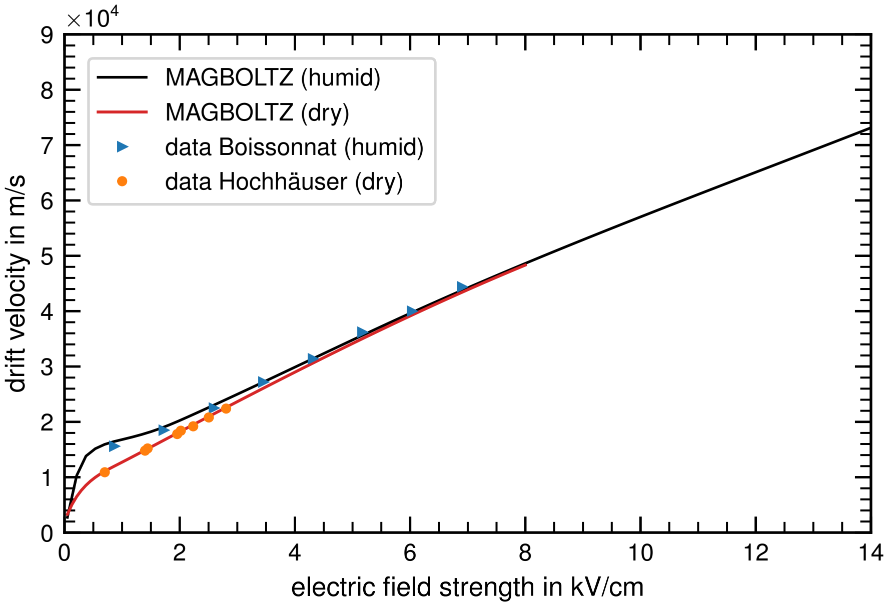

Figure 3.4: The electron velocity in humid (30 % relative humidity) and dry air. The available experimental data from Hochhäuser (1993) and Boissonnat (2015) are compared to interpolations of MAGBOLTZ calculations. The MAGBOLTZ calculation for humid air was used in the numerical k_s calculation

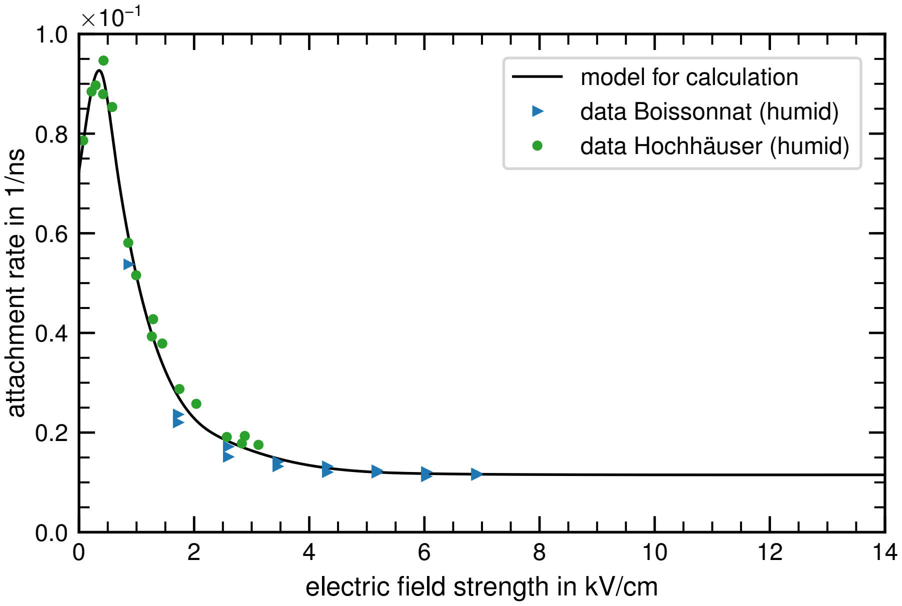

Figure 3.5: Attachment rate of electrons in air. Experimental data were taken from Hochhäuser (1993) and Boissonnat (2015). The inter- and extrapolation shown as a solid line is the attachment rate used in the numerical k_s calculation.

Air

As discussed in section 2.3.3 in an air-filled chamber positive and negative ions are heterogeneous groups whereas most available, experimental data of mobilities, such as Viehland and Mason (1995), considers very specific ions, such as N_2^+ in air. Constructing an average value of the ion mobility in air from such data is unfeasible. Therefore, measurements of ion mobility in air, specifically with air filled ionization chambers in mind, as performed by Boissonnat (2015), are used. Boissonnat (2015) reports values of $\mu_+ = 1.87 \cdot 10^{-4}\,\mathrm{m^2/(V\,s)}$ and $\mu_- = 2.09 \cdot 10^{-4}\,\mathrm{m^2/(V\,s)}$, which were used in the numerical k_s calculation.

The mobility and attachment rate of electrons sensitively depend on the electric field strength, such that a single value is not sufficient but rather a functional dependence of the parameters on the electric field strength (E) is required. Additionally, the usefulness of a mobility concept is strongly diminished when μ also depends on E, thus electron drift velocity is discussed directly in the following, instead of electron mobility.

Electron drift velocity and attachment rate were measured in air at different values of E by Hochhäuser (1993) and recently by Boissonnat (2015). In addition, these two parameters can be calculated from fundamental interaction cross sections by solving the Boltzmann-transport equation for electrons, for example, using a Monte-Carlo approach as implemented in the MAGBOLTZ program (Biagi, 1999).

Experimental and MAGBOLTZ data match very well for the electron drift velocity as can be seen in Fig. 3.4. The figure shows data for both synthetic dry air and humid air to illustrate the good agreement between the calculation and experiment for different settings. For input into the MAGBOLTZ program, humid air was approximated with a composition of 0.9390 % argon, 20.7074 % O_2, 77.1957 % N_2 and 1.1579 % water.

Due to this excellent agreement, MAGBOLTZ calculations were performed for values of the electric field from 50–14 000 V/cm at regular intervals every 50 V/cm. The results were interpolated using a cubic regression spline, which in turn was used as input for the calculation of k_s.

A spline was chosen because it allows the representation and efficient evaluation of an arbitrarily shaped smooth function without the need for further parameterization. The regression spline, as opposed to an interpolation, does not pass through every data point exactly, but finds a spline with the least possible number of knots (i.e., polynomial intervals) while keeping the deviation from the data to a specified margin. This allows for the smoothing of the statistical variations in the Monte-Carlo calculation results by finding a spline for which the reduced chi-squared is as close to 1 as possible. All the fitting calculations were performed using the Python SciPy wrappers for FITPACK (Dierckx, 1995).

Unfortunately, the MAGBOLTZ results for the attachment rate differed greatly from the experimental data (a factor of 10 for $E > 4$ kV/cm). Therefore, a model for the k_s calculation was derived solely from the experimental data shown in Fig. 3.5. To this end the experimental data above 2 kV/cm were fitted with a mono exponentially decreasing function. This exponential function was used to extrapolate the experimental data up to electric field values of 14 kV/cm. Subsequently, the entire available experimental data and the extrapolated data were fitted with a regression spline, which is also shown in Fig. 3.5.

For the recombination coefficient (α) no best value could be found in the literature. Reported values range from $2.3 \cdot 10^{-12}$ m^3/s (Sayers, 1938) to $1.17 \cdot 10^{-12}$ m^3/s (Ebert et al., 1964) and Boissonnat (2015) finds best consistency of his measurement with a value of $1.98 \cdot 10^{-12}$ m^3/s. Furthermore, several publications found a dependence of α on the “age” of the ions, that is the time between ion formation and measurement (Marshall, 1929; Ebert et al., 1964; McGowan, 1965). Due to this lack of a single consistent value, α was determined from fitting the numerical k_s calculation to the measured data.

N_2

While the equation system (2.7) and its solution were tailored for air as a sensitive medium its extension to other sensitive media is straightforward.

Pure N_2 can be considered fairly similar to air, because it is the major constituent of air. Thus and for simplicity the same ion mobilities as for air were used for N_2. The electron mobility in pure N_2 was determined by performing and subsequently interpolating MAGBOLTZ calculations for pure N_2. Electron attachment and the formation of negative ions should not occur in pure N_2 because N_2 cannot form stable negative ions (Gutsev et al., 1999). Therefore, the inclusion of another reaction term to allow for an ion-electron recombination of the form

$$\frac{\partial c_+}{\partial t} = \frac{\partial c_e}{\partial t} = -\beta c_+ c_e$$

is necessary to model a recombination in N_2. The value of β was determined from the experimental data itself, just like α was for air.

Table 3.3: Ion mobilities, recombination rates and relative permittivity used in the numerical k_s calculation for the two liquids as reported by Johansson and Wickman (1997). Because positive and negative charge carriers were not identified in that publication, the higher mobility was assigned to the negative charge carriers.

	μ_+ (m^2/(V s))	μ_- (m^2/(V s))	α (m^3/s)	ϵ_r
isooctane	$2.9 \cdot 10^{-8}$	$2.9 \cdot 10^{-8}$	$5.4 \cdot 10^{-16}$	1.94
TMS	$5.3 \cdot 10^{-8}$	$9.0 \cdot 10^{-8}$	$1.4 \cdot 10^{-15}$	1.84

Non-polar Liquids

The two liquids used (TMS and isooctane) obviously exhibit far different properties from air. Nevertheless, the principle of charge carriers accelerated in the electric field with a certain mobility and recombining with a certain recombination rate should still apply.

While free electrons can exist in liquids, usually called solvated electrons (Schindewolf, 1968; Dye, 2003), for recombination in the two liquids used here only ions are discussed in literature (Johansson and Wickman, 1997; Pardo-Montero et al., 2012). Pardo-Montero et al. (2012) found different ion species with different mobilities contribute to the charge transport. However, they attribute those to impurities in the isooctane and it is unclear how well these values and their relative strength transfer to other chambers with different impurities. Absent any data for an electron attachment rate or electron mobility, the consideration here was limited to one type of positive and negative ion each using the values from Johansson and Wickman (1997), conveniently providing measurements for both isooctane and TMS. Considering only positive and negative ions greatly simplifies the equation system (2.7) by removing the last equation and directly adding the production term $R(t)$ to the negative ion concentration.

In the recalculation of the electric field the polarizability of these substances has to be considered. The relative permittivity of air is approximated as $\epsilon_r = 1$, which allowed the calculation of E using only the free charges as there should be no bound charges. For a polarizable medium one should use the electric displacement field D if only considering the effects of free charges. However, assuming a linear, isotropic and homogeneous medium, it is also possible to directly obtain E by using $\epsilon_r\epsilon_0$ instead of ϵ_0. The relative permittivity is reported for the two liquids in table 3.3 along with the mobility and recombination rate values used.

4 Dose Rate Meter Investigation

4.1 Results

Determination of Reference Dose

Figure 4.1 shows homogeneity measurements performed with an IP as a 2-D heat map and in the form of two profiles along the x and y-axis. The largest dose rate meter, the RamION, has a diameter of 90 mm and up to 45 mm from the center the intensity variation is less than 5 %, providing sufficient homogeneity over the extent of the instruments.

Irradiation of the TLDs to establish a calibration of the ionization chamber measurement in front of the Faraday cup yielded comparable results for continuous and pulsed irradiation. The presented experiments were performed in two measurement periods of alloted beamtime and a calibration factor was determined each time yielding values of 4.86 ± 0.08 µGy/nC in the first period and 4.78 ± 0.17 µGy/nC in the second. The reference doses and dose rates reported throughout this section are calculated from ionization chamber readings and these factors.

Dose Rate Meter Response

Figures 4.2, 4.3 and 4.4 show the results of the measurements performed with the LB 1236-H10, the RamION and the 6150AD-b respectively, each for varying the dose-per-pulse and the pulse duration of the radiation field. The reference doses based on the TLD calibration of the ionization chamber measurement are reported in Gy because the TLDs were calibrated in terms of the absorbed dose to water. Yet, the dose rate meters were all factory calibrated for ambient dose equivalent $H^*(10)$, so their response is reported in Sv. However, the two quantities are numerically equal in the employed high energy photon field and the different units are only kept to highlight the difference in providence of the values. The error bars shown in the figures indicate ±20 % of the value, the maximum allowed deviation due to pulsation of the radiation field according to DIN IEC/TS 62743 (DIN, 2013).

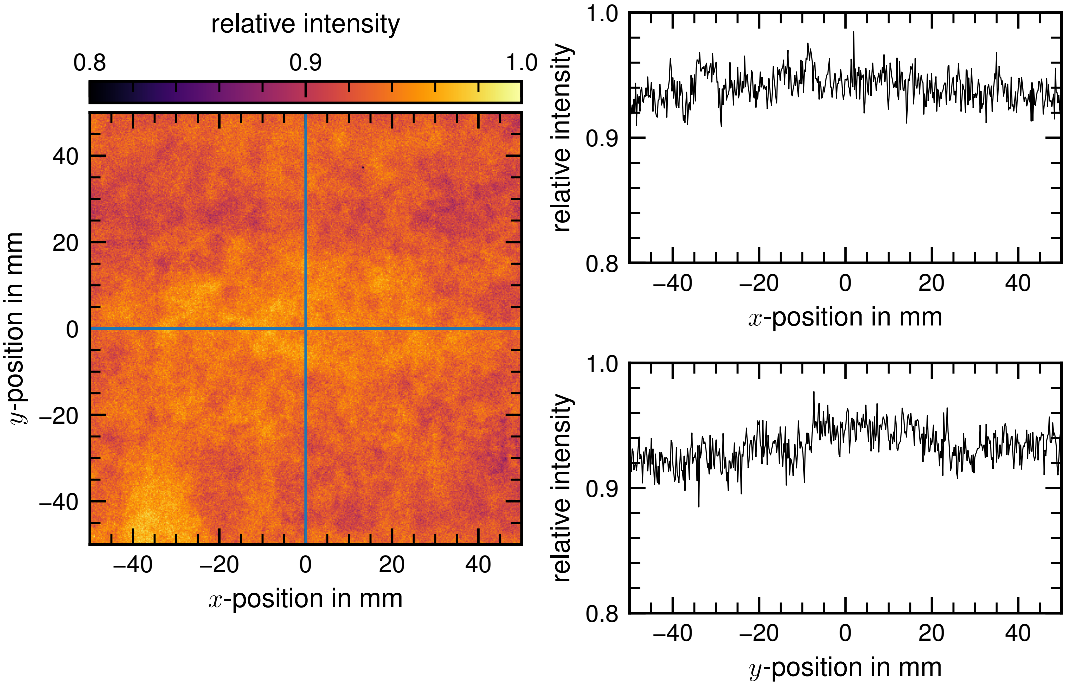

Figure 4.1: Measurements of the lateral field homogeneity at the position of the dose rate meters. The left hand image is a heat map representation of the image plate measurement, where the coordinate origin, marked by the cross, is the approximate location of the central axis. The profiles on the right were taken along these lines, parallel to the x-axis (top) and the y-axis (bottom). All intensities are reported relative to the maximum in the left hand image.

The LB 1236-H10 was irradiated with a continuous beam (Fig. 4.2a) in addition to the pulsed settings shown in Fig. 4.2b and 4.2c. The LB 1236-H10 shows a strong overresponse compared to the reference measurement by a factor of 2.65 calculated from the linear fit performed on the continuous data. This is most likely due to irradiating it 90° to its preference orientation for the sake of a common alignment for all the dose rate meters and due to the high energy of the photon field. The LB 1236-H10 is calibrated for energies up to 1.3 MeV and the mean photon energy here was estimated to be 4.8 MeV. The ideal response reported in Fig. 4.2b incorporates this overresponse and it should not influence the time structure dependent behavior.

A clear saturation of the measurement response is observable in the dose-per-pulse variation at high dose-per-pulse, leading to a discrepancy of over 20 % at dose-per-pulse values above 14.8 pGy. At saturation the instrument reports a value of 5.5 µSv/h, which corresponds to a count rate of 25.7 Hz. Varying the pulse duration results in a step-like

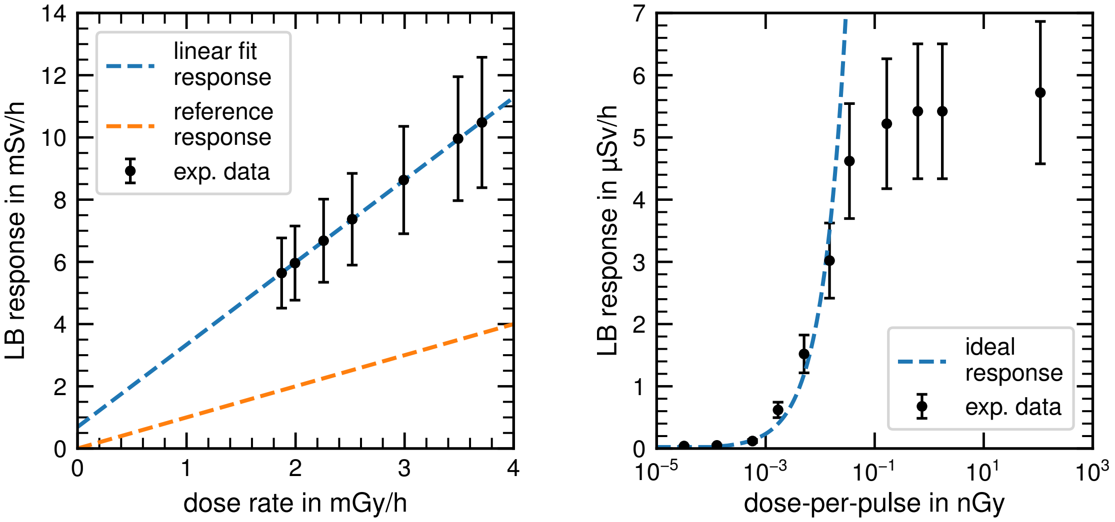

(a) continuous irradiation

(b) varied dose-per-pulse at t_{pulse} = 5 ps

(c) varied pulse duration at $\dot{D}_{\mathrm{avg}} = 16.5$ mGy/h

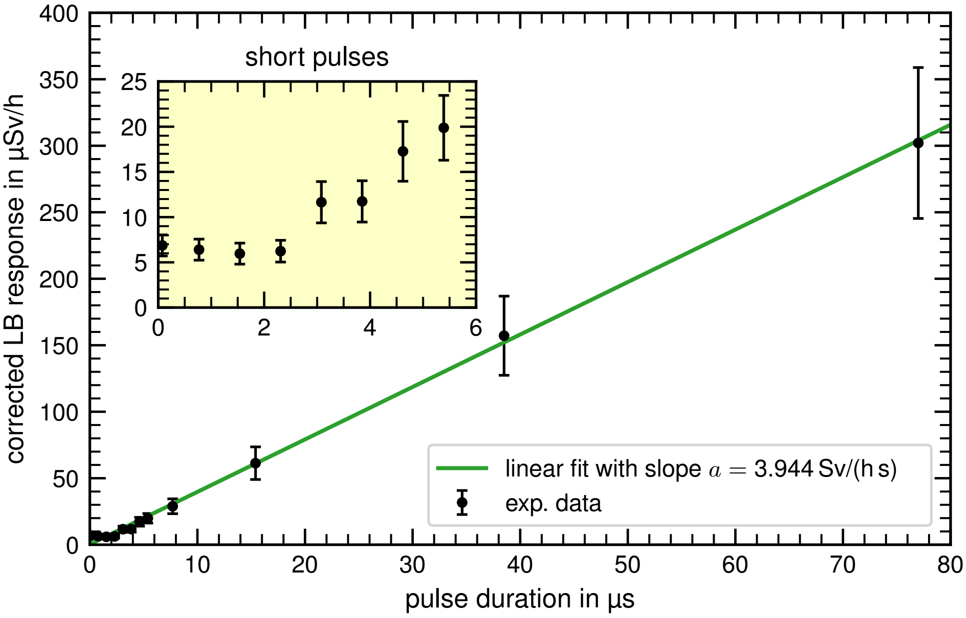

Figure 4.2: Measurement response of the LB 1236-H10 proportional counter in pulsed fields at a repetition rate of 25 Hz and under continuous irradiation. The linear fit in (a) was used to quantify the overresponse of the instrument with respect to the reference response calculated from the IC measurement. The ideal response shown in (b) is also calculated from the IC measurement, but incorporates that overresponse. The response in (c) was corrected for dose-per-pulse fluctuations. The linear fit in (c) allows the estimation of the maximally measurable pulse dose rate and the inset shows a magnification of the data for short pulse durations.

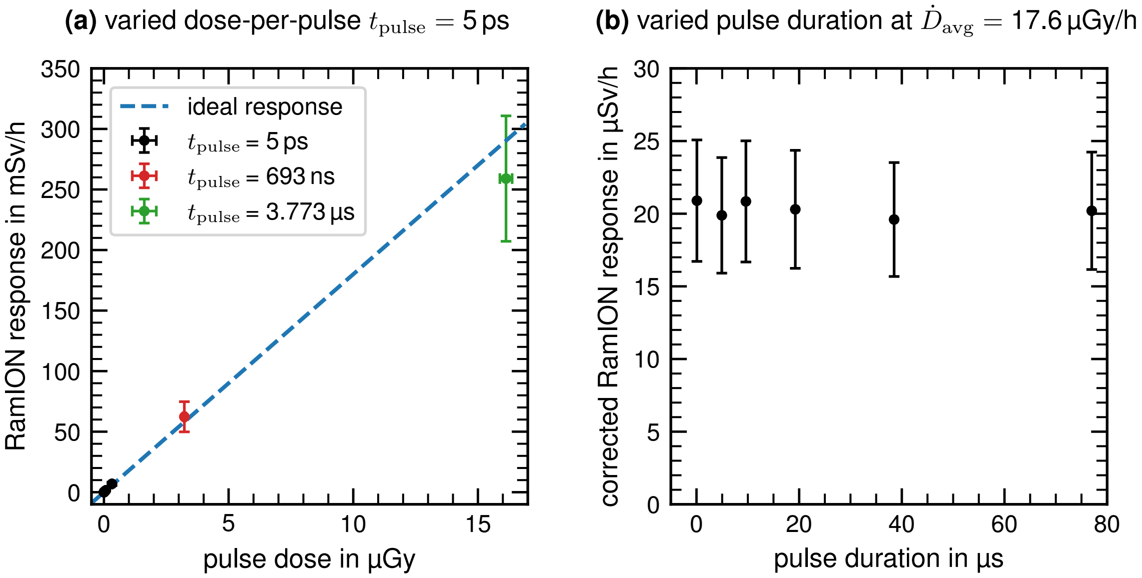

Figure 4.3: Measurements of the RamION ionization chamber at 5 Hz repetition rate while varying different pulse parameters. The ideal response in (a) is based on the reference measurement and the otherwise constant pulse duration was elongated to achieve the two highest dose points. The response in (b) was corrected for dose-per-pulse fluctuations.

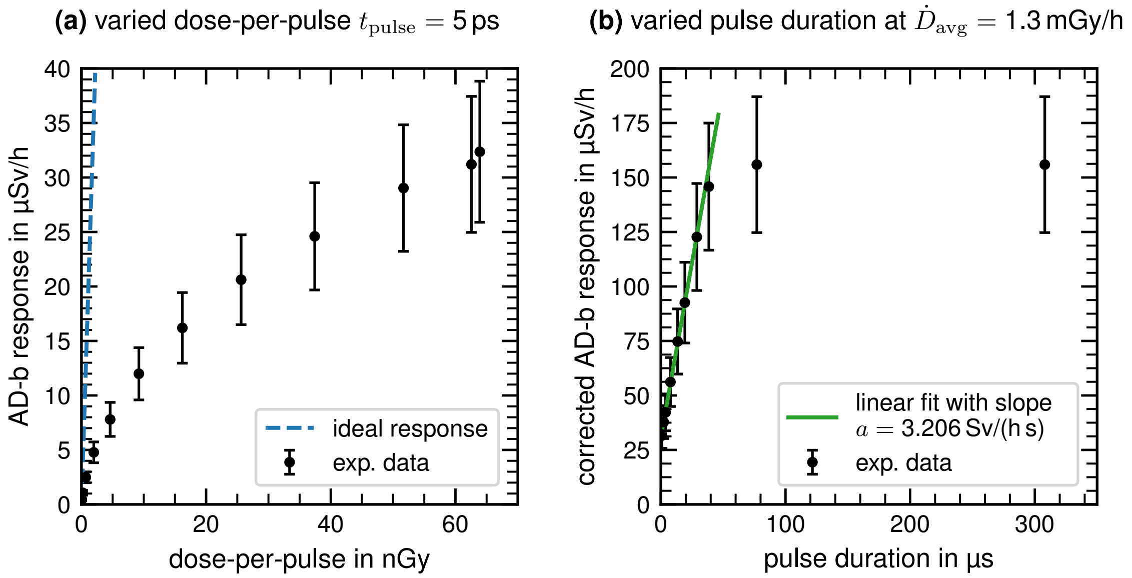

Figure 4.4: Measurements of the 6150AD-b scintillator at 5 Hz repetition rate. The linear fit in (b) was performed for pulse durations $< 40\,\mu\mathrm{s}$ to estimate the maximally measurable pulse dose rate. The response in (b) was corrected for dose-per-pulse fluctuations.

increase of the response between pulse durations of 2.31 µs and 3.08 µs as well as between 3.85 µs and 4.62 µs. At longer pulse durations this step behavior disappears and transitions into a linear relationship between pulse duration and displayed dose rate.

The RamION's response (shown in Fig. 4.3) is within 20 % of the reference measurement for both the dose-per-pulse and the pulse duration variation. To extend the accessible dose-per-pulse range the RamION was not only irradiated with pulses containing a single bunch ($t_{\mathrm{pulse}} = 5\,\mathrm{ps}$), but also with pulses containing 10 and 50 bunches. The resulting pulse durations of 0.693 µs and 3.773 µs are still short compared to typical ion collection times, which are at least several 10 µs, and should have no influence on the reading. At the highest dose-per-pulse used the RamION underresponds compared to the reference, while still within the maximum allowed deviation of 20 %. Whereas at all other doses it overresponds, for instance, in the pulse duration variation it measures around 20 µSv/h for a reference rate of 17.3 µGy/h.

The 6150AD-b exhibits an increasing deviation between instrument reading and reference values with increasing dose-per-pulse shown in Fig. 4.4a. However, no clear plateau is observed only a continuously decreasing slope. An underresponse by over 20 % is present even at the lowest dose-per-pulse of 39 pGy used. The pulse duration variation (Fig. 4.4b) shows a linear relationship between pulse duration and reported dose rate at low pulse durations. However, the measured dose rate saturates at a value of 156.5 µSv/h.

4.2 Discussion and Conclusion

Of the three dose rate meters investigated only the RamION measured the correct dose rate for all the pulse settings tested. Below, each instrument is discussed separately to draw more generalized conclusions regarding the origins of their limitations based on detector type.

RamION

Generally the RamION measured the correct dose rate in all the pulsed fields tested. Although there is indication for an underresponse at the highest dose-per-pulse used, which is probably due to ion recombination in the chamber, it is still well within the 20 % accuracy margin demanded by DIN IEC/TS 62743 (DIN, 2013). In addition, the dose-per-pulse of

16.5 µGy is quite high, which is most easily realized by considering the operational dose rate limits for continuous fields (table 3.1). Those limits give a good idea of the average dose rates typically encountered with such instruments and they should be similar for a pulsed source assuming similar shielding. The most strongly pulsed systems with a prospective use in medicine are laser based particle accelerators, usually estimated to have repetition rates of 10 Hz. 16.5 µGy at 10 Hz corresponds to an average dose rate of 594 mGy/h, which is beyond the specification of the RamION, even in a continuous field. An even more strongly pulsed source at 1 Hz would still be reliably measured up to an average dose rate of 59.4 mGy/h. While lower than the RamION's operational limits for continuous fields, this is still far in excess of the 3 mSv/h limit for an exclusion area in German radiation protection. As long as these limits are kept in mind, the RamION should report correct dose rates in most pulsed fields.

LB 1236-H10

The saturation count rate of the LB 1236-H10 of 25.7 Hz in the dose-per-pulse variation corresponds closely to the pulse repetition rate of the radiation field of 25 Hz. The instrument simply measures one count event per radiation pulse, which is at 5 ps much shorter than the dead time. The dose-per-pulse for which the measurement of such a short pulse duration deviates by more than 20 % can be deduced from the counting statistics. The number of ionization events per radiation pulse (k) is Poisson distributed with a probability $P(k) = \frac{\lambda^k}{k!}e^{-\lambda}$ and an expectation value λ. Thus, the true count rate would be $n = \lambda f_{\mathrm{rep}}$. However, the detector registers at most one count, regardless of how many more ionization events occur during a pulse. Therefore, the measured count rate m is given by the probability of at least one ionization event during a pulse multiplied with the repetition rate

$$m = P(k > 0) \cdot f_{\mathrm{rep}} = (1 - P(0)) \cdot f_{\mathrm{rep}} = \left(1 - e^{-\lambda}\right) \cdot f_{\mathrm{rep}}.$$

Using this expression the average number of ionization events per radiation pulse λ at which true and measured count rates differ by more than 20 % can be estimated from the inequality

$$1.2 \cdot \left(1 - e^{-\lambda}\right) \cdot f_{\mathrm{rep}} > \lambda \cdot f_{\mathrm{rep}}.$$

A second order expansion of the exponential function allows an approximate solution resulting in $\lambda \lesssim 0.33$.

The calibration factor of the LB 1236-H10 is $G_{\mathrm{count}} =$ 59.44 pSv/count (Berthold Technologies GmbH & Co. KG, 2007), so the dose-per-pulse corresponding to an average of one event per pulse ($\lambda = 1$) is 59.44 pSv. The measured dose-per-pulse limit of 14.8 pGy (see Fig. 4.2b) is 25 % of that dose instead of the calculated limit of 33 %. However, in all these measurements a background was subtracted, increasing the apparent dead time. In conclusion, the observed behavior of the LB 1236-H10 corresponds reasonably well to the expected performance of a counting detector in a field of very short pulses.

The stepwise response increase with increasing pulse duration, seen in the inset in Fig. 4.2c, is likewise a result of the instrument's dead time. Each pulse triggers multiple ionization events in the detector, but for the shortest pulses only one count is registered. As the pulse duration is increased beyond the dead time the detector recovers once during the pulse and two counts are registered and so on. Averaging the positions of the first two steps the dead time is estimated as 2.4 µs, a typical value for a proportional counter (Hashimoto et al., 1996).

The stochastic nature of the ionization events and the increasing relevance of the internal dead time correction smear the steps as longer pulses are applied, transitioning to a linear relationship between pulse duration and measured dose rate. The slope of this linear relationship is $a = \dot{H}_{\mathrm{meas-avg}}/t_{\mathrm{pulse}}$ with the measured average dose rate $\dot{H}_{\mathrm{meas-avg}}$. The average dose rate expressed in terms of the pulse dose rate is $\dot{H}_{\mathrm{avg}} = \dot{H}_{\mathrm{pulse}} \cdot t_{\mathrm{pulse}} \cdot f_{\mathrm{rep}}$. Thus,

$$\frac{a}{f_{\mathrm{rep}}} = \dot{H}_{\mathrm{meas-pulse}},$$

allowing the calculation of a measured pulse dose rate using the slope given in Fig. 4.2c. For the LB 1236-H10 this is $\dot{H}_{\mathrm{meas-pulse}} =$ 158 ± 2 mSv/h.

Taking the formula suggested in DIN IEC/TS 62743 (DIN, 2013) to calculate the maximally measurable pulse dose rate (eq. (2.21)), with the calibration factor given above and the estimated dead time of 2.4 µs, yields a much lower value of $\dot{H}_{pulse-max} =$ 22.3 mSv/h. The apparently much better than predicted performance of the LB 1236-H10 lies in the internal dead time correction of the instrument. 158 ± 2 mSv/h corresponds to a count rate of 738 Hz implying a dead time of at most 1.4 µs much shorter than what was actually observed. The problem of the dead time correction is that it is designed for a continuous field, depending on the average count rate. A field with a lower repetition rate and the same pulse dose rate would yield a lower count rate and would trigger less dead time correction, reducing the measured pulse dose rate. This is to say that the estimation based on DIN IEC/TS 62743 (DIN, 2013) is not overly cautious, but rather more realistic when one wants to ensure that the pulse dose rate can be measured under any condition, even for single pulses.

6150AD-b

The scintillator in the 6150AD-b has no associated dead time like the proportional counter LB 1236-H10. However, a saturation in the response is still observed, probably due to effects in the PMT used to detect the light emitted by the scintillator. The linear amplification range of a PMT is determined by the general construction and the applied voltage. Since the 6150AD-b is tuned for high sensitivity (down to 100 nSv/h) the high momentary photon fluxes from the pulsed irradiation probably exceed the limits of the PMT.

The upper limit of the instrument's response in the pulse duration variation is probably due to some conversion circuitry in the instrument. For instance, the instrument converts the measured PMT charge to a frequency to transmit its measurement to the readout unit. At 156.5 µSv/h the measured dose rate exceeds the instrument specification (max: 100 µSv/h) and this might be the maximum frequency that can be registered by the readout unit. Analyzing the slope of the pulse duration measurement gives $\dot{H}_{\mathrm{meas-pulse}} = 640 \pm 3\,\mathrm{mSv/h}$. A value much higher than that of the LB 1236-H10, but still far below the recommended minimum of 1 Sv/h (DIN, 2013).

Overall the behavior of the 6150AD-b is the most difficult to analyze and predict because of the many conversion steps the signal undergoes. In principal, a scintillation detector should be well suited for the detection of pulsed radiation, nevertheless such a system is still constrained by the achievable dynamic range. The detector can measure a pulse dose rate far in excess of its specified stationary dose rate, but still too low to be a considered for measurements of pulsed fields. A detector such as the 6150AD-b, which is tuned for high sensitivity, is therefore not well suited for a pulsed field with very high momentary dose rates.

DIN IEC/TS 62743

Generally, the limits suggested by DIN IEC/TS 62743 (DIN, 2013) appear very sound, based on the results of the LB 1236-H10, which was the only counting detector investigated here and consequently the only detector to fully fall within the norm's purview. At the same time this highlights the most severe limitation of the DIN IEC/TS 62743. Out of the three detectors the LB 1236-H10 is arguably the least suited for measurements of a pulsed field as investigated here. Conversely, no normative framework exists to test the other, more suitable detectors.

DIN IEC/TS 62743 is probably quite useful in the context of interventional radiology, where radiation fields with relatively long pulse durations (several ms) and consequently low pulse dose rates (around tens Sv/h) are used. However, most sources for radiation therapy use much shorter pulse durations, for example, the ubiquitous LINAC has a pulse duration of a few microseconds. The usefulness of DIN IEC/TS 62743 is severely diminished in this case, because detectors with a dead time shorter than the pulse duration and capable of measuring sufficiently high pulse dose rate do not exist. In addition, in the context of non-counting detectors, the usefulness of a pulse dose rate as the decisive limit in general is drawn into question. For any naturally integrating detector, such as an ionization chamber, the pulse dose rate is mostly irrelevant if the pulse duration is shorter than a critical time constant, such as the ion-collection time in an ionization chamber. Instead, the dose-per-pulse is the major determining factor for the accuracy of the measurement. Therefore, it would be useful to standardize to procedures to test non-counting detectors in pulsed fields, preferably centered around establishing a dose-per-pulse limit.

Conclusion and Outlook

Based on the observations made here only an ionization chamber based dose rate meter can be recommended for usage in a highly pulsed field. This conclusion, however, is based on the limited number of instruments analyzed here, with only one instrument for each operating principle. The limitations of the scintillator based instrument, for example, probably were not inherent to the detection principle, but more likely due to the specific choices made for that instrument.

The performance of the AD-b scintillation detector shows that the dynamic range required to have a very sensitive instrument, which also accurately measures strong pulses, cannot be achieved. Leading to the conclusion to generally caution against the usage of very sensitive instruments. Yet, without a standardized testing procedure, it is left to the end user to verify proper operation in a highly pulsed field, for any instrument chosen.

Unfortunately, even the recent development in the form of DIN IEC/TS 62743 (DIN, 2013) offers little relief, due to its limitation to counting detectors. It characterizes very well the limits of those counting detectors, but these limits are so far from the requirements in a highly pulsed field, to be essentially useless. A more general testing framework, for dose rate meters of any operating principle, would be much more useful.

With a German version of this investigation (Gotz et al., 2015) being taken up as literature of the German radiation protection commission (SSK) and identifying the dose-per-pulse as the most useful limiting quantity an important contribution towards such a general testing has been achieved.

5 Ionization Chamber Investigation

5.1 Field Homogeneity and Stability

Figure 5.1 shows the lateral beam profile at the position of the ionization chamber for the Advanced Markus chamber and the PinPoint chamber measurements. These dose distributions were calculated from EBT2-Films irradiated directly in front of the ionization chamber. For both measurements the lateral variation across the sensitive area is within $\pm 10\,\%$ of the mean.

Figure 5.2 shows the results from analyzing scintillator images, taken in the last measurement period with the isooctane LIC. Shown is the difference between the measured center of the beam and the reference position given by the alignment lasers in the experimental bunker. Several measurements were taken at each combination of dose-per-pulse and pulse duration. The shown data are averages of those measurements and the uncertainty shown as the error bars is the standard error of the mean. A clear dependence of the beam position on the pulse duration can be observed, while the variations with dose-per-pulse are mostly within the shot-to-shot variations.

5.2 Uncertainty Considerations

Following the recommendations in the guide to the expression of uncertainties in measurement (JCGM, 2008) each component used in the calculation of the measured k_s was evaluated for its uncertainty:

- The method used to determine the uncertainty of the ratio $\frac{M_\mathrm{FC}}{M_\mathrm{IC}-M_\mathrm{IC}^0}$ was dependent on the measurement series under consideration. In the case of the dose-per-pulse variation the standard deviation of multiple measurements at the same setting could be used. In the case of the pulse duration variation a linear regression of all the measurements at the same setting was performed to extrapolate and correct for variations

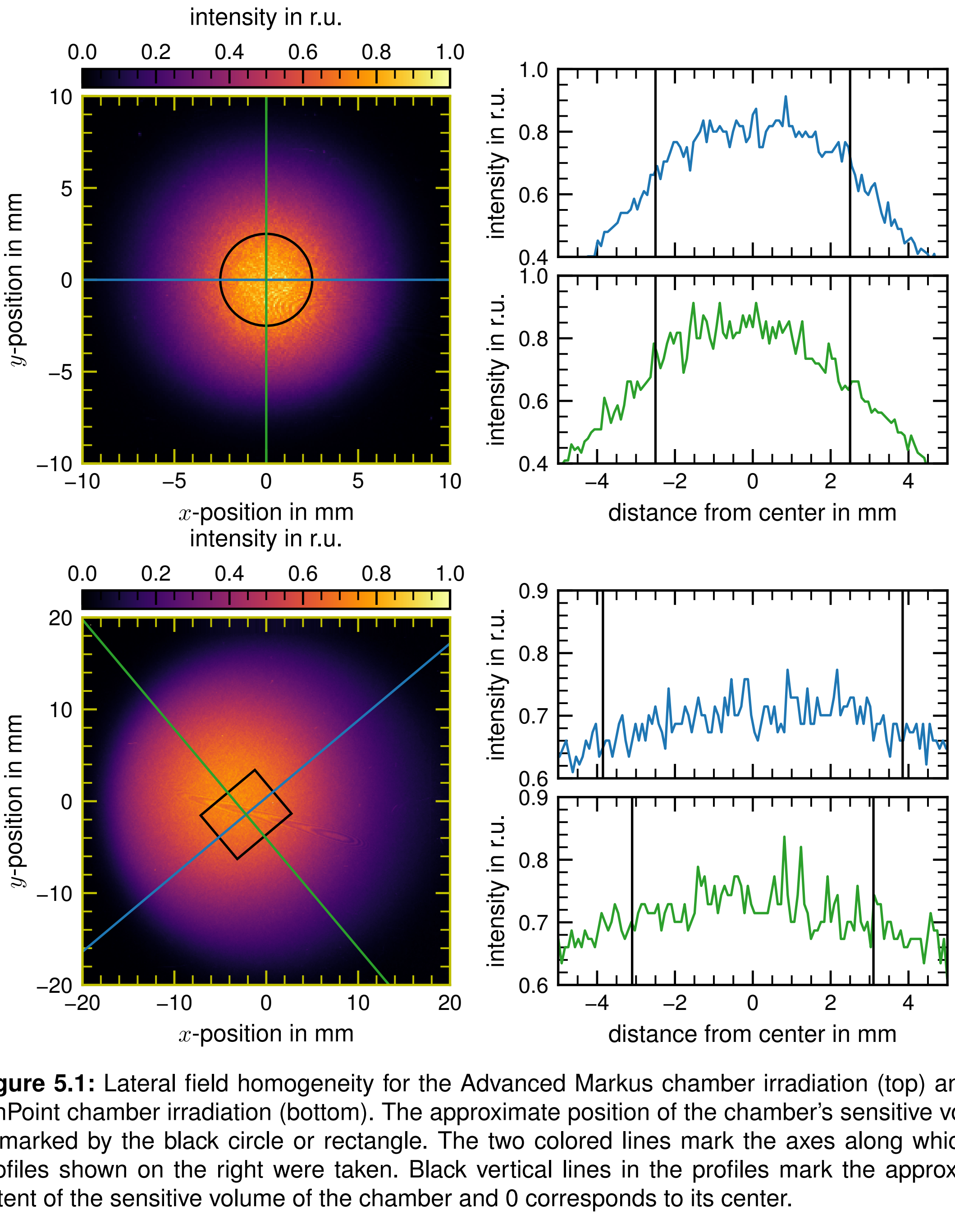

Figure 5.1: Lateral field homogeneity for the Advanced Markus chamber irradiation (top) and the PinPoint chamber irradiation (bottom). The approximate position of the chamber's sensitive volume is marked by the black circle or rectangle. The two colored lines mark the axes along which the profiles shown on the right were taken. Black vertical lines in the profiles mark the approximate extent of the sensitive volume of the chamber and 0 corresponds to its center.

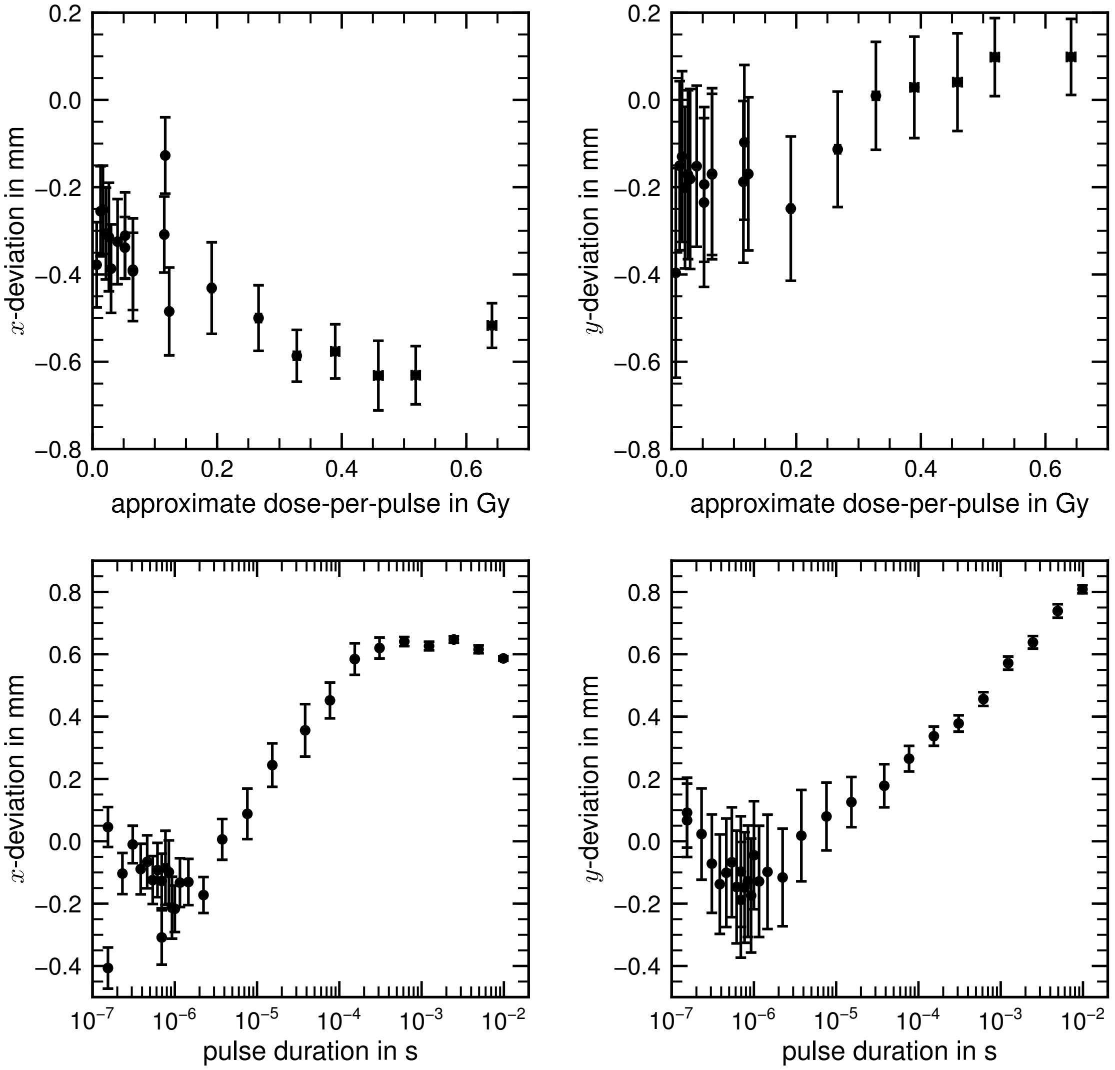

Figure 5.2: The deviation of the beam spot center from the reference position in dependence of dose-per-pulse (top row) at a fixed pulse duration of 693 ns and on the pulse duration (bottom row) at a fixed dose-per-pulse of approximately 0.12 Gy. For both variations a deviation in x (horizontal) and y (vertical) direction is shown.

in the applied dose-per-pulse. The standard error of this regression was used to calculate an uncertainty of the estimated ratio at the targeted dose-per-pulse.

- The background correction M_{IC}^{0} contributes an uncertainty that varied based on the chamber used. It was estimated from repeated background measurements and was around 20 % for the measurements with the Advanced Markus chamber in air, almost 50 % for those in N_2, around 10 % for the PinPoint chamber measurements, and around 40 % for the LICs.

- The relative gain of the Faraday cup electronics c_{amp} is defined as exactly 1 for the higher gain and the uncertainty for the lower gain setting was estimated as 1.3 % from the calibration experiment used to determine this gain factor.

- The fit used to determine the calibration factor of the Faraday cup (c_{calib}) was also used to estimate its uncertainty. It ranged from 0.5 % for the gas filled chambers to 1.5 % for the LICs. The systematic drift of the beam with changing pulse duration observed in the last experiments with the LIC would also cause a change in the calibration factor, because the entire beam spot is collected by the Faraday cup but the part used to irradiate the ionization chamber changes. To account for this effect a pulse duration dependent uncertainty was added, which was estimated by evaluating the change in dose-per-pulse applied to the chamber when the beam position changes by the observed values. This resulted in an additional uncertainty that is 0 at the pulse duration used for the calibration fit and increases up to 1 % at the longest pulse duration of 308 µs.

Combining these contributions and multiplying by a coverage factor $k = 2$ to approximate 95 % coverage, gave the values shown as the error bars in the k_{s} measurements. Due to this combination the very large uncertainty in M_{IC}^{0} only gave a relevant contribution for low dose-per-pulse measurements with the Advanced Markus chamber in air. For the other measurements M_{IC}^{0} was relatively small compared to M_{IC} such that its large uncertainty was mostly irrelevant. The other uncertainties were of comparable size contributing about equally to the overall uncertainty in k_{s}.

Table 5.1: The parameters obtained from fitting $(k_\mathrm{s})'_\mathrm{th}$ to the experimental data as well as the reduced chi-squared χ^2_ν calculated for each fit.

U_c	50 V	100 V	300 V	400 V
a (nC^{-1})	19.5 ± 0.4	6.8 ± 0.3	1.12 ± 0.04	0.76 ± 0.04
p	0.173 ± 0.006	0.072 ± 0.020	$(1.3 \pm 8.3) \cdot 10^{-3}$	$(1.4 \pm 11.3) \cdot 10^{-3}$
χ^2_ν	1.63	2.43	4.67	2.04

5.3 Advanced Markus Chamber in Air

5.3.1 Experimental and Calculation Results

Dose-per-Pulse Dependent Measurements

Figure 5.3 shows the measured saturation correction factor for an Advanced Markus chamber in dependence on the dose-per-pulse. The pulse duration for these measurements was fixed at $t_\mathrm{pulse} = 3.773\,\mu\mathrm{s}$ and measurements were performed at four different values of $U_\mathrm{c} = 50$ V, 100 V, 300 V and 400 V shown in the different sub-figures. The measurements are compared to two theoretical descriptions. The numerical calculation developed within the scope of this thesis $(k_\mathrm{s})_\mathrm{num}$ and a least-squares fit of Boag et al.'s (1996) $(k_\mathrm{s})'_\mathrm{th}$ from eq. (2.10). The parameters used in the numerical calculation were outlined in section 3.4.3 except for the recombination coefficient α which was determined from a fit of $(k_\mathrm{s})_\mathrm{num}$ to the data at $U_\mathrm{c} = 50$ V as $\alpha = 1.282 \cdot 10^{-12}$ m^3/s. The fit of $(k_\mathrm{s})'_\mathrm{th}$ was performed to give the best case scenario of this model and its two parameters a and p were both adjusted for each value of U_c independently. The resulting values are reported in table 5.1.

The most striking difference is observed between the lower collection voltages of $U_\mathrm{c} =$ 50 V and 100 V on the one side and the higher values of $U_\mathrm{c} =$ 300 V and 400 V on the other side. The shape of the dose-per-pulse dependence differs fundamentally between these two groups. For the lower U_c values k_s increases most strongly for low dose-per-pulse values with a gradually flattening curve (concave over the entire domain). For the higher U_c values the change in k_s is initially almost flat, increases steeply and then flattens again, giving an initially convex and then concave curve.

This has immediate consequences for the reproduction of the experimental data by the theoretical descriptions. Both $(k_\mathrm{s})_\mathrm{num}$ and $(k_\mathrm{s})'_\mathrm{th}$ reproduce the experimental data within the measurement uncertainty at the two lower U_c values, while they deviate from the experi-

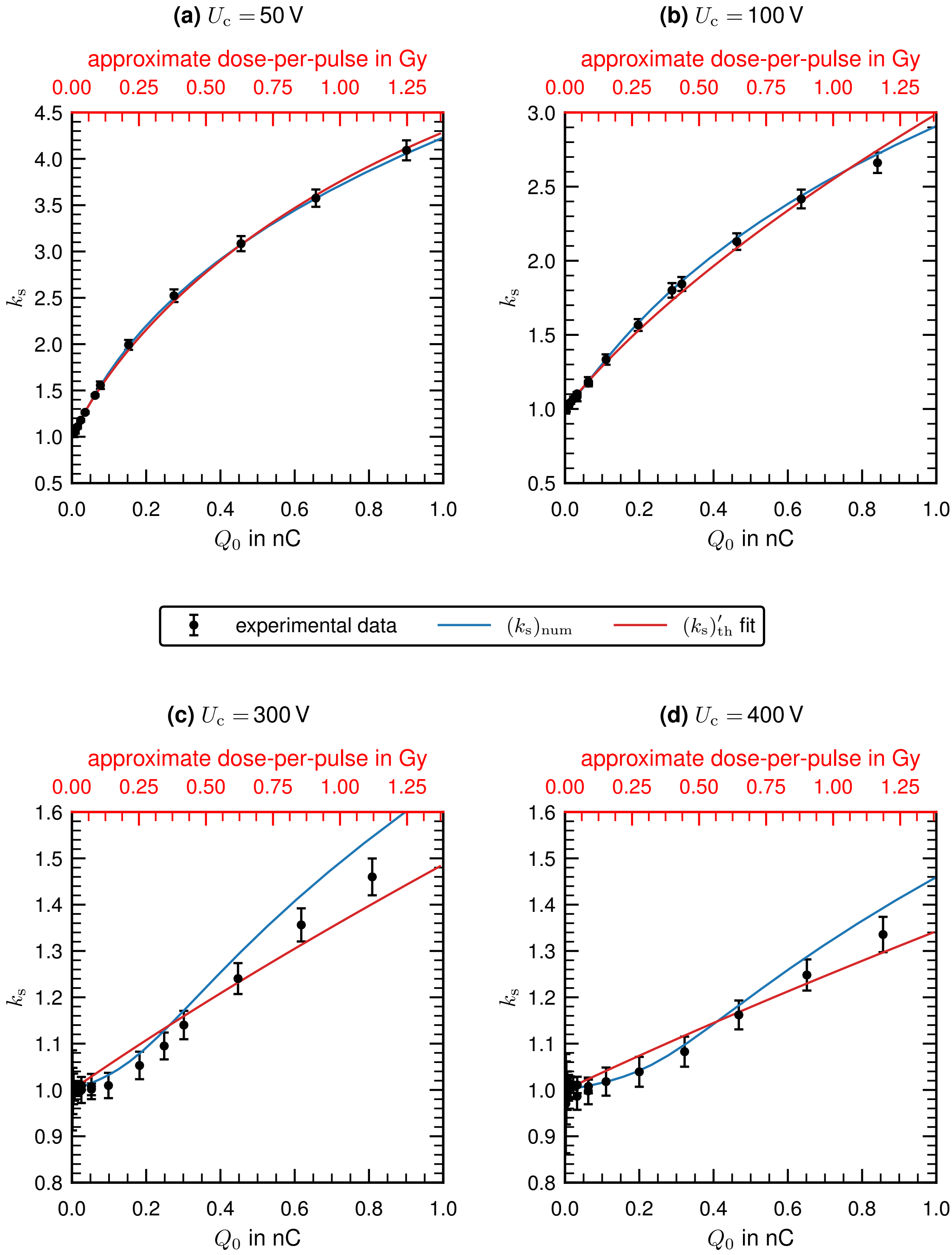

Figure 5.3: k_s of an Advanced Markus chamber in dependence on the dose-per-pulse at different collection voltages. Experimental data are compared to corresponding numerical calculations ($(k_s)_{num}$) and fits based on eq. (2.10) ($(k_s)'_{th}$). The error bars approximate 95 % coverage (coverage factor $k = 2$). The top axis shows the photon dose-per-pulse in water that would evoke the corresponding liberated charge on the bottom axis. It is provided as a more familiar comparison point to the liberated charge, which was used in the calculations.

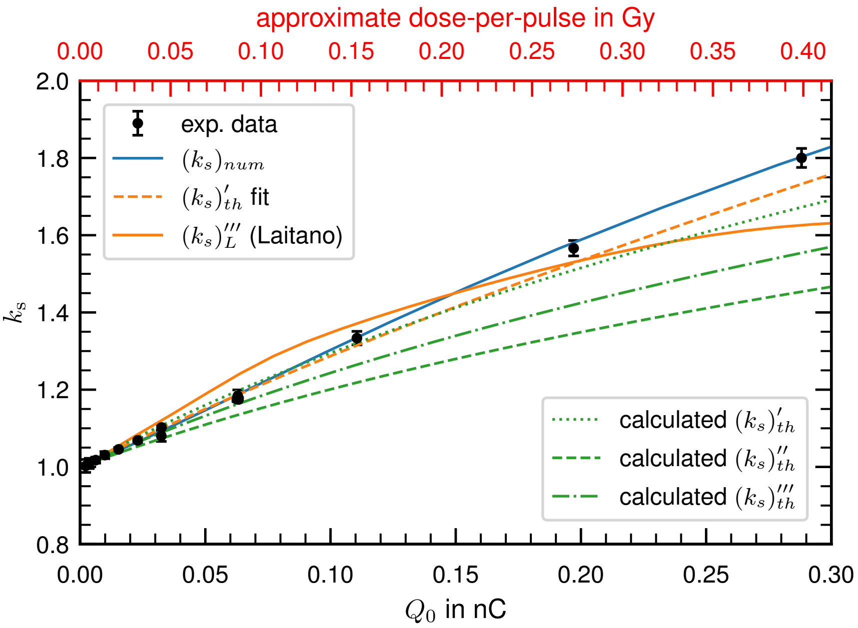

Figure 5.4: k_s for the Advanced Markus chamber at $U_\mathrm{c} = 100\,\mathrm{V}$ at low dose-per-pulse values. The same experimental data as in Fig. 5.3b is compared to various possible calculation methods

mental data at the two higher U_c values. However, this deviation is a systematic overestimation of k_s in the case of $(k_\mathrm{s})_\mathrm{num}$ whereas $(k_\mathrm{s})'_\mathrm{th}$ overestimates k_s at low dose-per-pulse and under estimates it at high dose-per-pulse. In addition, the $(k_\mathrm{s})_\mathrm{num}$ appears to better reproduce the experimental data at $U_\mathrm{c} = 400\,\mathrm{V}$ than at 300 V. In the latter setting $(k_\mathrm{s})_\mathrm{num}$ is within the experimental uncertainty up to a liberated charge of $Q_0 = 0.5\,\mathrm{nC}$.

The bad reproduction of the experimental data by the fit of $(k_\mathrm{s})'_\mathrm{th}$ also shows in the obtained parameters in table 5.1. They appear to be disconnected from their original physical meaning, with neither the free electron fraction p, which should be increasing with increasing U_c, nor a, which should scale with $1/U_\mathrm{c}$ (eq. (2.9)), following the respective expectations.

Figure 5.4 shows the same experimental data as Fig. 5.3b, but enlarges the low dose-per-pulse region. It also compares the experimental data to a wider range of methods to calculate k_s. The fit of $(k_\mathrm{s})'_\mathrm{th}$, the same as in Fig. 5.3, is the method suggest by di Martino et al. (2005). Whereas, $(k_\mathrm{s})'''_\mathrm{Laitano}$ is the modified two voltage method suggested by Laitano et al. (2006) (see section 2.3.3). The value of p for Laitano et al.'s approach was calculated using the same mobility and attachment values as in the numerical calculation and the measurements at $U_\mathrm{c} = 50\,\mathrm{V}$ were used as the second voltage to determine a in this modified two voltage approximation.

Furthermore, the same parameters as used for the numerical calculation were used to calculate values for a and p based on eq. (2.9) and (2.14) and expressions $(k_\mathrm{s})'_\mathrm{th}$, $(k_\mathrm{s})''_\mathrm{th}$ and $(k_\mathrm{s})'''_\mathrm{th}$ were evaluated using those calculated a and p values.

All three calculated expressions show a similar dose-per-pulse dependence of a flattening, concave curve. They differ primarily in the initial slope, with $(k_\mathrm{s})'_\mathrm{th}$ having the steepest slope, $(k_\mathrm{s})''_\mathrm{th}$ having the most gradual one and $(k_\mathrm{s})'''_\mathrm{th}$ having an intermediate slope. All three calculations underestimate k_s at high dose-per-pulse. Due to the steeper slope this underestimation is least pronounced for $(k_\mathrm{s})'_\mathrm{th}$ staying within the measurement uncertainty up to about $Q_0 =$ 0.15 nC. However, this is accompanied by an overestimation of k_s at low dose-per-pulse.

Laitano et al.'s (2006) method exhibits this combination of over- and then underestimation to an ever greater extent. It strongly overestimates k_s between $Q_0 =$ 0.015 nC and 0.13 nC and subsequently underestimates it above $Q_0 =$ 0.2 nC.

All the approaches to calculate k_s, except for the numerical model, are based on Boag's expression. Therefore, no such comparison was performed for the higher collection voltages, since even choosing parameters from a best fit fails to reproduce the data using this expression (see Fig. 5.3).

Pulse Duration Dependent Measurements

Measurement results of k_s for a varied pulse duration are shown in Fig. 5.5. At all values of U_c k_s decreases mono-exponentially for durations $t_\mathrm{pulse} >$ 1 µs. For $U_\mathrm{c} =$ 50 V an additional exponential component may be observable at short pulse durations $t_\mathrm{pulse} <$ 500 ns.

Those experimental data are compared to numerical calculations of k_s obtained with the same input parameters as for the dose-per-pulse dependent calculations. $(k_\mathrm{s})_\mathrm{num}$ reproduces the decreases at longer pulse durations well, but fails to replicate the short time component observed for $U_\mathrm{c} =$ 50 V.

5.3.2 Comparison to Literature

Previous measurements of the saturation correction of an Advanced Markus chamber were performed by Cella et al. (2010) and Ghorbanpour Besheli et al. (2016) using dose-per-pulse values up to 70 mGy and 40 mGy respectively. Generally, they found good agreement between their measurements and calculations using the approaches of Laitano et al. (2006)

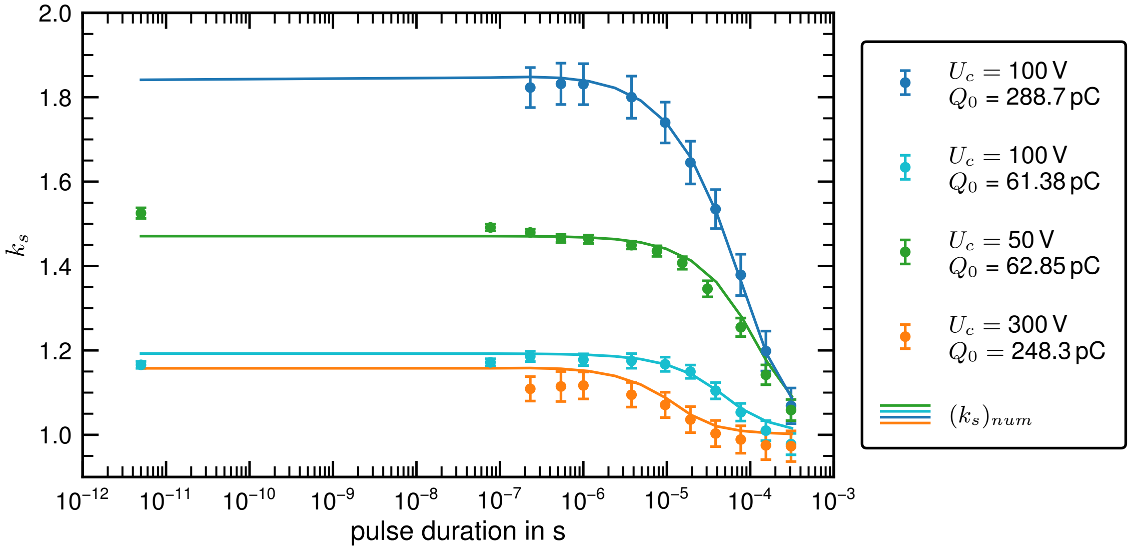

Figure 5.5: k_s dependence on the pulse duration for the Advanced Markus chamber for different values of U_c and Q_0. The experimental data are compared to numerical calculations of k_s.

or di Martino et al. (2005). This finding could not be replicated here. Especially at the higher collection voltages of 300 V and 400 V Boag's model, which is the foundation for both approaches, does not describe the observed behavior well.

The literature data is given in terms of k_s in dependence on dose-per-pulse. However, strictly speaking k_s depends on the liberated charge, from which dose-per-pulse is determined via the multiplication with several calibration and correction factors (eq. (2.1)). The factors used should depend on the experimental conditions, so using the dose-per-pulse as the independent variable is only a valid comparison for sufficiently similar experimental conditions. In order to make a meaningful comparison an attempt is made to reconstruct the factors and determine the liberated charge from given dose-per-pulse values. The calibration factor for the literature data was assumed as $N_\mathrm{w} = 1.385 \cdot 10^9$ Gy/C, the nominal response of the Advanced Markus chamber as specified by the manufacturer (PTW, 2016). Both literature measurements were performed using electron beams. The hypothesized calculation of the electron quality factor ($k_\mathrm{E} = k'_\mathrm{E} k''_\mathrm{E}$) was based on DIN 6800-2 (DIN, 2008), which gives the chamber dependent factor as $k''_\mathrm{E} = 0.985$ and the beam quality dependent factor as $k'_\mathrm{E} = 1.106 - 0.1312 \cdot (R_{50})^{0.214}$. The halfvalue depth ($R_{50}$) in turn was calculated from the electron beam's mean energy (E_0) using $E_0 = 0.656 + 2.059 R_{50} + 0.022 (R_{50})^2$

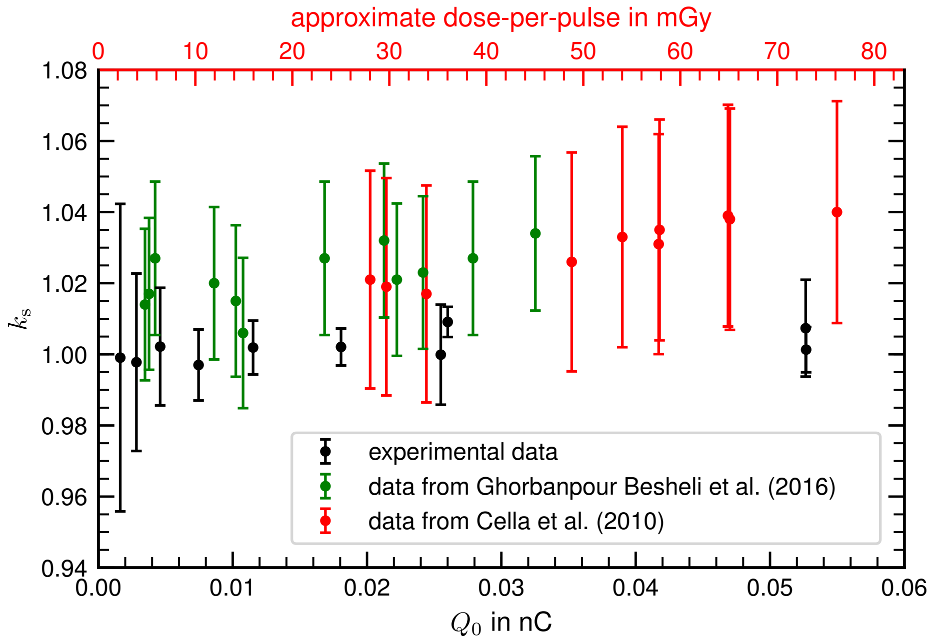

Figure 5.6: Comparing the measured k_s data to literature for the Advanced Markus chamber at $U_c = 300$ V. The error bars show an unexpanded uncertainty (coverage factor $k = 1$).

(Gerbi et al., 2009). This mean energy was given in the literature alongside the k_s measurements. Having no indication to the contrary, all other correction factor were assumed as $k_i = 1$.

The resultant comparison is shown in Fig. 5.6. While the k_s in the literature data is higher than the one determined here, all the data sets are in agreement within one standard deviation of the uncertainties. This serves as a check on the validity of the experimental data obtained here and shows that different conclusions are probably not due to fundamentally different measurement results, but rather a result of considering different ranges of applied dose-per-pulse.

5.3.3 Validity of the Numerical Model

Using a single value of the recombination coefficient α, the numeric calculation replicates the general shape of the dose-per-pulse dependence of the experimental data quite well, but shows sizable discrepancies in the actual value of the calculated k_s at $U_c = 300$ V and 400 V. In principle, this could be an inaccuracy in the numerical approximation warranting an extended analysis.

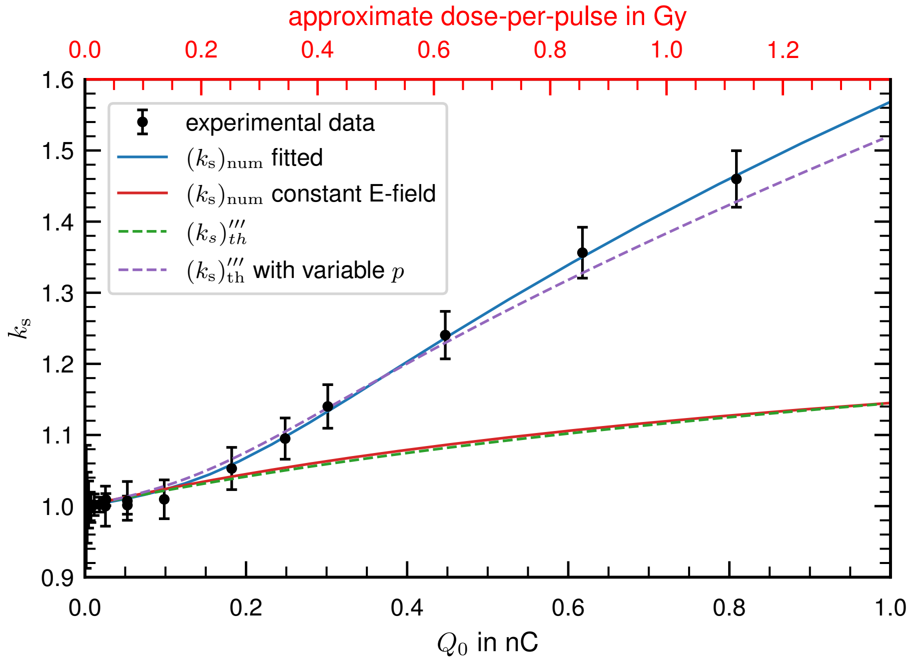

Figure 5.7: Variations of the numerical calculation of k_s for the Advanced Markus chamber at $U_\mathrm{c} =$ 300 V. A calculation with a fixed electric field strength is compared to $(k_\mathrm{s})'''_\mathrm{th}$. In addition, a least squares fit of $(k_\mathrm{s})_\mathrm{num}$ resulting in a different value of α is shown together with the experimental data that was fitted. As a final comparison a calculation using $(k_\mathrm{s})'''_\mathrm{th}$ with values of p depending on the liberated charge is shown.

Fixing the electric field strength in the numerical calculation renders the inclusion of variable electron mobility and attachment in the numerical calculation moot, resulting in a problem virtually identical to the one considered by Boag et al. (1996). Therefore, it is instructive to compare such a calculation to Boag et al.'s (1996) best approximation ($(k_\mathrm{s})'''_\mathrm{th}$ from eq. (2.12)). This comparison is shown in Fig. 5.7 as red and dashed green lines. The remaining difference between the numerical approach and the derivation of $(k_\mathrm{s})'''_\mathrm{th}$ is the treatment of the electron attachment process. It is treated as instantaneous and resulting in a rectangular negative ion concentration in $(k_\mathrm{s})'''_\mathrm{th}$, while its finite duration is considered in the numerical calculation and the resulting ion concentration should be smooth with an asymptotic shape. Despite this rather rough approximation, the two solutions are virtually identical (Fig. 5.7), showing that the numerical calculation is well behaved, at least in this limit of a constant electric field strength.

A further heuristic estimation of the errors of the full numerical calculation can be obtained from a variation of the grid size. Since the errors of the numerical approximation

Table 5.2: The numerically calculated k_s for an Advanced Markus chamber at $U_c = 300\,\text{V}$ and a liberated charge of $Q_0 = 722\,\text{pC}$ ($\sim$ 1.0 Gy) using different spatial discretization cell sizes (h) and two different conditions for the time step (Δt).

h	10^5 nm	10^4 nm	10^3 nm	10^2 nm
$\Delta t = 0.5\frac{h}{max(\lvert v(x)\rvert)}$	1.509 83	1.491 62	1.491 18	1.491 17
$\Delta t = 0.1\frac{h}{max(\lvert v(x)\rvert)}$	1.502 40	1.490 89	1.491 10	1.491 16

scale with the grid size, the changes resulting from its variation are indicative of the overall numerical error. The numerically calculated k_s for different time and space step size combinations is shown in table 5.2.

The table clearly shows a decreasing change of the result with decreasing step size, indicating the convergence of the numerically calculated k_s. All the calculations shown in the results (except for those in table 5.2) were carried out with $h = 100$ nm and $\Delta t = 0.5\frac{h}{max(|v(x)|)}$. Using the observed changes with decreasing step size as a guidepost, a very conservative estimation of the remaining numerical error of 10^{-4} can be made, leaving practically no room for a meaningful improvement of the overall accuracy by reducing the numerical errors. Using a "better" numerical method, specifically one of higher order, could only confer the benefit of achieving the same accuracy at a larger step size, possibly resulting in reduced computation time, at the expense of increasing the implementation complexity. Barring any severe blunders in implementation or choice of the numerical method, such as choosing an unstable method for the system under consideration, the conclusion from this accuracy analysis must be that the numerical solution is an accurate solution of the equation system (2.7).

Therefore, the reason for the discrepancies between $(k_\text{s})_\text{num}$ and the experimental data should be sought in either the input parameters or even the approximations going into the formulation of the original equation system as discussed in the following.

5.3.4 Discussion of the Recombination Rate

The recombination rate constant could not be determined with satisfactory certainty from literature. Therefore, it was determined from a fit of the numerical k_s calculation to the experimental data at $U_\text{c} = 50$ V, while the other determinations were based on independent measurements found in literature. The rather arbitrary choice of which data set to fit to obtain α raises the question how the results would change if the data obtained at any of the

Table 5.3: Values of α obtained from fitting $(k_\mathrm{s})_\mathrm{num}$ to the experimental data and reduced chi-squared of the fit for each collection voltage in the Advanced Markus chamber.

U_c	50 V	100 V	300 V	400 V
α (10^{-12} m^3/s)	1.282	1.236	0.904	0.990
χ^2_ν	0.421	0.613	0.323	0.331

other collection voltages were used to determine α. Figure 5.7 shows the result of fitting the numerical calculation to the data at $U_\mathrm{c} = 300$ V and table 5.3 compares the values of α obtained from fitting each data set and the corresponding reduced chi-squared.

Using an individual α for each collection voltage results in excellent agreement of the numerical calculation with the experimental data. This can be seen in Fig. 5.7 as well as in the χ^2_ν values in table 5.3. A value of $\chi^2_\nu < 1$ actually suggests that the deviation of the data from the fit is smaller than what would be expected from the uncertainties. As the uncertainties include, for instance, an uncertainty in the calibration factor, which systematically affects all measured k_s at a single collection voltage equally, the fit may adjust to some of the variation accounted for in the given uncertainty.

While a variable α contradicts the original assumption that the recombination reaction could be described by a single constant, it is not implausible. The equation system solved by the numerical solution simplifies the various different ions species existing in air to positive and negative ions. While a static mixture of different ion species may be described well by a set of average parameters, the composition of the ions evolves in time. Charge transfer collisions with neutral gas molecules change the relative concentration of the different species and reactions even form new compounds (Kossyi et al., 1992). Such a changing ion composition is one possible explanation for what has also been observed as changes of the recombination rate with “age” of the ions (Marshall, 1929; Ebert et al., 1964; McGowan, 1965). Here the collection voltage directly affects the average time the ions spent in the sensitive volume until they are neutralized at the electrodes (i.e., their average “age”).

The observed trend in α is opposite to the literature, though, where lower values of α are reported for longer time durations (“older” ions). However, all the literature data is for times longer than 1 ms between irradiation and recombination measurements, while the ion collection time in the Advanced Markus chamber is less than 100 µs. Therefore, changes of the ion mixture constituting positive and negative ions could still be responsible for the observed changes in the effective value of α for the entirety of ions.

The measurement at $U_\mathrm{c} = 300\,\mathrm{V}$ stands out, even when allowing for a variation in α. While there appears to be a general trend for lower effective values of α (table 5.3) and less agreement of the fit of $(k_\mathrm{s})'_\mathrm{th}$ with the data (table 5.1), the fitted value of α is lowest and agreement with the fit of $(k_\mathrm{s})'_\mathrm{th}$ is also lowest at $U_\mathrm{c} = 300\,\mathrm{V}$. In this context it should be noted that the measurement at $U_\mathrm{c} = 300\,\mathrm{V}$ was performed on a different day from the other measurements. There could be an uncontrolled change in the experimental conditions, such as a change in air humidity, which could affect any of the ion and electron swarm parameters (McGowan, 1965; Davies and Chantry, 1985; Hochhäuser et al., 1994). Furthermore, the experiments with the LIC and subsequent addition of an online monitoring of the beam position showed that the ELBE may exhibit some instability in the beam position when operated in this pulsed regime. A drift in the beam position could easily skew the measurement by changing the relation between the fraction of the beam irradiating the ionization chamber and being collected by the Faraday cup.

Finally, it should be noted that the variable values of α have to be seen as a general proxy for shortcomings in the input parameters. It was chosen, because its value from literature appeared to be least certain and the effects on $(k_\mathrm{s})_\mathrm{num}$ of changing it are most easily anticipated. For instance, different values of the ion mobilities could probably yield the same effect, but would also entail changes to the pulse duration dependence of $(k_\mathrm{s})_\mathrm{num}$. In general, it can be concluded that the numerical calculation is capable of reproducing qualitatively the dose-per-pulse and pulse duration dependence of k_s, but it needs individual adjustment of the input parameters to obtain exact results.

5.3.5 Relevance of the Free Electron Fraction

Particularly at the high collection voltages in the Advanced Markus chamber, the dose-per-pulse dependence of k_s takes a shape that cannot be reproduced by any of the expressions $(k_\mathrm{s})'_\mathrm{th}$, $(k_\mathrm{s})''_\mathrm{th}$ and $(k_\mathrm{s})'''_\mathrm{th}$ derived by Boag et al. (1996). At the same time the numerical solution reproduces the observed dependence well. The discussion of the validity of the numerical model already touched on the key difference between $(k_\mathrm{s})_\mathrm{num}$ and $(k_\mathrm{s})'''_\mathrm{th}$ (see Fig. 5.7): the shielding of the electrodes by the liberated charges and consequently the feedback of the charge collection on itself.

Mostly responsible for this field distortion are the free electrons. The electron mobility is about three order of magnitude higher than that of the ions; so while they are rapidly

Table 5.4: The fraction of liberated charge (Q_0) collected as free electrons for different values of Q_0 in the Advanced Markus chamber as calculated with the numerical solution at two different collection voltages.

Q_0	1.00 pC	10.0 pC	100 pC	1000 pC
300 V	0.735	0.731	0.683	0.374
100 V	0.313	0.308	0.267	0.188

collected, an almost stationary space charge of positive ions is left behind. This space charge of positive ions subsequently slows down the further collection of free electrons, increasing the time the electrons spend in the sensitive volume and increasing the number of electrons that attach to form negative ions. The higher the amount of charge liberated the higher is the potential distortion, consequently the fraction of charge collected as free electrons is reduced with increasing liberated charge.

The importance of this effect is illustrated in two ways. Table 5.4 lists the fraction of free electrons for the Advanced Markus chamber at two collection voltages and four liberated charge values. At $U_\mathrm{c} = 300\,\mathrm{V}$ the free electron fraction is halved from 0.735 at low dose-per-pulse to 0.374 at the highest dose-per-pulse value. While the relative change in the free electron fraction is similar at $U_\mathrm{c} = 100\,\mathrm{V}$ (reduced to about 60 %), one must also consider what this means for the relative increase in negative ion concentration. At $U_\mathrm{c} = 300\,\mathrm{V}$ the charge fraction converted to negative ions more than doubles from 0.262 to 0.626. Thus, the negative ion concentration is increased doubly, first the overall liberated charge is increased and second an increased fraction of that charge is transformed into negative ions, explaining the super-linear increase in k_s. Consequently, Boag's models cannot replicate the dose-per-pulse dependence of k_s, because such a feedback is not considered therein.

At $U_\mathrm{c} = 100\,\mathrm{V}$ the fraction of charge converted to negative ions is always higher (0.687 at the lowest dose-per-pulse). Consequently, the fraction of negative ions increases by less than 20 % to 0.812. While this is apparently not high enough to spark a super-linear increase in k_s, it is still sufficient to cause an increasing underestimation of k_s with increasing dose-per-pulse by a purely calculated $(k_\mathrm{s})_\mathrm{th}'''$, as seen in Fig. 5.4.

Another demonstration of the relevance of the free electron fraction is achieved by using the value of $p(Q_0)$ as calculated with the numerical solution and inserting it into $(k_\mathrm{s})_\mathrm{th}'''$. The result of this semi-analytical solution is shown in Fig. 5.7 (purple dashed line) and it is fairly close to the full numerical calculation. While some differences remain, due to the effect

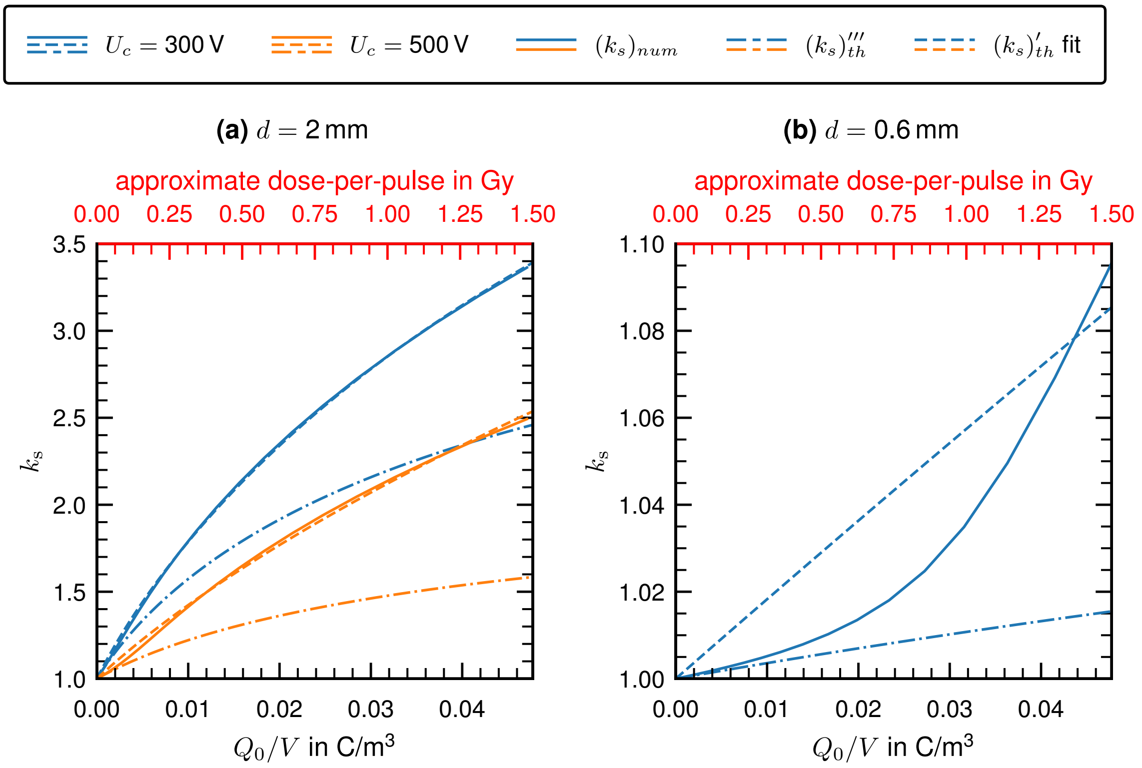

(a) $d = 2\,\mathrm{mm}$ **(b)** $d = 0.6\,\mathrm{mm}$

Figure 5.8: Numerically calculated k_s values for two electrode distances compared to fits of those values with $(k_\mathrm{s})'_\mathrm{th}$ and a calculation using $(k_\mathrm{s})'''_\mathrm{th}$. The lateral dimensions and absolute volume of the chamber are irrelevant to this calculation, due to the reduction of the problem to one dimension. To reflect this fact, the x-axis is given in liberated charge per volume (Q_0/V). The approximate dose-per-pulse was calculated using calibration factors $N_\mathrm{w}(2\,\mathrm{mm}) = 8.33 \cdot 10^7$ Gy/C and $N_\mathrm{w}(0.6\,\mathrm{mm}) = 5.0 \cdot 10^8$ Gy/C, derived from the nominal responses of Roos (PTW, 2016) and PPC05 (CNMC, 2017) chambers.

of the field distortion on the ion collection and the rather irregularly shaped negative ion distribution, it nicely highlights the dominant role of the free electron fraction in the dose-per-pulse dependence of k_s at such high collection voltages.

Building on this realization it is possible to generalize under which conditions the dose-per-pulse dependence may be described by a fit of $(k_\mathrm{s})'_\mathrm{th}$ or when a numerical calculation is more appropriate. Fitting $(k_\mathrm{s})'_\mathrm{th}$ will fail, whenever the fraction of free electrons is large, that is in particular for a chamber with small electrode separation.

As far as commercially available plane-parallel chambers for radiation therapy are concerned one can find, in addition to the 1 mm electrode distance in the Advanced Markus chamber, two other common electrode separations: 2 mm and 0.6 mm. 2 mm is the separation in the Bragg Peak and Roos chambers from PTW and the NACP and PPC40 chambers from IBA dosimetry (formerly Scanditronix-Wellhöfer), while 0.6 mm is the separation in the PPC05 chamber from IBA dosimetry. A numerical calculation was carried out for both of these separations at the maximum recommended collection voltages for the mentioned chambers. Those are 300 V for Roos, NACP, PPC40 and PPC05 chambers and 500 V for the Bragg Peak chamber. In Fig. 5.8 the resulting $(k_\mathrm{s})_\mathrm{num}$ is compared to a calculation of $(k_\mathrm{s})'''_\mathrm{th}$ using the same input parameters and a fit of $(k_\mathrm{s})'_\mathrm{th}$ to the $(k_\mathrm{s})_\mathrm{num}$ data is also attempted. The figure mirrors the conclusions made above: For the lowest collection voltage and largest electrode spacing the fit of $(k_\mathrm{s})'_\mathrm{th}$ works well as a model of the dose-per-pulse dependence. At $U_\mathrm{c} = 500$ V and $d = 2$ mm some discrepancies show, but the fit is probably still acceptable. Finally, for the smallest spacing the fit is pretty much useless. In all cases the pure calculation using Boag et al.'s (1996) expression underestimates k_s because changing p is not taken into account. Fitting this expression to the data masks this effect to some extent, but only if it is sufficiently weak.

5.4 Advanced Markus Chamber in N$_2$

5.4.1 Experimental and Calculation Results

Figure 5.9 shows experimentally determined k_s values for the Advanced Markus chamber in an N$_2$ atmosphere at a pulse duration of $t_\mathrm{pulse} = 3.773$ µs. For comparison also measurements using the same setup of the ionization chamber inside a vacuum chamber, with a regular air atmosphere are shown as well. Those measurements were acquired once before exchanging air with N$_2$ (air filling) and once again after releasing the N$_2$ and re-venting the vacuum chamber with air (air refill).

Below a value of $Q_0 = 50$ pC k_s is close to 1 for the N$_2$ filling, while it increases from unity to a value of 1.1 for the air filling. However, beyond that liberated charge value k_s quickly increases for the N$_2$ filling, leading to almost identical k_s values for $Q_0 > 150$ pC.

Three different numerical calculations were performed to analyze possible causes for this behavior. One calculation introduces an additional reaction term for an electron-ion recombination and this reaction rate constant β was left as a fit parameter. The other two calculations assume the same reactions as in the previous models for air, but fit the attachment rate γ in one case and both γ and recombination rate α in the other case to the experimental data. Introducing an electron-ion recombination with a value of $\beta = 4.45 \cdot 10^{-12}$ m^3/s

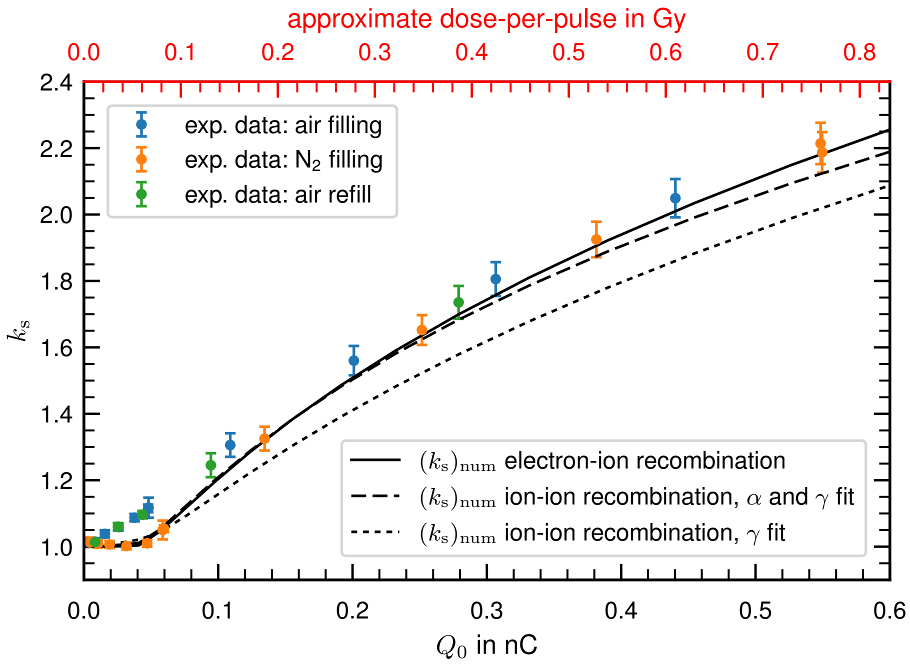

Figure 5.9: Comparison of the dose-per-pulse dependence of k_s in air and N_2 atmospheres using $U_c = 100\,V$ with an Advanced Markus chamber. Additionally, three approaches to the numerical calculation of k_s in the N_2 atmosphere are shown.

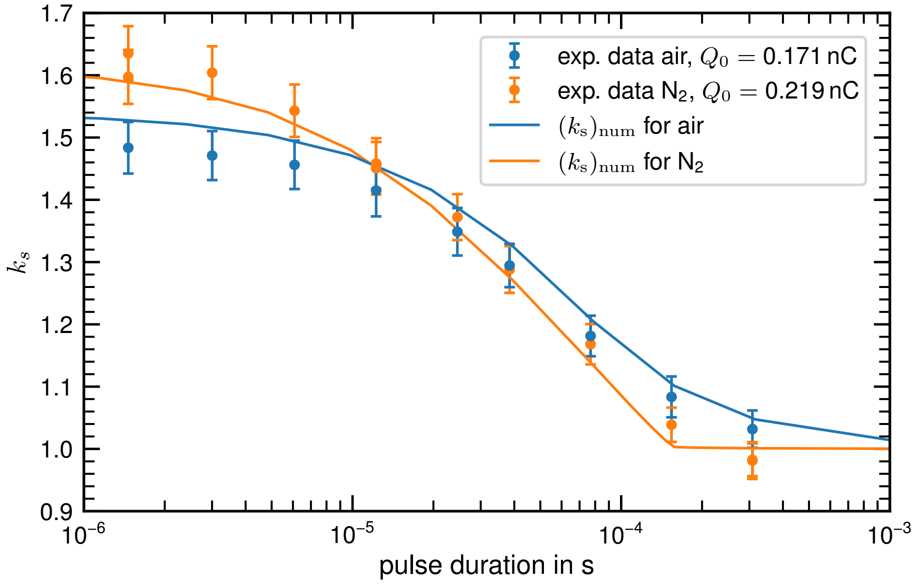

Figure 5.10: Comparison the pulse duration dependence of k_s in air and N_2 atmospheres in an Advanced Markus chamber. Experimental data and numerical calculation results are shown.

Table 5.5: Numerically calculated k_s for $U_c = 300\,\mathrm{V}$ in the Advanced Markus chamber at different liberated charge values, with and without electron-ion recombination.

	Q_0	1.00 pC	10.0 pC	100 pC	1000 pC
$(k_\mathrm{s})_\mathrm{num}$	*with electron-ion*	1.000 27	1.002 74	1.033 86	1.663 25
	only ion-ion	1.000 26	1.002 64	1.032 79	1.658 10

Table 5.6: The electron collection time (τ_electron, defined as the duration from end of irradiation until the reduction of the total electron charge in the sensitive volume to $10^{-7}Q_0$) as determined in the numerical k_s calculation for $U_c = 100\,\mathrm{V}$ in the Advanced Markus chamber for air and N_2.

	Q_0	1.00 pC	10.0 pC	100 pC	1000 pC
τ_electron	N_2	0.1090 µs	0.1110 µs	14.4225 µs	20.9491 µs
	air	0.0603 µs	0.0603 µs	0.0604 µs	0.0643 µs

shows the best agreement with the experimental data, with a reduced chi-squared of $\chi^2_\nu = 0.94$. Adjusting only the attachment rate yielded a value of $\gamma = 2.08 \cdot 10^{-3}\,\mathrm{ns}^{-1}$ and $\chi^2_\nu = 16.0$, while also adjusting the ion recombination rate yielded $\alpha = 3.00 \cdot 10^{-12}\,\mathrm{m}^3/\mathrm{s}$ and $\gamma = 4.44 \cdot 10^{-4}\,\mathrm{ns}^{-1}$ with $\chi^2_\nu = 3.23$.

Figure 5.10 shows another comparison of N_2 and air atmospheres but for different pulse duration values at a fixed dose-per-pulse, instead of a variable dose-per-pulse. The observed reduction in k_s is faster for the N_2 atmosphere than for the air atmosphere, which is well reproduced in the numerical calculation, which uses the best fitting approach from the dose-per-pulse variation: introducing an electron-ion recombination.

5.4.2 Discussion of the Electron-Ion Recombination

The best reproduction of the experimental data for the Advanced Markus chamber filled with N_2 was achieved by adding an electron-ion recombination reaction to the numerical calculation. Furthermore, the pulse duration dependent measurements of k_s in N_2 were well reproduced using this electron-ion recombination, reaffirming the conclusion that it is the main cause for the observed k_s in the N_2 atmosphere.

However, if positive ions and electrons recombine with a non-negligible recombination rate in N_2, a similar mechanism should exist in air as well. To evaluate the effect of including this reaction, the calculations for air were repeated including this reaction, using the reaction rate constant determined in N_2. Table 5.5 shows a comparison of the k_s values in the Advanced Markus chamber with air, with and without an electron-ion recombination, at

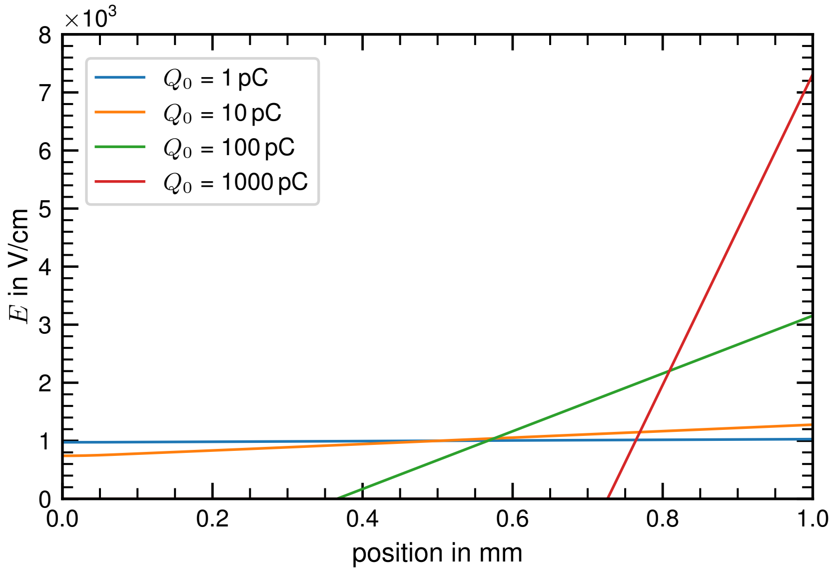

Figure 5.11: Electric field strength in an Advanced Markus chamber in dependence of the position between the electrodes for different value of liberated charge. The anode is at 0 mm and the cathode at 1.0 mm. The values were determined in the numerical k_s calculation and taken at the end of the irradiation with a pulse duration of 3.770 µs.

a value of $U_c = 300$ V and for a few selected values of Q_0. The largest relative difference occurs at the highest dose-per-pulse value, but even there it is small with a value of 0.31 %. Thus, the determined electron-ion recombination rate is in good agreement with the previous findings and not including this effect for calculations regarding air-filled chambers is a good approximation. This is particularly true if fitting the ion-ion recombination rate α, because the adjusted α probably masks most of the theoretical discrepancies introduced by ignoring this minor effect.

Despite its negligible role in air, the electron-ion recombination takes on such a prominent role in N_2 due to a strong distortion of the electric field by the liberated charges. The much higher mobility of the electrons causes their initially rapid collection, while the positive ions hardly move. However, as some electrons are collected the remaining space charge of the positive ions slows the subsequent electron collection, which may increase their collection time dramatically, consequently increasing the probability to recombine with a positive ion. The electron collection time, defined as the time from the end of the irradiation until the time at which the charge of all electrons in the sensitive volume is reduced to $10^{-7}Q_0$, is shown for both air and N_2 for a few liberated charge values in table 5.6. The values were determined in the numerical calculation and clearly show the aforementioned difference between N_2 and air. Additionally, the more charge is liberated in the ionization chamber the stronger is the potential distortion, explaining the increase of the collection time with increasing dose-per-pulse.

Figure 5.11 illustrates this distortion of the electric field by plotting the electric field strength in the N_2-filled ionization chamber at the end of the irradiation for different values of liberated charge. For $Q_0 = 100$ pC the electric field strength in the region from 0 mm to 0.4 mm is reduced to almost 0 and this region of almost perfect shielding expands for $Q_0 = 1000$ pC to over 0.7 mm. This nicely explains the vast increase in electron collection times, as the electrons are effectively only removed from these extremely low field regions once some of the other charge is cleared, which is limited by the ion's drift velocity.

5.5 PinPoint Chamber

5.5.1 Results and Discussion

Figure 5.12 shows the measured k_s for a PinPoint chamber in dependence of the dose-per-pulse using a fixed pulse duration of $t_\mathrm{pulse} = 3.773$ µs. Mirroring the comparisons in the case of the Advanced Markus chamber, the measured data are compared to a fit of Boag's $(k_\mathrm{s})'_\mathrm{th}$ and the numerical calculation using the value of $\alpha = 1.282 \cdot 10^{-12}$ m^3/s determined in the Advanced Markus chamber measurements. In addition, due to the results of the Advanced Markus chamber analysis (section 5.3.4), $(k_\mathrm{s})_\mathrm{num}$ was fitted to the data using individual α values for each value of U_c. Table 5.7 lists the parameters obtained from both fits, for $(k_\mathrm{s})'_\mathrm{th}$ as well as for $(k_\mathrm{s})_\mathrm{num}$.

The general shape of the dose-per-pulse dependence of k_s is reproduced fairly well by both $(k_\mathrm{s})_\mathrm{num}$ and $(k_\mathrm{s})'_\mathrm{th}$. While this is in contrast to the observations made for the Advanced Markus chamber (where $(k_\mathrm{s})'_\mathrm{th}$ failed to adequately describe this dependence at higher collection voltages), it is a direct consequence of the relatively large electrode separation of 2 mm in the PinPoint chamber. The dose-per-pulse dependence of k_s in the Advanced Markus chamber is a result of substantial changes in the fraction of charge collected as free electrons. If this fraction is small $(k_\mathrm{s})'_\mathrm{th}$ can give a good description of the dose-per-pulse dependence of k_s. This is the case for large electrode separations in plane-parallel chambers (section 5.3.5). The same principle should apply to thimble chambers and apparently 2 mm electrode separation results in a fairly low free electron fraction here as well.

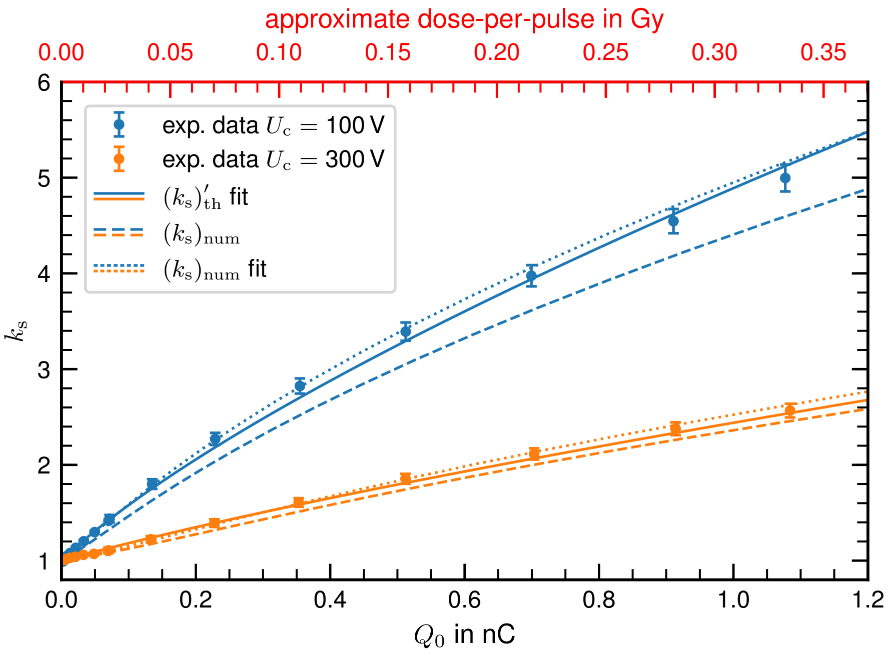

Figure 5.12: k_s measured for a PinPoint chamber in dependence of the dose-per-pulse at pulse duration of $t_{pulse} = 3.773\,\mu s$. The measured data are compared to a fit of $(k_s)'_{th}$ and a numerical calculation using the same parameters as for the Advanced Markus chamber with air.

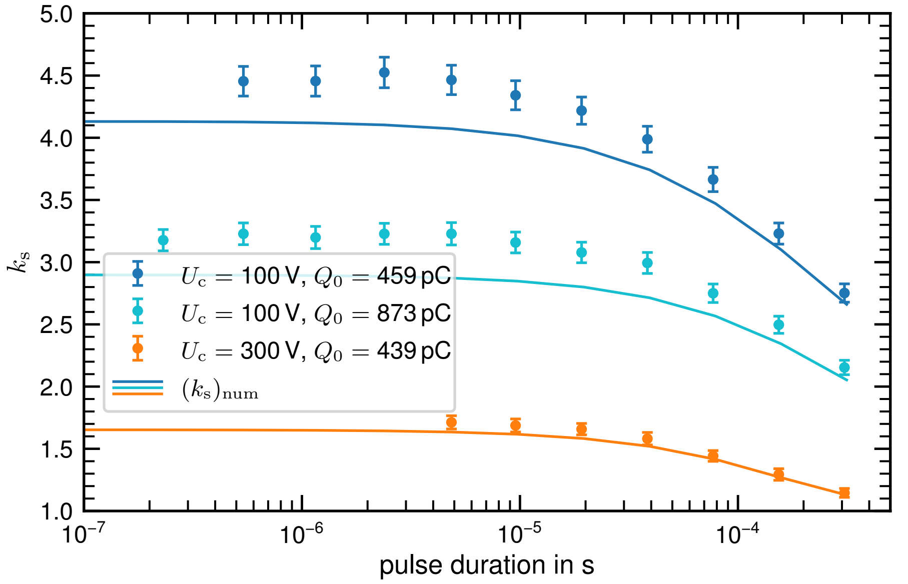

Figure 5.13: Measured k_s for the PinPoint chamber in dependence of the pulse duration. The experimental data are compared to corresponding numerical calculations.

Table 5.7: The parameters obtained from fitting $(k_\mathrm{s})'_\mathrm{th}$ and $(k_\mathrm{s})_\mathrm{num}$ to the experimental k_s values of the PinPoint chamber, along with the reduced chi-squared (χ^2_ν) calculated for each fit.

U_c		100 V	300 V
$(k_\mathrm{s})'_\mathrm{th}$	a (nC^{-1})	13.89 ± 0.25	3.86 ± 0.05
	p	$(2.1 \pm 0.7) \cdot 10^{-2}$	$(6.1 \pm 3.4) \cdot 10^{-5}$
	χ^2_ν	4.2	3.8
$(k_\mathrm{s})_\mathrm{num}$	α (10^{-12} m^3 s^{-1})	1.767	1.619
	χ^2_ν	2.396	2.133

Regarding the reproduction of the experimental data, both fits ($(k_\mathrm{s})'_\mathrm{th}$ as well as $(k_\mathrm{s})_\mathrm{num}$) are closer than the $(k_\mathrm{s})_\mathrm{num}$ calculation using a fixed α value determined from the Advanced Markus chamber measurements. Using a fixed value of α, the $(k_\mathrm{s})_\mathrm{num}$ underestimates the measured k_s, in particular at $U_\mathrm{c} = 100$ V. Considering only the plots, both fits may appear equally good, but fitting $(k_\mathrm{s})_\mathrm{num}$ results in reduced chi-squared of about half the size of that resultant from fitting $(k_\mathrm{s})'_\mathrm{th}$. Therefore, even though the dose-per-pulse dependence does not reveal any obvious deviations from the shape predicted by $(k_\mathrm{s})'_\mathrm{th}$, $(k_\mathrm{s})_\mathrm{num}$ still allows a better description of the experimental data.

Nevertheless, the agreement between the fit of $(k_\mathrm{s})_\mathrm{num}$ and experimental data is not as good in the PinPoint chamber as it is in the Advanced Markus chamber ($\chi^2_\nu > 2$ for both values of U_c in the PinPoint chamber and $\chi^2_\nu < 1$ in the Advanced Markus chamber). A possible explanation for the mismatch between numerical fit and experimental data is an overly simplified geometry assumption for the PinPoint chamber. About half of the thimble chamber's volume is close to spherical in geometry, while the other half is cylindrical. For the numerical calculation the entire volume was assumed to have cylindrical geometry, which could quite possibly affect the calculated $(k_\mathrm{s})_\mathrm{num}$, in particular at the high dose-per-pulse end, where the effect of the liberated charges on the electric field is more pronounced and where $(k_\mathrm{s})_\mathrm{num}$ differs most from the experimental data.

Another difference to the Advanced Markus chamber is observed in the fitted α values. They are both higher than those observed in the Advanced Markus chamber. In the discussion of the recombination rate of the Advanced Markus chamber it was suggested that the variable value of α may result from changes in composition of the ion swarm and be related to the ion collection time. The trend within the PinPoint chamber is the same as for the Advanced Markus chamber, higher values of U_c result in higher effective values for

α, however, the values in the PinPoint chamber should be closer to the Advanced Markus chamber values. Roughly, the ion collection time should be proportional to $\frac{d^2}{U_\mathrm{c}}$, with the distance between the electrodes d, which is $d_{\mathrm{Adv.\,Markus}} = 1\,\mathrm{mm}$ and $d_{\mathrm{PinPoint}} = 2\,\mathrm{mm}$. Thus, ion collection time at $U_\mathrm{c} = 300\,\mathrm{V}$ in the PinPoint chamber should be in between the time in the Advanced Markus chamber at $U_\mathrm{c} = 50\,\mathrm{V}$ and $U_\mathrm{c} = 100\,\mathrm{V}$. So in principle the pre-determined value of $\alpha = 1.282 \cdot 10^{-12}\,\mathrm{m^3/s}$ should have been a decent match for the PinPoint chamber at $U_\mathrm{c} = 300\,\mathrm{V}$.

These higher than expected effective α values could also be a result of an oversimplified geometry in the numerical calculation or they could indicate that α in this context is not only dependent on the ion collection time. Yet, resolving this question would require further, non trivial refinement of the numerical method to consider the thimble geometry more completely or additional experiments to obtain more data for different electrode separations and collection voltages.

Finally, Fig. 5.13 shows pulse duration dependent measurements of k_s for the PinPoint chamber together with numerically calculated values using the α value determined from the Advanced Markus chamber measurement. Very similarly to the observations for the Advanced Markus chamber, k_s falls off exponentially with increasing pulse duration, which is in principle well reproduced by $(k_\mathrm{s})_\mathrm{num}$. The calculation is subject to the same underestimation of k_s as observed in the dose-per-pulse dependent data, though. Still, the good reproduction of the falloff supports the general applicability of the numerical model here.

5.6 Liquid Ionization Chamber

5.6.1 Experimental and Calculation Results

Dose-per-pulse dependent measurements of two LICs are compared in Fig. 5.14 to a numerical calculation using mobility and recombination rate values reported by Johansson and Wickman (1997). In addition, two calculations using Boag's original expression $(k_\mathrm{s})_\mathrm{th}$ (eq. (2.8)) were performed. One uses the same parameters as the numerical calculation and the other is a fit adjusting a. Table 5.8 compares the calculated and fitted values of a. In both chambers the k_s calculated using literature values overestimates k_s, with the numerical solution doing slightly more so than the analytical approach. At the same time, the fit matches the experimental data closely in both chambers.

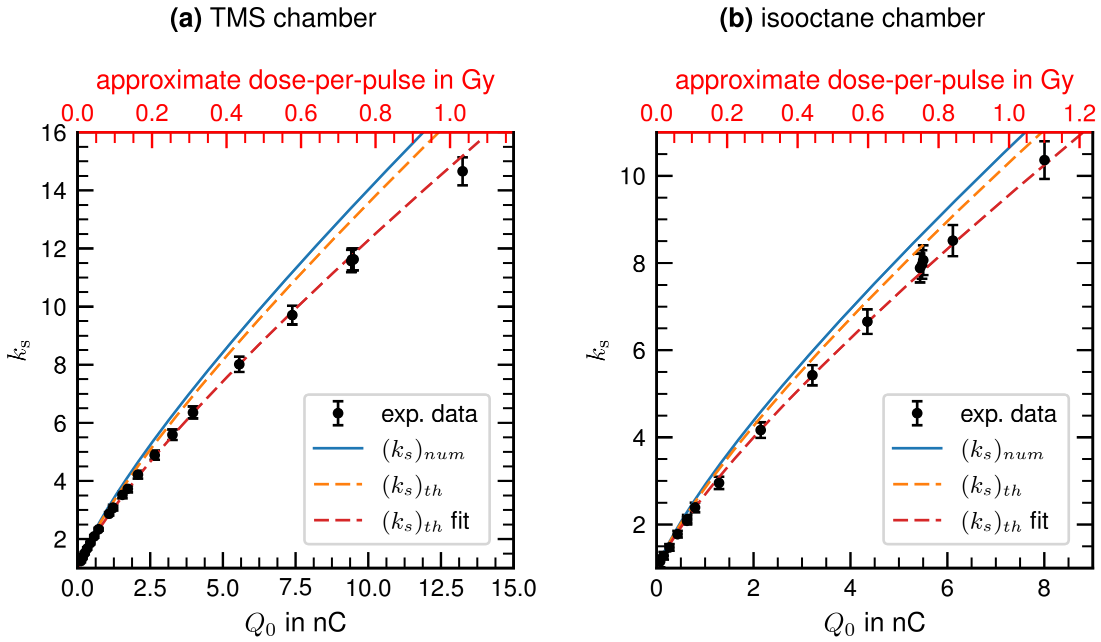

Figure 5.14: Dose-per-pulse dependent k_s measurements with two LICs. The measurements are compared to calculated values from the numerical solution, Boag's (1950) $(k_\mathrm{s})_\mathrm{th}$ (eq. (2.8)) and a least-squares fit of $(k_\mathrm{s})_\mathrm{th}$ adjusting a.

Table 5.8: Calculated and fitted values of a for the curves shown in Fig. 5.14 as well as the reduced chi-squared of the fit.

	$a_\mathrm{calculated}$	a_fit	χ^2_ν
TMS	5.45 nC^{-1}	4.80 ± 0.02 nC^{-1}	0.75
isooctane	5.18 nC^{-1}	4.68 ± 0.04 nC^{-1}	1.01

Pulse duration dependent measurements performed with the same chambers are shown in Fig. 5.15 and are also compared to numerical calculations using the literature values from Johansson and Wickman (1997).

In order to analyze the prominent dip in k_s at 693 ns, further measurements were performed using the isooctane chamber adding a scintillator screen in front of the LIC. This scintillator provided an online position measurement of the beam spot but also broadened the beam spot due tot the additional scattering. In addition, the amplifier of the Faraday cup was modified to allow longer pulse durations to be measured. The results of this follow up measurement are shown in Fig. 5.16 together with numerically calculated k_s values.

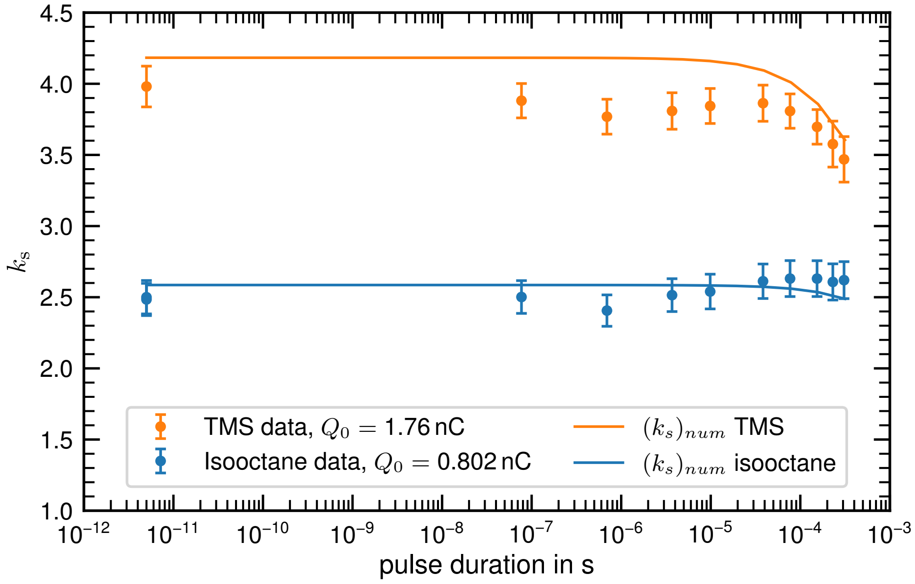

Figure 5.15: Pulse duration dependent measurements of k_s in an isooctane and TMS filled chamber. The shown $(k_\mathrm{s})_\mathrm{num}$ is based on the literature values from Johansson and Wickman (1997).

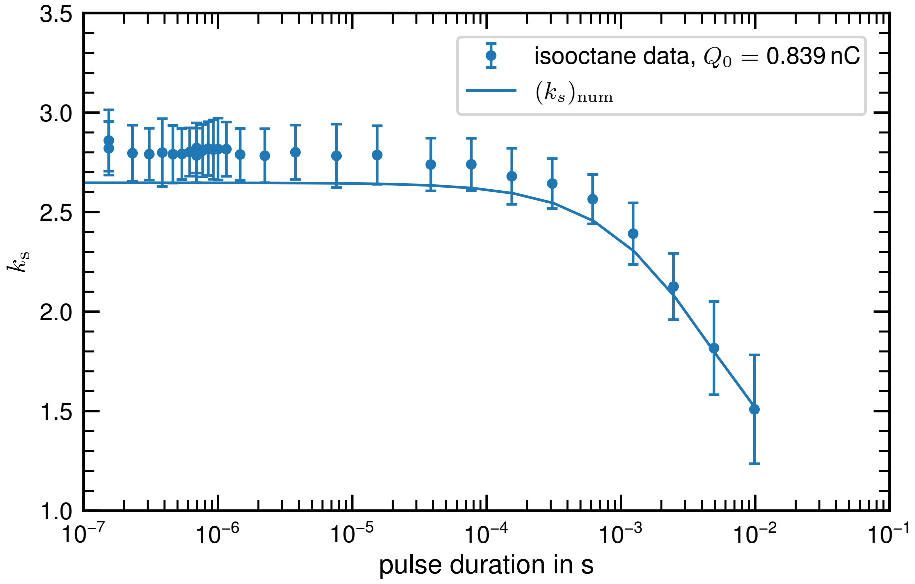

Figure 5.16: Repeated pulse duration dependent measurements of k_s of the isooctane filled chamber, extending to longer pulse durations and with an additional scintillator in front of the LIC.

5.6.2 Discussion

In contrast to the air filled chambers, shielding of the electrodes appears to be a minor effect in both LICs, judging from the good agreement of the experimental data with Boag's (1950) original expression. Despite the high ionization densities occurring in these chambers, which are about 100 times the value observed in the Advanced Markus chamber, the consideration of two charge carrier species and a constant electric field strength in this expression appear to be sufficient. Without a fast charge carrier, like the free electrons in gases, distortions of the electric field due the liberated charges remain minor, and ignoring those changes remains a very good approximation (Boag, 1950; Boag et al., 1996). The discrepancies between the measured k_s and that calculated from literature values seen in Fig. 5.14 could be due to differences in the exact composition of the liquid used. Minor impurities may have a large effect on the mobility and recombination rates in these media (Johansson and Wickman, 1997; Pardo-Montero et al., 2012). On the other hand this discrepancy could also be a result of the calculation of the experimental k_s. The determination of the Faraday cup's calibration factor, which determines the liberated charge and ultimately k_s, relies on a linear relationship between liberated charge and k_s at low values of liberated charge. However, for the LICs even the lowest value measured was $k_\mathrm{s} = 1.1$ and using just the three lowest values for the extrapolation meant including values up to $k_\mathrm{s} = 1.5$. It is conceivable that this has lead to an error that is not considered in the uncertainties discussed above.

Furthermore, the pulse duration variation showed a peculiar feature for both LICs: a drop in k_s at a setting of 10 bunches per pulse corresponding to $t_\mathrm{pulse} = 693\,\mathrm{ns}$. However, the addition of a scintillator screen to monitor the beam position for each radiation pulse eventually caused the feature to disappear. Those scintillator measurements showed a variation of the beam position with changing pulse duration.

Such changes in the beam position are relevant because only a fraction of the inhomogeneous beam profile is irradiating the chamber's sensitive volume, while the entire beam is collected by the Faraday cup. With the changes in the alignment, the fraction of the beam that irradiated the chamber changed, essentially altering the calibration factor relating Faraday cup measurement to liberated charge. Since alignment of the beam was performed using 10 bunches per pulse, the beam's most intense part struck the ionization chamber in this setting, liberating a certain amount of charge and inducing a certain Faraday cup measurement. For all other pulse durations, alignment was not perfect and at the same Faraday cup value a lower amount of charge was liberated in the chamber. This lead to a lower collected charge and the determination of a higher k_s.

This movement of the beam spot in combination with the small dimensions of the LIC probably caused the apparent dip in k_s. The feature disappeared when the scintillator block was introduced, because this block served as a scatterer, homogenizing the beam spot sufficiently to liberate the same amount of charge independent of these variations in the beam's position.

Disregarding the sudden dip, the numerical calculation reproduces the pulse duration dependence of k_s in both liquids well, showing the flexibility of the numerical approach to cover a wide range of parameter values. Beyond the calculation of k_s for longer pulses, however, the numerical approach offers little advantage over the existing approximations for the liquid filled chambers. This is due to the absence of a fast charge carrier in these liquids, like the free electrons in air, which are largely responsible for unexpected behavior at high dose-per-pulse.

5.7 Conclusion and Outlook

The existing models for volume recombination in the form of $(k_\mathrm{s})_\mathrm{th}$, $(k_\mathrm{s})'_\mathrm{th}$, $(k_\mathrm{s})''_\mathrm{th}$ or $(k_\mathrm{s})'''_\mathrm{th}$ are only truly suitable for high dose-per-pulse values in active media without fast charge carriers, such as the investigated non-polar liquids TMS and isooctane.

Using effective parameters for the free electron fraction p and combined chamber geometry and medium properties a, it is possible to use, for instance, $(k_\mathrm{s})'_\mathrm{th}$ to describe the dose-per-pulse dependence over a wider dose-per-pulse range in media with a fast charge carrier such as the free electrons in air, with two limitations, however. The parameters take non-physical values and even their dependence on, for example, collection voltage, is contrary to expectations. In addition, this approach reaches its limit for chambers of small electrode spacing and large collection voltage, such as the Advanced Markus chamber at $U_\mathrm{c} = 300\,\mathrm{V}$.

The developed numerical calculation provides a more consistent approach without such limitations. It describes volume recombination in all the investigated chambers, requiring only small adjustments of the recombination rate coefficient. In addition to air, it was also applicable in the very different media of nitrogen, TMS and isooctane and also to arbitrary pulse durations. Furthermore, in contrast to the existing models, the numerical calculation allowed for arbitrary pulse duration and replicated dependence of volume recombination on pulse duration well.

Due to the required adjustments of the recombination rate coefficient α, however, it is not possible to calculate volume recombination *ab initio*. Instead a measurement with a chamber at the desired collection voltage U_c at different known dose-per-pulse values is required to determine the exact recombination rate coefficient.

Future work should aim to improve the description of the dependence of volume recombination on U_c, possibly by determining a function $\alpha(U_\mathrm{c})$. Such knowledge could eliminate the need to adjust α individually for each chamber and collection voltage which requires reference measurements using variable dose-per-pulse. As a result, k_s could be derived from a variation of U_c in a manner similar to Jaffé plots, greatly simplifying the required procedures.

Yet, even without such knowledge the numerical solution allows a very accurate description of the dose-per-pulse dependence of volume recombination in ionization chambers. Thereby it improves on the existing models, which failed at high dose-per-pulse, and allows the principal application of ionization chambers in highly pulsed fields.

6 Summary

Synchrocyclotrons and laser based particle accelerators, developed with the goal to enable more compact particle therapy facilities, may bring highly pulsed radiation field to external beam radiation therapy. In addition, such highly pulsed fields may be desirable due to their potential clinical benefits regarding better healthy tissue sparing or improved gating for moving tumors. However, they pose new challenges for dosimetry, the corner stone of any application of ionizing radiation.

These challenges affect both clinical and radiation protection dosimetry. Air-filled ionization chambers, which dominate clinical dosimetry, face the problem of increased signal loss due to volume recombination when a highly pulsed field liberates a large amount of charge in a short time in the chamber. While well established descriptions exist for this volume recombination for the moderately pulsed fields in current use (Boag's formulas), the assumptions on which those descriptions are based will most likely not hold in the prospective, highly pulsed fields of future accelerators. Furthermore, ambient dose rate meters used in radiation protection dosimetry as survey meters or fixed installations are generally only tested for continuous fields, casting doubt on their suitability to measure pulsed fields.

This thesis investigated both these aspects of dosimetry – clinical as well as radiation protection – to enable the medical application of highly pulsed radiation fields. For a comprehensive understanding, experimental investigations were coupled with theoretical considerations and developments.

Pulsed fields, varying in both dose-per-pulse and pulse duration over a wide range, were generated with the ELBE research accelerator, providing a 20 MeV pulsed electron beam. Ionization chambers for clinical dosimetry were investigated using this electron beam directly, with an aluminium Faraday cup providing the reference measurement. Whereas the dose rate meters were irradiated in the photon field generated from stopping the electron beam in the Faraday cup. In those measurements, the reference was calculated from the ionization chamber, then serving a an electron beam monitor, cross-calibrated to the photon field with thermoluminescent dosimeters.

Three dose rate meters based on different operating principles were investigated, covering a large portion of the operating principles used in radiation protection: the ionization chamber based RamION, the proportional counter LB 1236-H10 and the scintillation detector AD-b. Regarding clinical dosimetry, measurements of two prominent ionization chamber geometries, plane-parallel (Advanced Markus chamber) and thimble type (PinPoint chamber), were performed. In addition to common air-filled chambers, chambers filled with pure nitrogen and two non-polar liquids, tetramethylsilane and isooctane, were investigated.

In conjunction with the experiments, a numerical solution of the charge liberation, transport, and recombination processes in the ionization chamber was developed to calculate the volume recombination independent of the assumptions necessary to derive Boag's formulas. Most importantly, the influence of the liberated charges in the ionization chamber on the electric field, which is neglected in Boag's formulas, is included in the developed calculation.

Out of the three investigated dose rate meters only the RamION could be identified as an instrument truly capable of measuring a pulsed field. The AD-b performed below expectations (principally, a scintillator is not limited in detecting pulsed radiation), which was attributed to the signal processing, emphasizing the problem of a typical black-box signal processing in commercial instruments. The LB 1236-H10, on the other hand, performed as expected of a counting detector. While this supports the recent effort to formalize these expectations and standardize testing for counting dosimeters in DIN IEC/TS 62743, it also highlights the insufficiency of counting detectors for highly pulsed fields in general and shows the need for additional normative work to establish requirements for dose rate meters not based on a counting signal (such as the RamION), for which no framework currently exists. With these results recognized by the German radiation protection commission (SSK) the first steps towards such a framework are taken.

The investigation of the ionization chambers used in radiation therapy showed severe discrepancies between Boag's formulas and the experimentally observed volume recombination. Boag's formulas describe volume recombination truly correctly only in the two liquid-filled chambers. All the gas-filled chambers required the use of effective parameters, resulting in values for those parameters with little to no relation to their original meaning. Even this approach, however, failed in the case of the Advanced Markus chamber for collection voltages $\geq 300\,\mathrm{V}$ and beyond a dose-per-pulse of about 100 mGy.

The developed numerical model enabled a much better calculation of volume recombination and allowed the identification of the root of the differences to Boag's formulas as the influence of the liberated charges on the electric field. Increased positive space charge due to increased dose-per-pulse slows the collection and reduces the fraction of fast, free electrons, which are unaffected by volume recombination. The resultant increase in the fraction of charge undergoing volume recombination, in addition to the increase in the total amount of charge, results in an increase in volume recombination with dose-per-pulse that is impossible to describe with Boag's formulas. It is particularly relevant in the case of high electric fields and small electrode distances, where the free electron fraction is large. In addition, the numerical calculation allows for arbitrary pulse durations, while Boag's formulas apply only to very short pulses.

In general, the numerical calculation worked well for plane-parallel chambers, including those filled with the very diverse media of liquids, nitrogen and air. Despite its increased complexity, the thimble geometry could be implemented as well, although, in the case of the PinPoint chamber, some discrepancies to the experimental data remained, probably due to the required geometrical approximations.

A possible future development of the numerical calculation would be an improved description of the voltage dependence of the volume recombination. At the moment it requires characterizing a chamber at each desired collection voltage, which could be eliminated by an improved modeling of the volume recombination's dependence on collection voltage. Nevertheless, the developed numerical calculation presents a marked improvement over Boag's formulas to describe the dose-per-pulse dependence and pulse duration dependence of volume recombination in ionization chambers, in principle enabling the application of ionization chambers in the absolute dosimetry of highly pulsed fields.

7 Zusammenfassung

Durch die Einführung von Synchrozyklotronen und Laser-Teilchenbeschleunigern, entwickelt mit dem Ziel günstigere und kompaktere Protonentherapieanlagen bereitzustellen, werden stark gepulste Strahlenfelder möglicherweise Anwendung in der Teletherapie finden. Darüber hinaus bergen stark gepulste Strahlenfelder das Potential klinischer Vorteile durch eine bessere Schonung gesunden Gewebes oder die verbesserte Behandlung bewegter Tumore. Allerdings ergeben sich neue Herausforderungen im Bereich der Dosimetrie, der Grundlage für eine präzise therapeutische Anwendung ionisierender Strahlung.

Diese Herausforderungen betreffen sowohl den Bereich der klinischen Dosimetrie für die unmittelbare Strahlenanwendung als auch die Strahlenschutzdosimetrie zum Schutz von Umwelt und Personal. Luftgefüllte Ionisationskammern, die primären Messinstrumente der klinischen Dosimetrie, sind von einem zunehmenden Signalverlust aufgrund von Volumenrekombination betroffen, da stark gepulste Strahlenfelder eine hohe Ionisationsdichte innerhalb eines sehr kurzen Zeitraums erzeugen. Beschreibungen für diese Effekte sind zwar gut etabliert für die moderat gepulsten Felder im gegenwärtigen klinischen Einsatz (Boags Theorie), allerdings sind die dafür nötigen Näherung höchst wahrscheinlich unzureichend für die stark gepulsten Strahlenfelder zukünftiger Beschleuniger. Ferner sind Dosisleistungsmessgeräte, welche im Strahlenschutz als fest installierte oder mobile Überwachungsdosimeter eingesetzt werden, nur für kontinuierliche Strahlenfelder geprüft und bauartzugelassen, was Zweifel an ihrer Eignung für die Messung gepulster Felder eröffnet.

In dieser Arbeit wurden beide Bereiche der Dosimetrie, sowohl Strahlenschutz als auch klinische Dosimetrie, untersucht, um die medizinische Anwendung stark gepulster Strahlung zu ermöglichen. Für ein möglichst umfassendes Verständnis wurden dabei experimentelle Untersuchungen mit theoretischen Überlegungen und Entwicklungen verzahnt.

Mit dem ELBE-Forschungsbeschleuniger wurde ein gepulster 20 MeV Elektronenstrahl und somit ein gepulstes Strahlungsfeld erzeugt, welches eine systematische Untersuchung in einem großen Bereich in Bezug auf Pulsdosis und Pulsdauer erlaubte. Ionisationskammern für den klinischen Einsatz wurden mit diesem Elektronenstrahl direkt bestrahlt und ein Faraday-Becher diente als unabhängige Referenzmessung. Dosisleistungsmessgeräte hingegen wurden im, durch den Elektronenstrahl im Faraday-Becher erzeugten, Bremsstrahlungsfeld bestrahlt. Dabei fungierte die Ionisationskammer vor dem Faraday-Becher als Strahlmonitor und diente zur Bestimmung der Referenzdosis des Bremsstrahlungsfeldes über eine Querkalibrierung mit Thermolumineszenzdosimetern.

Es wurden drei Dosisleistungsmessgeräte basierend auf unterschiedlichen Messprinzipien untersucht, die damit einen großen Teil der im Strahlenschutz eingesetzten Messprinzipien abdecken: Die Ionisationskammer RamION, das Proportionalzählrohr LB 1236-H10 und der Szintillationsdetektor AD-b. Für die klinische Dosimetrie wurden zwei verbreitete Ionisationskammergeometrien untersucht: die Advanced Markus Kammer als Flachkammer und die PinPoint Kammer als Kompaktkammer. Zusätzlich zu der üblichen Luftfüllung wurde außerdem eine Füllung mit reinem Stickstoff und zwei Flüssigionisationskammern mit Isooctan und Tetramethylsilan untersucht.

Ferner wurde eine numerische Berechnung der Volumenrekombination in Ionisationskammern durch die Beschreibung der Prozesse von Ladungsfreisetzung, Ladungstransport und Reaktion entwickelt, um eine Beschreibung zu erhalten, die ohne die für Boags Theorie notwendigen Näherungen auskommt. Insbesondere berücksichtigt diese Berechnung den Einfluss der freigesetzten Ladungen auf das elektrische Feld, der in Boags Theorie vernachlässigt wird.

Von den drei untersuchten Dosisleistungsmessgeräten zeigte nur das RamION Messungen innerhalb der gegebenen Toleranzen in den untersuchten Strahlungsfeldern. Die unerwartet schlechte Präzision des AD-b Szintillationsdetektors, der keinen prinzipiellen Beschränkungen in gepulsten Feldern unterliegen sollte, wurde auf die Signalverarbeitung im Messgerät zurückgeführt, welche das prinzipielle Problem einer unbekannten Signalverarbeitung in kommerziellen Geräten hervorhebt. Das LB 1236-H10 Proportionalzählrohr andererseits maß den Erwartungen entsprechend. Dies unterstützt zwar die in DIN IEC/TS 62743 dargelegten Erwartungen für zählende Dosimeter, zeigt allerdings zugleich die allgemeine Unzulänglichkeit solcher Instrumente für die Messung stark gepulster Felder und demonstriert die Notwendigkeit für weitere normative Bestrebungen, um einheitliche Bedingungen für die Untersuchung nicht-zählender Dosimeter (wie das RamION) zu schaffen. Durch die Aufnahme dieser Ergebnisse in die Literatur der Strahlenschutzkommission wurde hier der Grundstein für eine solche Entwicklung gelegt.

Die Untersuchung der Ionisationskammern für klinische Dosimetrie zeigte z.T. starke Abweichungen zwischen Boags Theorie und experimentellen Beobachtungen. Boags Theorie beschreibt Volumenrekombination hinreichend genau lediglich für die zwei Flüssigionisationskammern. Im Falle sämtlicher gasgefüllter Kammern waren effektive Parameter notwendig, deren Wert kaum einen Zusammenhang mit der ursprünglichen Definition besaß. Doch auch dieser Ansatz versagt jedoch für die Advanced Markus-Kammer bei Sammelspannungen $\geq 300\,\mathrm{V}$ und Pulsdosen ab ca. $100\,\mathrm{mGy}$.

Das entwickelte numerische Berechnungsverfahren lieferte eine deutlich passendere Berechnung der Volumenrekombination und ermöglichte es, die Ursache für die Unterschiede zu Boags Theorie in dem Einfluss der freigesetzten Ladungen auf das elektrische Feld zu identifizieren. Eine aufgrund der erhöhten Pulsdosis erhöhte positive Raumladung verlangsamt die Sammlung der normalerweise schnellen freien Elektronen, welche von Volumenrekombination zunächst unbeeinträchtigt sind. Aufgrund der längeren Verweildauer im Kammervolumen, lagert sich jedoch ein höherer Anteil der Elektronen an und bildet negative Ionen. Der daraus resultierende höhere Anteil an Ladungen die Volumenrekombination ausgesetzt sind, zusätzlich zu der erhöhten Ladungsmenge, bedingt eine Erhöhung der Volumenrekombination mit der Pulsdosis, die sich nicht durch Boags Theorie beschreiben lässt. Insbesondere von Bedeutung ist dieser Effekt bei hohen elektrischen Feldstärken und kleinen Elektrodenabständen, die in einem hohen Anteil freier Elektronen resultieren. Des Weiteren erlaubt das numerische Verfahren die Berechnung für beliebige Pulsdauern, wohingegen Boags Theorie auf verschwindend geringe Pulsdauern beschränkt ist.

Im Allgemeinen ergab das numerische Berechnungsverfahren Ergebnisse in guter Übereinstimmung mit den experimentellen Beobachtungen für die sehr verschiedenartigen Füllungen von Luft, Stickstoff und Flüssigkeiten. Auch die geometrisch komplexere Kompaktkammer konnte prinzipiell damit beschrieben werden, wobei sich jedoch für die untersuchte PinPoint-Kammer einige Diskrepanzen zu den experimentellen Beobachtungen ergaben.

Eine vielversprechende Weiterentwicklung der Berechnung wäre die verbesserte Beschreibung der Sammelspannungsabhängigkeit der Volumenrekombination. In ihrer derzeitigen Form erfordert die Berechnung eine Charakterisierung jeder Kammer und Spannung, was durch eine Weiterentwicklung der Berechnung möglicherweise eliminiert werden könnte. Nichtsdestotrotz stellt die entwickelte numerische Berechnung eine deutliche Verbesserung gegenüber Boag's Theorie durch die korrekte Beschreibung der Pulsdosis- und Pulsdauerabhängigkeit der Volumenrekombination in stark gepulsten Felder dar, was prinzipiell eine absolute Dosimetrie dieser Felder ermöglichen sollte.

Bibliography

Almond PR, Biggs PJ, Coursey BM, Hanson WF, Huq MS, Nath R, and Rogers DWO. 1999. AAPM's TG-51 Protocol for Clinical Reference Dosimetry of High-Energy Photon and Electron Beams. Med Phys 26:1847–1870. DOI: `10.1118/1.598691`.

Andreo P, Burns DT, Hohlfeld K, Huq MS, Kanai T, Laitano F, Smyth V, and Vynicker S. 2000. Absorbed Dose Determination in External Beam Radiotherapy: An International Code of Practice for Dosimetry Based on Standards of Absorbed Dose to Water. Technical Reports Series of the IAEA. Technical Reports Series 398.

Ankerhold U, Hupe O, and Ambrosi P. 2009. Deficiencies of Active Electronic Radiation Protection Dosemeters in Pulsed Fields. Radiat Prot Dosimetry 135:149–153. DOI: `10.1093/rpd/ncp099`.

Automation und Messtechnik GmbH. 2011. Technical data sheet - scintillator probe 6150AD-b (/H,/E). [Visited on 10/12/2017] URL: `http://www.automess.de/6150AD-b_E.htm`.

Baumann M, Krause M, Overgaard J, Debus J, Bentzen SM, Daartz J, Richter C, Zips D, and Bortfeld T. 2016. Radiation Oncology in the Era of Precision Medicine. Nat Rev Cancer 16:234–249. DOI: `10.1038/nrc.2016.18`.

Berthold Technologies GmbH & Co. KG. 2007. Data Sheet Dose Rate Probe LB 1236-H10. [Visited on 04/19/2017] URL: `https://www.berthold.com/en/rp/lb-123-d-h10-dose-rate-monitor`.

Biagi SF. 1999. Monte Carlo Simulation of Electron Drift and Diffusion in Counting Gases under the Influence of Electric and Magnetic Fields. Nucl Instr Meth Phys Res 421 (1–2):234–240. DOI: `10.1016/S0168-9002(98)01233-9`.

Boag JW. 1950. Ionization Measurements at Very High Intensities - Part I. Br J Radiol 23:601–611. DOI: `10.1259/0007-1285-23-274-601`.

Boag JW. 1987. Ionization Chambers. In: Kase KR, Bjärngard BE, and Attix FH, (eds). The Dosimetry of Ionizing Radiation. Vol. 2. Academic Press Inc, Orlando, pp. 169–245.

Boag JW, Hochhäuser E, and Balk OA. 1996. The Effect of Free-Electron Collection on the Recombination Correction to Ionization Measurements of Pulsed Radiation. Phys Med Biol 41:885–897. DOI: `10.1088/0031-9155/41/5/005`.

Boissonnat G. 2015. Chambres d'ionisation En Protonthérapie et Hadronthérapie. Normandy Université, Caen, Dissertation.

Cella L, Liuzzi R, and Salvatore M. 2010. The Italian Affair: The Employment of Parallel-Plate Ionization Chambers for Dose Measurements in High Dose-per-Pulse IORT Electron Beams. Medical Physics 37:2918–2924. DOI: `10.1118/1.3432601`.

Clairand I, Struelens L, Bordy JM, Daures J, Debroas J, Denozières M, Donadille L, Gouriou J, Itié C, Vaz P, and d'Errico F. 2008. Intercomparison of Active Personal Dosemeters in Interventional Radiology. Radiat Prot Dosimetry 129 (1-3):340–345. DOI: `10.1093/rpd/ncn083`.

CNMC, CNMC Company Inc. 2017. Model PPC05 - Plane-Parallel Ionization Chamber. [Visited on 08/20/2017] URL: `http://www.teambest.com/CNMC_docs/radPhysics/parallel/CNMC_PPC05.pdf`.

Courant R, Friedrichs K, and Lewy H. 1928. Über die partiellen Differenzengleichungen der mathematischen Physik. Math Ann 100:32–74. DOI: `10.1007/BF01448839`.

Davies DK and Chantry PJ. 1985. Air Chemistry Measurements 2. Air Force Weapons Laboratory, Kirtland Air Foirce Base, NM, USA. [Visited on 10/05/2017] URL: `http://www.dtic.mil/cgi-bin/GetTRDoc?Location=U2&doc=GetTRDoc.pdf&AD=ADA156041`.

DIN, Deutsches Institut für Normung e.V. 1985. DIN 6814-3:12-1985. Begriffe in der radiologischen Technik - Teil 3: Dosisgrößen und Dosiseinheiten.

DIN, Deutsches Institut für Normung e.V. 2008. DIN 6800-2:03-2008. Dosismessverfahren nach der Sondenmethode für Photonen- und Elektronenstrahlung - Teil 2: Dosimetrie hochenergetischer Photonen- und Elektronenstrahlung mit Ionisationskammern.

DIN, Deutsches Institut für Normung e.V. 2013. DIN IEC/TS 62743:05-2013. Strahlenschutz Messgeräte: Zählende Elektronische Dosimeter für Gepulste Felder ionisierender Strahlung.

Dierckx P. 1995. Curve and Surface Fitting with Splines. Clarendon Press, Oxford.

Dye JL. 2003. Electrons as Anions. Science 301:607–608. DOI: `10.1126/science.1088103`.

Ebert HG, Booz J, and Koepp R. 1964. Rekombination von Ionen in Luft und Sauerstoff. Z Physik 181:187–195. DOI: `10.1007/BF01380506`.

Einstein A. 1905. Über die von der molekularkinetischen Theorie der Wärme geforderte Bewegung von in ruhenden Flüssigkeiten suspendierten Teilchen. Ann Phys 322:549–560. DOI: `10.1002/andp.19053220806`.

Favaudon V, Caplier L, Monceau V, Pouzoulet F, Sayarath M, Fouillade C, Poupon MF, Brito I, Hupé P, Bourhis J, Hall J, Fontaine JJ, and Vozenin MC. 2014. Ultrahigh Dose-Rate FLASH Irradiation Increases the Differential Response between Normal and Tumor Tissue in Mice. Sci Transl Med 6:245ra93. DOI: `10.1126/scitranslmed.3008973`.

Gerbi BJ, Antolak JA, Deibel FC, Followill DS, Herman MG, Higgins PD, Huq MS, Mihailidis DN, Yorke ED, Hogstrom KR, and Khan FM. 2009. Recommendations for Clinical Electron Beam Dosimetry: Supplement to the Recommendations of Task Group 25. Med Phys 36:3239–3279. DOI: `10.1118/1.3125820`.

Ghorbanpour Besheli M, Simiantonakis I, Zink K, and Budach W. 2016. Determination of the Ion Recombination Correction Factor for Intraoperative Electron Beams. Z Med Phys 26:35–44. DOI: `10.1016/j.zemedi.2015.06.011`.

Gotz M. 2017. numerical-ks-calculator. DOI: `10.5281/zenodo.597850`.

Gotz M, Karsch L, and Pawelke J. 2015. Ortsdosimetrie in Gepulsten Strahlungsfeldern. Schriftenreihe 5/2015. Landesamt für Umwelt, Landwirtschaft und Geologie, Dresden.

Grau C, Defourny N, Malicki J, Dunscombe P, Borras JM, Coffey M, Slotman B, Bogusz M, Gasparotto C, and Lievens Y. 2014. Radiotherapy Equipment and Departments in the European Countries: Final Results from the ESTRO-HERO Survey. Radiotherapy and Oncology 112:155–164. DOI: `10.1016/j.radonc.2014.08.029`.

Gray LH. 1936. An Ionization Method for the Absolute Measurement of γ-Ray Energy. Proceedings of the Royal Society of London A: Mathematical, Physical and Engineering Sciences 156:578–596. DOI: `10.1098/rspa.1936.0169`.

Gutsev GL, Rozyczko PB, and Bartlett RJ. 1999. Does N2- Exist? A Coupled-Cluster Study. The Journal of Chemical Physics 110:5137–5139. DOI: `10.1063/1.478408`.

Hashimoto K, Ohya K, and Yamane Y. 1996. Dead-Time Measurement for Radiation Counters by Variance-to-Mean Method. Journal of Nuclear Science and Technology 33:863–868. DOI: `10.1080/18811248.1996.9732021`.

Hochhäuser E. 1993. Lebensdauer und Driftgeschwindigkeit freier Elektronen in Ionisationskammern. Justus-Liebig-Universität, Gießen, Dissertation.

Hochhäuser E, Balk OA, Schneider H, and Arnold W. 1994. Determination of Electron Swarm Parameters from the Radiation Pulse Response of an Ionization Chamber. J Phys D: Appl Phys 27:2312–2319. DOI: `10.1088/0022-3727/27/11/011`.

Holthusen H. 1936. Erfahrungen über die Verträglichkeitsgrenze für Röntgenstrahlen und deren Nutzanwendung zur Verhütung von Schäden. Strahlentherapie 57:254–269.

Hundsdorfer W and Verwer J. 2003. Numerical Solution of Time-Dependent Advection-Diffusion-Reaction Equations. Springer Series in Computational Mathematics 33. Springer, Berlin. DOI: `10.1007/978-3-662-09017-6_1`.

IAEA. 2007. Intercomparison of Personal Dose Equivalent Measurements by Active Personal Dosimeters. Final Report of a joint IAEA-EURADOS Project. IAEA-TECDOC-1564. International Atomic Energy Agency, Vienna.

IBA. 2014. IBA Recieves FDA Approval of Its New Compact Gantry Clearing the Way for ProteusONE. [Visited on 04/12/2017] URL: `https://iba-worldwide.com/content/iba-receives-fda-approval-its-new-compact-gantry-clearing-way-proteusone`.

ICRP. 2007. The 2007 Recommendations of the International Commission on Radiological Protection. ICRP Publication 103. Ann ICRP 37 (2-4):1–332. DOI: `10.1016/j.icrp.2007.10.003`.

ICRU, International Commission on Radiation Units and Measurements. 1982. ICRU Report No. 34, The Dosimetry of Pulsed Radiation.

ICRU, International Commission on Radiation Units and Measurements. 1985. ICRU Report No. 39, Determination of Dose Equivalents Resulting from External Radiation Sources.

ICRU, International Commission on Radiation Units and Measurements. 2011. ICRU Report No. 85, Fundamental Quantities and Units for Ionizing Radiation.

ISO, International Organization for Standardization. 2015. ISO/TS 18090-1:08-2015. Radiological protection - Characteristics of reference pulsed radiation - Part 1: Photon radiation.

Jaffé G. 1913. Zur Theorie der Ionisation in Kolonnen. Ann Phys 347:303–344. DOI: `10.1002/andp.19133471205`.

Johansson B and Wickman G. 1997. General Collection Efficiency for Liquid Isooctane and Tetramethylsilane Used as Sensitive Media in a Parallel-Plate Ionization Chamber. Phys Med Biol 42:133–145. DOI: `10.1088/0031-9155/42/1/009`.

JCGM, Joint Committee for Guides in Metrology. 2008. Evaluation of Measurement Data — Guide to the Expression of Uncertainty in Measurement. [Visited on 09/06/2017] URL: `www.bipm.org/utils/common/documents/jcgm/JCGM_100_2008_E.pdf`.

Karsch L, Beyreuther E, Burris-Mog T, Kraft S, Richter C, Zeil K, and Pawelke J. 2012. Dose Rate Dependence for Different Dosimeters and Detectors: TLD, OSL, EBT Films, and Diamond Detectors. Medical Physics 39:2447–2455. DOI: `10.1118/1.3700400`.

Karsch L and Pawelke J. 2014. Theoretische Untersuchung der Sättigungskorrektion von Ionisationskammern in gepulsten Strahlungsfeldern bei beliebiger Pulsdauer. Z Med Phys 24:201–210. DOI: `10.1016/j.zemedi.2013.10.007`.

Knoll GF. 2000. Radiation Detection and Measurement. 3rd ed. John Wiley & Sons, Hoboken.

Kossyi IA, Kostinsky AY, Matveyev AA, and Silakov VP. 1992. Kinetic Scheme of the Non-Equilibrium Discharge in Nitrogen-Oxygen Mixtures. Plasma Sources Sci T 1:207–220. DOI: `10.1088/0963-0252/1/3/011`.

Krieger H. 1998. Strahlenphysik, Dosimetrie und Strahlenschutz. 4th ed. Vol. 1. B. G. Teubner, Stuttgart.

Krieger H. 2001. Strahlenphysik, Dosimetrie und Strahlenschutz. 3rd ed. Vol. 2. B.G. Teubner, Stuttgart.

Krimmer J, Dauvergne D, Létang JM, and Testa É. 2017. Prompt-Gamma Monitoring in Hadrontherapy: A Review. Nucl Instrum Methods Phys Res A. DOI: `10.1016/j.nima.2017.07.063`.

Laitano RF, Guerra AS, Pimpinella M, Caporali C, and Petrucci A. 2006. Charge Collection Efficiency in Ionization Chambers Exposed to Electron Beams with High Dose per Pulse. Phys Med Biol 51:6419–6436. DOI: `10.1088/0031-9155/51/24/009`.

Langevin MP. 1902. Sur la recombinaison des ions dans les gaz. C R Hebd Seances Acad Sci 134:533–536.

Linz U and Alonso J. 2007. What Will It Take for Laser Driven Proton Accelerators to Be Applied to Tumor Therapy? Phys Rev ST Accel Beams 10:094801. DOI: `10.1103/PhysRevSTAB.10.094801`.

Loo BW, Schuler E, Lartey FM, Rafat M, King GJ, Trovati S, Koong AC, and Maxim PG. 2017. Delivery of Ultra-Rapid Flash Radiation Therapy and Demonstration of Normal Tissue Sparing After Abdominal Irradiation of Mice. Int J Radiat Oncol Biol Phys. Proceedings of the American Radium Society 98 (2, Supplement):E16. DOI: `10.1016/j.ijrobp.2017.02.101`.

Maier A, Westphal S, Geimer T, Maxim PG, King G, Schueler E, Fahrig R, and Loo B. 2017. Fast Pose Verification for High-Speed Radiation Therapy. In: Bildverarbeitung für die Medizin 2017. Informatik aktuell. Springer Vieweg, Berlin, Heidelberg, pp. 104–109. DOI: `10.1007/978-3-662-54345-0_27`.

Marshall LC. 1929. The Recombination of Ions and of Ions and Electrons in Gases. Phys Rev 34:618–634. DOI: `10.1103/PhysRev.34.618`.

di Martino F, Giannelli M, Traino AC, and Lazzeri M. 2005. Ion Recombination Correction for Very High Dose-per-Pulse High-Energy Electron Beams. Med Phys 32:2204–2210. DOI: `10.1118/1.1940167`.

Masood U, Bussmann M, Cowan TE, Enghardt W, Karsch L, Kroll F, Schramm U, and Pawelke J. 2014. A Compact Solution for Ion Beam Therapy with Laser Accelerated Protons. Appl Phys B 117:41–52. DOI: `10.1007/s00340-014-5796-z`.

Maxim PG and Loo BW. 2014. Pluridirectional High-Energy Agile Scanning Electron Radiotherapy (PHASER): Extremely Rapid Treatment for Early Lung Cancer. LELAND STANFORD JUNIOR UNIV CA. [Visited on 02/20/2017] URL: `http://oai.dtic.mil/oai/oai?verb=getRecord&metadataPrefix=html&identifier=ADA607938`.

McGowan S. 1965. Ion-Ion Recombination in Laboratory Air. Phys Med Biol 10:25–40. DOI: `10.1088/0031-9155/10/1/303`.

Mevion, Mevion Medical Systems. 2012. Mevion Medical Systems Announces FDA 510(k) Clearance for the MEVION S250 Proton Therapy System. [Visited on 04/12/2017] URL: `http://www.prnewswire.com/news-releases/mevion-medical-systems-announces-fda-510k-clearance-for-the-mevion-s250-proton-therapy-system-158424625.html`.

Mie G. 1904. Der elektrische Strom in ionisierter Luft in einem ebenen Kondensator. Ann Phys 318:857–889. DOI: `10.1002/andp.18943180502`.

Onsager L. 1938. Initial Recombination of Ions. Phys Rev 54:554–557. DOI: `10.1103/PhysRev.54.554`.

Pardo-Montero J, Tegami S, Gago-Arias A, González-Castaño DM, Holzscheiter MH, and Gómez F. 2012. Analysis of Ionic Mobilities in Liquid Isooctane with Low Dose Radiotherapy Pulsed Photon Beams. J Inst 7 (09):P09008. DOI: `10.1088/1748-0221/7/09/P09008`.

Podgorsak EB (ed). 2005. Radiation Oncology Physics: A Handbook for Teachers and Students. International Atomic Energy Agency, Vienna. [Visited on 09/29/2016] URL: `http://www-pub.iaea.org/books/IAEABooks/7086/Radiation-Oncology-Physics`.

PTB, Physikalisch-Technische Bundesanstalt. 2009. Problematik bei Messungen in gepulsten Photonen-Strahlungsfeldern. [Visited on 04/14/2017] URL: `https://www.ptb.de/cms/fileadmin/internet/fachabteilungen/abteilung_6/6.3/bap/gepstrl.pdf`.

PTB, Physikalisch-Technische Bundesanstalt. 2013. Strahlenschutzmessgeräte - Ortsdosimeter zur Messung der Umgebungs- und Richtungs-Äquivalentdosis und der Umgebungs- und Richtungs-Äquivalentdosisleistung. A 23.3. [Visited on 02/08/2017] URL: `http://www.ptb.de/cms/fileadmin/internet/fachabteilungen/abteilung_6/6.3/bap/ptb23_3.pdf`.

PTCOG, Particle Therapy Co-Operative Group. 2016. Particle therapy facilities in operation. [Visited on 08/23/2016] URL: `http://www.ptcog.ch/index.php/facilities-in-operation`.

PTW, Physikalisch-Technische Werkstätten Dr. Pychlau GmbH. 2016. Radiation Medicine QA Solutions. [Visited on 04/24/2017] URL: `http://www.ptw.de/fileadmin/data/download/catalogviewer/DETECTORS_Cat_en_16522900_10/blaetterkatalog/index.html`.

Ramo S. 1939. Currents Induced by Electron Motion. Proc IRE 27:584–585. DOI: `10.1109/JRPROC.1939.228757`.

RKI, Robert Koch-Institut and Gesellschaft der epidemiologischen Krebsregister in Deutschland e.V. (eds). 2015. Krebs in Deutschland 2011/2012. 10th ed. Berlin. DOI: `10.17886/rkipubl-2015-004`.

Rohling H. 2015. private communication.

Rotem Industries LTD. 2014. Technical data sheet - the RAM ION Monitor. [Visited on 10/13/2017] URL: `http://www.rotem-radiation.co.il/product/ram-ion-meter/`.

Sayers J. 1938. Ionic Recombination in Air. Proc R Soc Lond A Math Phys Sci 169:83–101. DOI: `10.1098/rspa.1938.0196`.

Schindewolf U. 1968. Bildungsreaktionen und Eigenschaften solvatisierter Elektronen. Angew Chem 80:165–179. DOI: `10.1002/ange.19680800502`.

Shockley W. 1938. Currents to Conductors Induced by a Moving Point Charge. J Appl Phys 9:635–636. DOI: `10.1063/1.1710367`.

von Smoluchowski M. 1906. Zur kinetischen Theorie der Brownschen Molekularbewegung und der Suspensionen. Ann Phys 326:756–780. DOI: `10.1002/andp.19063261405`.

Viehland LA and Mason EA. 1995. Transport Properties of Gaseous Ions over a Wide Energy Range, IV. At Data Nucl Data Tables 60:37–95. DOI: `10.1006/adnd.1995.1004`.

Zeil K, Kraft SD, Bock S, Bussmann M, Cowan TE, Kluge T, Metzkes J, Richter T, Sauerbrey R, and Schramm U. 2010. The Scaling of Proton Energies in Ultrashort Pulse Laser Plasma Acceleration. New J Phys 12:045015. DOI: `10.1088/1367-2630/12/4/045015`.

Appendix

A Evaluation of the Faraday Cup Data

The charge sensitive amplifier, connected to the Faraday cup, provided a time dependent voltage signal which was recorded with a digital oscilloscope. From this time dependent signal a single value had to be extracted, in order to associate each radiation pulse with a specific voltage signal from the charge sensitive amplifier. In the simplest case (for very short radiation pulses) this voltage step, induced by the radiation pulse, could be obtained from taking the difference of the average of the signal before and after the pulse. An example of this is shown in Fig. A.1.

For longer pulse durations (an example is shown in Fig. A.2), in addition to the noise and oscillations, the signal is affected by a decay due to a discharge of the measured charge. In order to correct for this discharge the signal after the pulse was not simply averaged, but rather fitted linearly. This linear fit was used to extrapolate to a hypothetical signal at the start of the pulse in order to correct for signal loss during the pulse. A difference was then taken between the signal before the pulse and this extrapolated signal to obtain a value for the Faraday cup measurement.

For very long pulse durations (more than 4000 bunches, i.e, $t_{\mathrm{pulse}} \gtrsim 400\,\mu\mathrm{s}$) this linear extrapolation seemed inappropriate as well, since non linear components of the decay begin to show increasingly (see Fig. A.3). Here the signal during the pulse was fitted with a model function instead. The assumptions of this model are that a continuous current (I_{irr}, the radiation pulse) charges a capacitance C_{FC}. At the same time this capacitance is discharged across a resistance R_{loss}. This leads to the differential equation for the charge on the capacitance Q:

$$\frac{\mathrm{d}Q}{\mathrm{d}t} = I_{\mathrm{irr}} - \frac{Q}{C_{\mathrm{FC}} \cdot R_{\mathrm{loss}}}.$$

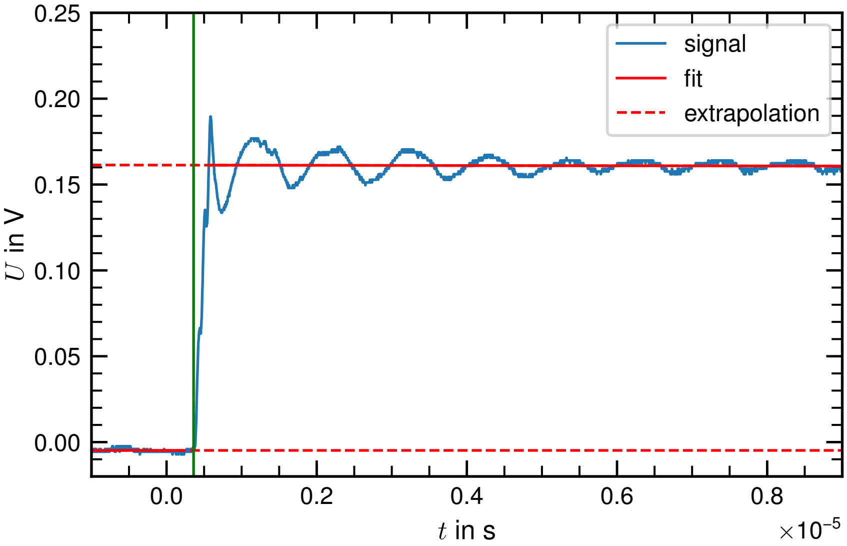

Figure A.1: Time dependent voltage signal (blue line) recorded with the oscilloscope from the charge sensitive amplifier connected to the Faraday cup for a very short radiation pulse ($t_{\mathrm{pulse}} =$ 154 ns. The green vertical line marks the beginning of the radiation pulse, where the extrapolations (red dashed lines) of the two fits (red solid lines) are evaluated.

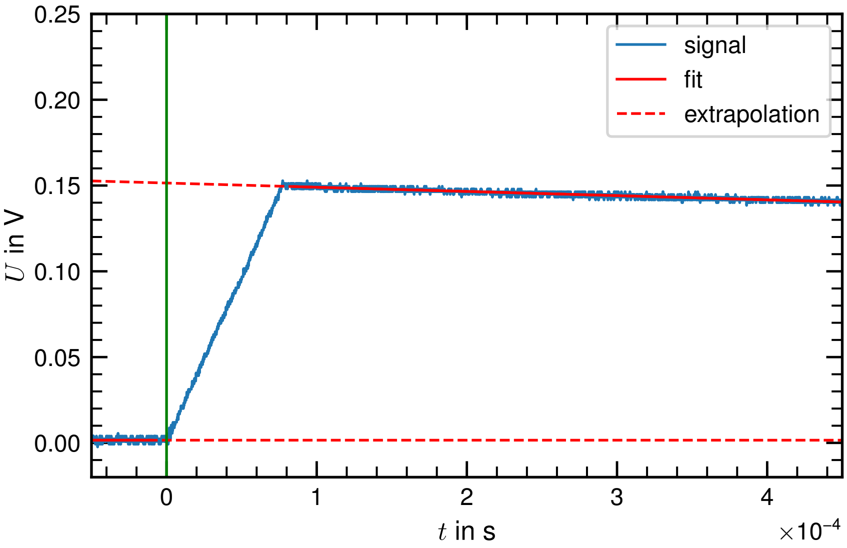

Figure A.2: Time dependent voltage signal (blue line) recorded with the oscilloscope from the charge sensitive amplifier connected to the Faraday cup for a long radiation pulse ($t_{\mathrm{pulse}} = 76.92$ µs. The green vertical line marks the beginning of the radiation pulse, where the extrapolations (red dashed lines) of the two fits (red solid lines) are evaluated.

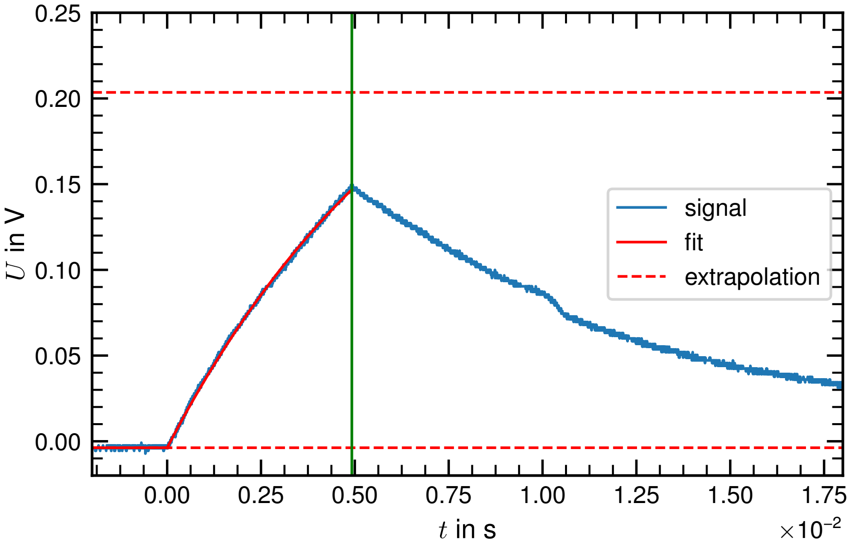

Figure A.3: Time dependent voltage signal (blue line) recorded with the oscilloscope from the charge sensitive amplifier connected to the Faraday cup for a very long radiation pulse ($t_{\text{pulse}} =$ 2.464 ms. The green vertical line marks the beginning of the radiation pulse, where the extrapolations (red dashed lines) of the two fits (red solid lines) are evaluated.

The solution for $Q(0) = 0$ is:

$$Q(t) = I_{\text{irr}} \cdot C_{\text{FC}} \cdot R_{\text{loss}} \left(1 - e^{-\frac{t}{C_{\text{FC}} \cdot R_{\text{loss}}}}\right) .$$

Using this model one can fit a function $y(t) = a \cdot \left(1 - e^{-\frac{t}{b}}\right)$ to the measured signal and derive the total charge without loss from $Q = \frac{a}{b} \cdot t_{\text{pulse}}$, which is the fit shown in Fig. A.3. While it should be in principle suitable for any pulse duration, this approach was only applied to very long pulses ($t_{\text{pulse}} >$ 400 µs) because the fit resulted in large uncertainties for shorter pulse durations. These large uncertainties are due to the almost linear curves for shorter pulses, which make the observation and estimation of the asymptotic term $e^{-\frac{t}{b}}$ difficult. Therefore, this last approach was only used for the very long pulse durations employed in the measurements of the isooctane LIC.

In order to provide a good consistency of the evaluation, the method of linear extrapolation was used for all pulse durations $t_{\text{pulse}} \leq$ 400 µs. At very short pulse durations a simple average would have sufficed, but defining a clear criterion for the transition is difficult and the linear extrapolation gave the same results as the averaging in those cases. Therefore, using a single method was chosen as the preferable approach.

A measurement of the dose dependence of k_s for one chamber at one voltage entailed around 300 individual measurements, meaning 300 data sets of time dependent voltages, which had to be evaluated to obtain single voltage values for the Faraday cup. To handle this amount of data a semi-automatic python script was employed, which on request loaded the next data set in a folder and performed the fitting and difference calculation using the settings of the previous data set. Typically, this reduced the evaluation effort to clicking through a couple hundred datasets, only requiring adjustment of the ranges on which the averaging and fits were performed, when the pulse duration changed.

B Description of the Implemented Numerical Solver

The full source code of the implementation of the numerical algorithm outlined in section 3.4 is archived in Gotz (2017). Here a supplemental description of the implementation is given to ease the understanding of this source code. The implementation is written in C++03 using program-options and property-tree from the boost libraries (version 1.55.0) and cmake (version 3.0.2) as a build system.

At the core of the solver are sets of nested loops. The outer loop steps forward through time, while several inner loops iterate over the spatial bins. This core time loop is shown as a block diagram in Fig. B.1, with each process operating on all the spatial bins.

In one time step new charge concentrations are calculated from the old ones by successively considering the liberation of new charges through radiation, the advection and recombination of ions and the advection and recombination of electrons. From this new charge concentration the charges outside the sensitive volume are “collected” by zeroing those bins and adding their values to the collected charge. The electric field for the next time step is calculated using those newly determined concentrations. Finally the size of the next time step is calculated using this electric field and the resulting maximum velocity.

Most of the details of the implementation are concerned with allowing a variety of choices about the specific calculation at runtime, such as chamber type, properties of the active medium or the beam, while maintaining speedy performance.

Allowing both continuous and micro-pulsed beams and chambers of different geometry is realized through two abstract base classes (beam_model and chamber) with specific child classes, e.g. cylinder and plane-parallel. The abstract base class essentially defines

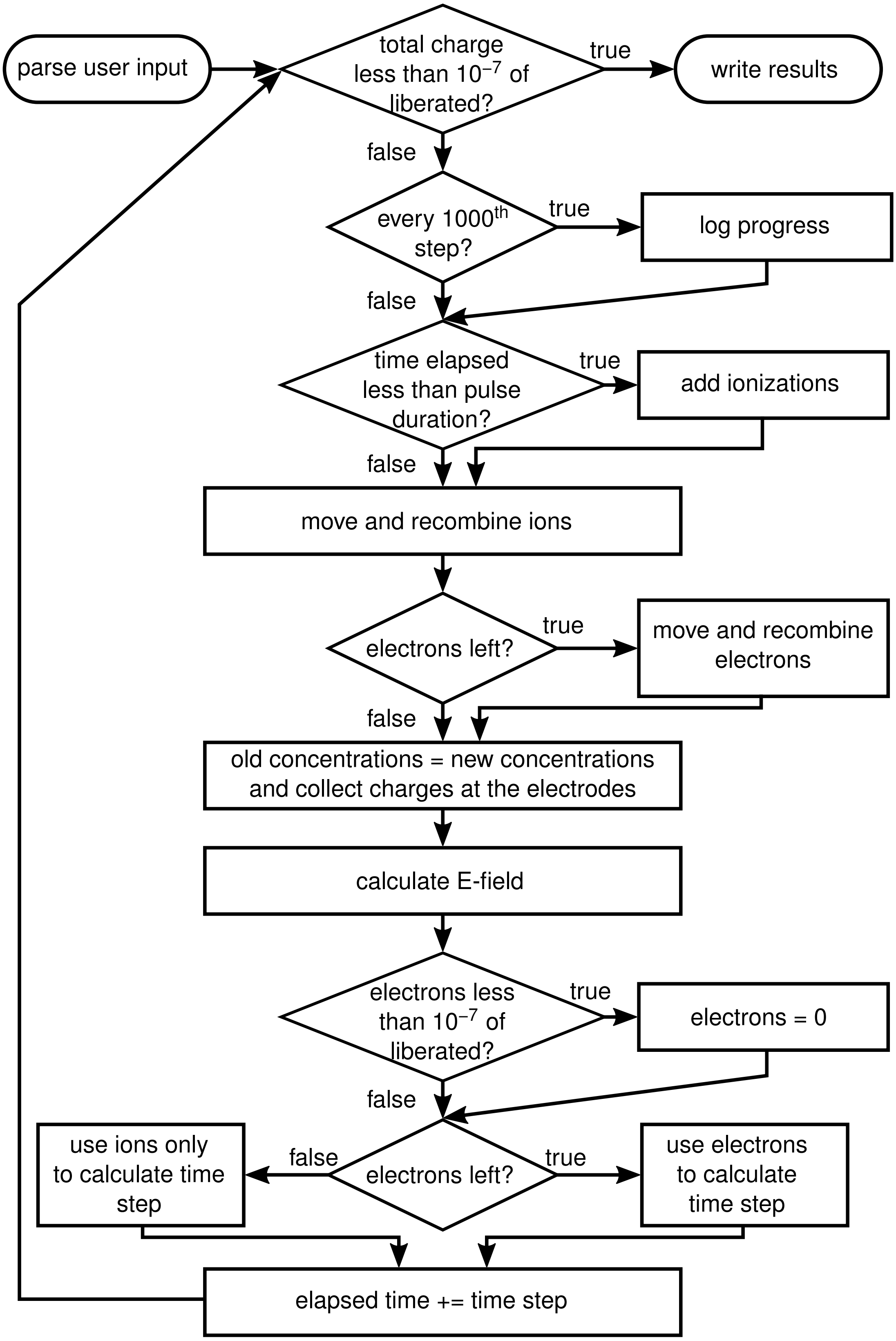

Figure B.1: Flow-chart illustrating the steps of the loop at the core of the numerical solver implemented in Gotz (2017) an interface with certain common methods, such as calculating the liberated charge in the chamber. The child classes then provide concrete implementations to, for example, calculate the liberated charge for a cylindrical or plane-parallel chamber. Therefore, the concrete type of chamber or beam maybe chosen at runtime.

In a similar manner different functions to describe the electric field strength dependence of the parameters describing the active medium, such as ion mobility or attachment rate, are realized. A base class (evaluation_functiod) exposing a single method (evaluate) is given for each property. At runtime a specific child object, such as a linear function, is instantiated containing the parameters defining the function (i.e., slope and intercept for a linear function) and implementing an appropriate evaluate function.

Unfortunately, the choice between cylindrical and plane-parallel chamber does not only impact calculation of isolated parameters, such as the liberated charge, but also requires a different treatment of the advection step. The same is true for the polarity of the collection voltage in the cylindrical chamber due to the upwind nature of the discretization, while polarity has no effect in the plane-parallel chamber because of the reflection symmetry of its 1-D representation. This difference in the advection step could be realized with a simple if-branching at each step of the inner spatial loops. However, this may incur repetitive branch misses inside these inner loops, causing significant computational overhead.

In order to avoid such branch misses, the core time loop is implemented as a template taking the chamber geometry and polarity as its instantiation parameters. Thus, the runtime parameters polarity and chamber geometry become compilation time constants and the branches in the inner loops are optimized by the compiler. This template is instantiated once for the plane-parallel geometry and twice for the cylindrical geometry (once for both polarities). Therefore, all the choices are still available at runtime. The template approach causes the generation of duplicate execution code, increasing the size of the program, but avoids duplicate source code and expensive branch misses.

Additional optimizations are enabled through cmake options that control the conditional compilation of parts of the source code. Those allow to specify that the recombination rates and ion mobilities are constant, avoiding superfluous function calls, set the logging level to control the information output and disable the electron-ion recombination, reducing computation time compared to simply setting the rate to zero. Furthermore, it is possible to generate an output of all the charge concentrations at fixed intervals and perform the calculation with a fixed electric field using those switches.

Danksagung

Diese Arbeit wäre ohne die vielfältige Unterstützung verschiedenster Menschen nicht möglich gewesen und ich möchte hier meinen herzlichen Dank für diese Unterstützung ausdrücken.

Insbesondere möchte ich meinen Betreuern Dr. Leonhard Karsch und Dr. Jörg Pawelke sowie Prof. Dr. Wolfgang Enghardt danken, die mir die Möglichkeit eröffnet haben am OncoRay zu promovieren. So erlangte ich Einblicke in die faszinierende Welt der Strahlentherapie, Laser-Teilchenbeschleunigung und letztendlich der Dosimetrie gepulster Strahlung. Meine Betreuer gaben mir alle erdenklichen Freiräume und befähigten mich so zu einer wirklich eigenverantwortlichen Arbeitsweise, standen mir bei Bedarf aber auch immer mit Rat und Tat zur Seite. Die Zeit am OncoRay war dadurch geprägt durch eine enorme persönliche wie auch fachliche Weiterentwicklung für mich.

Mein Dank gilt außerdem Michael Schürer, für viele hilfreiche Konstruktionen und seine stets fröhliche Art, und Andreas Schuhmann für all die Python-Teilstücke, die mir immer wieder als Sprungbrett dienten.

Eine Aufzählung all der Kollegen und Freunde, die im Doktorandenraum, beim Mittag- und Kuchenessen, beim Bouldern und Rudern die Moral hoch hielten und im Großen und Kleinen aushalfen, wäre immer unvollständig und soll daher gar nicht versucht werden.

Erwähnt werden soll aber noch Guillaume Boissonnat, der extrem bereitwillig seine Daten zur Beweglichkeit und Anlagerung in Luft teilte, die eine ungemeine Bereicherung für meine Arbeit waren. Dafür möchte ich mich genauso herzlich bedanken wie für Heikki Töllis Bereitschaft, seine Flüssigionisationskammern zur Verfügung zu stellen.

All diese Unterstützung wäre allerdings wahrscheinlich vergebens ohne die unnachgiebige Bestärkung meiner Familie. In Liebe und Dankbarkeit verbunden bleibe ich dafür Rebecca und Kathleen, die trotz manch schlafloser Nacht immer ein Lichtblick waren.

Erklärungen zur Eröffnung des Promotionsverfahrens

1. Hiermit versichere ich, dass ich die vorliegende Arbeit ohne unzulässige Hilfe Dritter und ohne Benutzung anderer als der angegebenen Hilfsmittel angefertigt habe; die aus fremden Quellen direkt oder indirekt übernommenen Gedanken sind als solche kenntlich gemacht.

2. Bei der Auswahl und Auswertung des Materials sowie bei der Herstellung des Manuskripts habe ich Unterstützungsleistungen von folgenden Personen erhalten:
   Dr. Leonhard Karsch, Dr Jörg Pawelke

3. Weitere Personen waren an der geistigen Herstellung der vorliegenden Arbeit nicht beteiligt. Insbesondere habe ich nicht die Hilfe eines kommerziellen Promotionsberaters in Anspruch genommen. Dritte haben von mir weder unmittelbar noch mittelbar geldwerte Leistungen für Arbeiten erhalten, die im Zusammenhang mit dem Inhalt der vorgelegten Dissertation stehen.

4. Die Arbeit wurde bisher weder im Inland noch im Ausland in gleicher oder ähnlicher Form einer anderen Prüfungsbehörde vorgelegt.

5. Die Inhalte dieser Dissertation wurden in folgender Form veröffentlicht:

   - Gotz M, Karsch L und Pawelke J. 2015. Ortsdosimetrie in Gepulsten Strahlungsfeldern. Schriftenreihe 5/2015. Landesamt für Umwelt, Landwirtschaft und Geologie, Dresden
   - Gotz M, Karsch L und Pawelke J. 2015. Comparative Investigation of Three Dose Rate Meters for Their Viability in Pulsed Radiation Fields. J Radiol Prot 35:415. DOI: `10.1088/0952-4746/35/2/415`
   - Gotz M, Karsch L und Pawelke J. 2017. A New Model for Volume Recombination in Plane-Parallel Chambers in Pulsed Fields of High Dose-per-Pulse. Phys Med Biol [Epub ahead of print]. DOI: `10.1088/1361-6560/aa8985`

6. Ich bestätige, dass es keine zurückliegenden erfolglosen Promotionsverfahren gab.

7. Ich bestätige, dass ich die Promotionsordnung der Medizinischen Fakultät Carl Gustav Carus der Technischen Universität Dresden anerkenne.

8. Ich habe die Zitierrichtlinien für Dissertationen an der Medizinischen Fakultät der Technischen Universität Dresden zur Kenntnis genommen und befolgt.

Dresden, 16. Oktober 2017 __________________________________

Erklärung über die Einhaltung der gesetzlichen Bestimmungen

Hiermit bestätige ich die Einhaltung der folgenden aktuellen gesetzlichen Vorgaben im Rahmen meiner Dissertation

- ☐ ~~das zustimmende Votum der Ethikkommission bei Klinischen Studien, epidemiologischen Untersuchungen mit Personenbezug oder Sachverhalten, die das Medizinproduktegesetz betreffen~~
  nicht zutreffend
- ☐ ~~die Einhaltung der Bestimmungen des Tierschutzgesetzes~~
  nicht zutreffend
- ☐ ~~die Einhaltung des Gentechnikgesetzes~~
  nicht zutreffend
- ☐ ~~die Einhaltung von Datenschutzbestimmungen der Medizinischen Fakultät und des Universitätsklinikums Carl Gustav Carus.~~
  nicht zutreffend

Dresden, 16. Oktober 2017 __________________________________

HZDR

HELMHOLTZ
ZENTRUM DRESDEN
ROSSENDORF

Bautzner Landstr. 400
01328 Dresden, Germany
Tel. +49 351 458-7628
Fax +49 351 458-7311
m.gotz@hzdr.de
http://www.hzdr.de